

December 2013

Structure and Function of Proteins Investigated By Crystallographic and Spectroscopic Time- Resolved Methods

Namrta Purwar

University of Wisconsin-Milwaukee

Follow this and additional works at: <https://dc.uwm.edu/etd>

 Part of the [Biophysics Commons](#), and the [Physics Commons](#)

Recommended Citation

Purwar, Namrta, "Structure and Function of Proteins Investigated By Crystallographic and Spectroscopic Time-Resolved Methods" (2013). *Theses and Dissertations*. 372.
<https://dc.uwm.edu/etd/372>

This Dissertation is brought to you for free and open access by UWM Digital Commons. It has been accepted for inclusion in Theses and Dissertations by an authorized administrator of UWM Digital Commons. For more information, please contact open-access@uwm.edu.

**STRUCTURE AND FUNCTION OF PROTEINS
INVESTIGATED BY CRYSTALLOGRAPHIC AND
SPECTROSCOPIC TIME-RESOLVED METHODS**

by

Namrta Purwar

A Dissertation Submitted in

Partial Fulfillment of the

Requirements for the Degree of

Doctor of Philosophy

in Physics

at

The University of Wisconsin-Milwaukee

December 2013

ABSTRACT

STRUCTURE AND FUNCTION OF PROTEINS INVESTIGATED BY CRYSTALLOGRAPHIC AND SPECTROSCOPIC TIME-RESOLVED METHODS

by

Namrta Purwar

The University of Wisconsin-Milwaukee, 2013
Under the Supervision of Dr. Marius Schmidt

Biomolecules play an essential role in performing the necessary functions for life. The goal of this thesis is to contribute to an understanding of how biological systems work on the molecular level. We used two biological systems, beef liver catalase (BLC) and photoactive yellow protein (PYP). BLC is a metalloprotein that protects living cells from the harmful effects of reactive oxygen species by converting H_2O_2 into water and oxygen. By binding nitric oxide (NO) to the catalase, a complex was generated that mimics the Cat- H_2O_2 adduct, a crucial intermediate in the reaction promoted by the catalase. The Cat-NO complex is obtained by using a convenient NO generator (1-(N,N-diethylamino)diazen-1-ium-1,2-diolate). Concentrations up to 100~200 mM are reached by using a specially designed glass cavity. With this glass apparatus and DEANO, sufficient NO occupation is achieved and structure determination of the catalase with NO bound to the heme iron becomes possible. Structural changes upon NO binding are

minute. NO has a slightly bent geometry with respect to the heme normal, which results in a substantial overlap of the NO orbitals with the iron-porphyrin molecular orbitals. From the structure of the iron-NO complex, conclusions on the electronic properties of the heme iron can be drawn that ultimately lead to an insight into the catalytic properties of this enzyme.

Enzyme kinetics is affected by additional parameters such as temperature and pH. Additionally, in crystallography, the absorbed X-ray dose may impair protein function. To address the effect of these parameters, we performed time-resolved crystallographic experiments on a model system, PYP. By collecting multiple time-series on PYP at increasing X-ray dose levels, we determined a kinetic dose limit up to which kinetically meaningful X-ray data sets can be collected. From this, we conclude that comprehensive time-series spanning up to 12 orders of magnitude in time can be collected from a single PYP crystal. Time-resolved X-ray data collected at pH's of 4, 7 and 9 demonstrate that pH alters the kinetics of the PYP photocycle dramatically. At pH 4 the photocycle lasts almost one order of magnitude longer in time compared to pH 7. The final intermediate that accumulates at both pH 7 and pH 4 is absent at pH 9. Results from the dose- and the pH-dependent time-resolved crystallographic experiments show that it is imperative to carefully control the conditions under which time-resolved data are collected. With these considerations we collected a comprehensive time-series from nanoseconds to seconds at 14 different temperature settings from -40 °C to 70 °C. Results from time-resolved crystallography are corroborated by employing time-resolved absorption spectroscopy. For this, absorption spectra on crystals and solution are collected by a fast micro-

spectrophotometer custom-designed in our lab. We identify kinetic phases of the PYP photocycle at all 14 temperature settings. Relaxation times associated with these phases are temperature-dependent and can be fit by the Van't Hoff-Arrhenius equation. Kinetic modeling yields entropy and enthalpy values at the barriers of the activation solely from the time-resolved crystallographic data. With this, we advance crystallography to a new frontier: the determination of free energy surfaces.

Investigating enzymatic reactions can be challenging, because they are non-cyclic. After one turnover product must be washed away and substrate must be reloaded. A promising approach for routine application can be envisioned at the new 4th generation X-ray sources, such as X-ray free electron lasers (XFELs). With our results we set the scene to comprehensively investigate all kinds of enzymatic reactions with these instruments.

TABLE OF CONTENTS

ABSTRACT.....	II
TABLE OF CONTENTS	V
LIST OF FIGURES	IX
LIST OF TABLES	XII
ACKNOWLEDGEMENS	XIII
1 INTRODUCTION.....	1
1.1 Enzymes: structure and function	1
1.2 Short history of crystallography.....	2
1.3 From static structure to function	4
1.4 Catalase.....	5
1.5 PYP	9
1.6 Effect of X-rays doses on PYP	14
1.7 Effect of pH on the PYP	15
1.8 Effect of temperature on PYP.....	16
2 MATERIAL AND METHODS.....	23
2.1 Monochromatic X-ray crystallography	23
2.1.1 Scattering from an atom	23
2.1.2 Scattering from a molecule	23
2.1.3 Scattering from a crystal	24
2.1.4 The lattice factor for a crystal having an infinite number of unit cells	26
2.1.5 Deviation of the lattice factor due to a finite size crystal	26
2.1.6 Scattering vector H	27
2.1.7 The Bragg conditions	28
2.1.8 Physical and experimental resolution limit	29
2.1.9 Structural heterogeneity and dynamic disorder.....	29
2.1.10 The mosaicity	32
2.1.11 Lorentz factor	33
2.1.12 Polarization factor	33
2.1.13 Total integral intensity scattered by a crystal	34

2.1.14 Sample preparation and mounting.....	34
2.1.15 Experimental setup.....	35
2.1.16 Data collection	36
2.1.17 Data analysis and refinement	36
2.1.18 Molecular replacement and crystallographic refinement	39
2.1.19 Water search and addition.....	41
2.1.20 Structure validation	42
2.2 Laue and time-resolved X-ray crystallography	43
2.2.1 Polychromatic X-rays.....	43
2.2.2 Instantaneous recording of integral intensity	44
2.2.3 Spatially overlapping reflections.....	44
2.2.4 λ -curve for wavelength normalization	44
2.2.5 Harmonically overlapping reflections	45
2.2.6 Scattering background.....	46
2.2.7 The mosaicity	47
2.2.8 Time-resolved Laue method.....	48
2.2.9 Sample mounting	49
2.2.10 Experimental setup.....	50
2.2.11 Data collection	51
2.2.12 Data reduction by Precognition.....	52
2.2.13 Scaling by EpiNorm.....	54
2.2.14 From structure factor amplitudes to electron density maps	54
2.2.15 Singular value decomposition of difference electron density map	56
2.2.16 Kinetic analysis of Laue data	58
2.2.17 Posterior analysis	58
2.3 Time-resolved spectroscopy	59
2.3.1 UV-Vis radiation.....	59
2.3.2 Chromophore.....	60
2.3.3 Beer-Lambert law.....	60
2.3.4 Time-resolved spectroscopic investigations.....	61
2.3.5 Sample preparation.....	62
2.3.6 Sample mounting	63
2.3.7 Setup of a self-designed fast micro-spectrophotometer	64
2.3.8 Timing scheme for synchronization.....	67
2.3.9 Display of selected pulses during data collection	69
2.3.10 Description of the Andor Basic data collection software	70
2.3.11 The Matlab data analysis program	73
2.4 Biochemical procedures	75
2.4.1 Beef liver catalase (BLC).....	75
2.4.2 Photoactive yellow protein (PYP).....	76
2.5 Experimental details to investigate interaction of nitric oxide (NO) with catalase.....	78
2.5.1 Monochromatic X-ray crystallographic experiments.....	79
2.5.2 Micro-spectrophotometric experiments (performed at BioCARS)	83

2.6	Experimental details to investigate the kinetic dose limit in PYP	84
2.6.1	Data collection	84
2.6.2	Absorbed dose calculation	85
2.6.3	SVD analysis	88
2.7	Experimental details to investigate the pH dependence of PYP photocycle	89
2.7.1	Data Collection.....	89
2.7.2	Kinetic analysis	90
2.7.3	Extrapolated maps	90
2.8	Experimental details to investigate the temperature dependence of the PYP photocycle	91
2.8.1	Time-resolved crystallography.....	91
2.8.2	Time-resolved spectroscopy.....	93
3	RESULTS	97
3.1	Interaction of Nitric Oxide (NO) with Catalase: X-ray crystallographic analysis.....	97
3.1.1	Crystal structures.....	97
3.1.2	Ammonia-bound Catalase form (Cat-NH ₃).....	99
3.1.3	The five-coordinate Cat-5	100
3.1.4	Cat-NO Structure	101
3.2	Interaction of Nitric Oxide (NO) with Catalase: Micro-spectrophotometric analysis.....	103
3.2.1	Spectral changes for Cat-5, Cat-NH ₃ and Cat-NO	103
3.3	Time-resolved Laue crystallography: Effect of X-ray dose on PYP	105
3.3.1	Data processing	105
3.3.2	Average absorbed dose.....	105
3.3.3	Correction to the absorbed dose (<i>D_{corr}</i>).....	106
3.3.4	Correction for laser damage using the control experiment	107
3.3.5	First Right singular vectors (rSVs) from SVD.....	108
3.3.6	The ratio of the amplitude to the offset	109
3.3.7	Relaxation times.....	110
3.4	Time-resolved Laue crystallography: Effect of pH on PYP	112
3.4.1	Data processing	112
3.4.2	Averaged difference maps and extrapolated electron density maps of intermediates	114
3.4.3	Structural analysis of intermediates at pH 7, pH 4 and pH 9	116
3.4.4	Kinetic Analysis.....	117
3.5	Effect of temperature on PYP photocycle	117
3.5.1	Time-resolved Laue crystallography.....	117

3.5.2	Time-resolved spectroscopy.....	120
4	DISCUSSION	125
4.1	Catalase: structure and function.....	125
4.1.1	Significance for other heme proteins involved in electron transfer	129
4.1.2	Summary	129
4.2	Time-resolved study on PYP.....	130
4.2.1	Effect of radiation dose	130
4.2.2	Effect of pH.....	134
4.2.3	Effect of temperature.....	138
4.3	Future applications.....	141
5	APPENDICES	149
5.1	Appendix A: Program 1 for time-resolved spectroscopic data collection	150
5.2	Appendix B: Graphical user interface for the timing synchronization	153
5.3	Appendix C: Program 2 for time-resolved spectroscopic data analysis...	154
5.4	Appendix D: Program 3 for the fitting of right singular vectors using a sum of exponentials.....	157
5.5	Appendix E: A figure showing the relaxation times obtained from time-resolved crystallography	159

LIST OF FIGURES

Figure 1.1 Chemical structure of the prosthetic group heme type 'B'	6
Figure 1.2 Quaternary structure of bovine liver catalase (BLC).....	7
Figure 1.3 A. Cartoon representation of the photoactive yellow protein	10
Figure 1.4 A. Photoactive yellow protein (PYP) photocycle	12
Figure 2.1 A. Atomic form factors of oxygen, carbon and hydrogen atoms plotted as a function of $\sin\theta/\lambda$. ..	24
Figure 2.2 A. An example of four unit cells with the translational vectors a , b , and c (not shown, lies parallel to a \times b) in real space.....	25
Figure 2.3 Representation of the diffraction geometry in reciprocal space for the conventional rotation method.....	28
Figure 2.4 A. Several factors contribute to the static disorder and one of them is demonstrated	30
Figure 2.5 A. The atomic form factor of a carbon atom, normalized to its atomic number plotted against $\sin \theta/\lambda$ and resolution d	31
Figure 2.6 Effect of the mosaicity χ on the reciprocal lattice points	32
Figure 2.7 Schemes for different methods to crystallize proteins	35
Figure 2.8 A. A typical diffraction pattern obtained for catalase using monochromatic x-ray crystallography.....	36
Figure 2.9 Scheme for monochromatic X-ray data collection	37
Figure 2.10 Scheme for monochromatic X-ray data analysis.....	38
Figure 2.11 A reciprocal space representation of Laue diffraction by a stationary crystal	43
Figure 2.12 A typical λ -curve determined from an experimental data set collected at beamline BioCARS 14-ID-B at Advanced Photon Source (APS).....	45
Figure 2.13 A scheme of time-resolved Laue crystallography.....	47
Figure 2.14 A. A pencil-shaped long PYP crystal mounted in a glass capillary for the time-resolved experiments	49
Figure 2.15 A. The main steps associated with time-resolved Laue data processing.....	53
Figure 2.16 Difference maps near the p-cinnamic acid (pCA) chromophore in PYP	56
Figure 2.17 A scheme of Singular value decomposition (SVD).....	57
Figure 2.18 Two examples of kinetic mechanisms used for slower part of the PYP photocycle.....	59
Figure 2.19 Chromophore of photoactive yellow protein (PYP)	60
Figure 2.20 Two types of samples used for the time-resolved spectroscopic experiments	61

Figure 2.21 A. Image of the sample environment of our micro-spectrophotometer setup.....	64
Figure 2.22 A. A scheme of the in-house microspectrophotometer designed in our lab	65
Figure 2.24 Electronic pulses monitored with the oscilloscope during time-resolved spectroscopic experiments.....	69
Figure 2.25 Reasons for the CCD dark current and their effects on the absorption spectra at different time delays.....	71
Figure 2.26 A. A charge couple device (CCD) of the Andor iStar with full vertical binning (FVB) as a read out mode.....	72
Figure 2.27 Typical examples of time-resolved absorption spectra collected on PYP solution at ambient temperature	74
Figure 2.28 Scheme to prepare all three crystal forms of catalase	79
Figure 2.29 A. Molecular structure of DEANO. DEANO decomposes into NO and diethylamine. B. A scheme of the apparatus used to generate NO from DEANO.....	80
Figure 2.30 Tilt (τ), bending (ϕ) and tilt+bend (α) angles for two different ligands with respect to the heme plane.....	83
Figure 2.31 A model used to determine the common area F_c	85
Figure 2.32 A. Protein sample mounted in the capillary for $T > 30^\circ\text{C}$	92
Figure 3.1 Structure of the heme pocket in the three different catalase forms	100
Figure 3.2 Spectral changes of catalase crystals after X-ray exposure (500 nm to 700 nm).....	104
Figure 3.3 A. Raw mean intensities I (solid squares) and $I/\sigma I$ (open squares) as a function of absorbed dose	106
Figure 3.4 The right singular vectors (rSVs) for the two short time-series (1^{st} and 10^{th}).....	109
Figure 3.5 A. Normalized R^{AO} values (black spheres) for rSV1 of all 12 time series as a function of adjusted dose.....	110
Figure 3.6 A. Relaxation times obtained from the SVD analysis (Red squares) and from the posterior analysis (Green triangles) as a function of adjusted dose.....	111
Figure 3.7 A-C. Right singular vectors obtained from the SVD analysis at three different pH's.....	113
Figure 3.8 Extrapolated and difference electron density maps at different pHs. I. pH 7; II. pH 4 and III. pH 9.....	115
Figure 3.9 Chemical kinetic mechanism proposed for the PYP photocycle	118
Figure 3.10 A. Right singular vectors (rSVs) at -40°C . Four kinetic processes with $\tau_1 \dots \tau_4$ (dashed vertical lines) are globally observed	119
Figure 3.11 Dark absorption spectra for PYP in solution (blue) and on a crushed single crystal (red) measured by micro-spectrophotometer	120

Figure 3.12 A. Time-resolved difference absorption spectra from $30\ \mu\text{s}$ – $2\ \text{s}$ for PYP in solution at 295 K	121
Figure 3.13 Time-resolved difference absorption spectra on crystalline slurry at different temperatures	122
Figure 4.1 Structural differences of the PYP chromophore in the pG and blue shifted intermediate state pB	135
Figure 4.2 A schematic setup for a mix and inject time-resolved femtosecond (fs) serial crystallographic experiment at the XFEL	144

LIST OF TABLES

Table 1.1 Noble prizes in the field of X-ray crystallography (Not a complete list).....	3
Table 2.1 Data collection statistics of PYP at different temperatures. Table from Schmidt et al., 2013.	93
Table 2.2 Data collection parameters assigned to different time delays for time-resolved spectroscopic experiments.....	94
Table 3.1 Data collection statistics for the three crystal forms of the catalase. Table from Purwar et al., 2011.....	97
Table 3.2 Number of cavities in some selected proteins. Table from Purwar et al., 2011.....	101
Table 3.3 Tilt+bend angles for NO found in different heme-iron proteins with the iron in different oxidation states (Mb: myoglobin, NP4: nitrophorin 4). Table from Purwar et al., 2011.....	102
Table 3.4 Structural differences in Å relative to Cat-5 averaged over all 4 subunits. Table from Purwar et al., 2011.....	103
Table 3.5 Data statistics for 1 st , 6 th and 12 th time-series after analysis with Precongnition/Epinorm. Table from Schmidt et al., 2012.....	106
Table 3.6 Absorbed doses (in 10 ⁵ Gy) for 12 consecutive time-series, before and after corrections.....	108
Table 3.7 D1/2 and D1/2K derived from uncorrected and corrected dose data. Table from Schmidt et al., 2012.....	111
Table 3.8 Data collection statistics for PYP at three different pH conditions. Δρ denote highest positive and lowest negative difference electron density features in the unit of σ value that is used for the difference maps. Table from Tripathi et al., 2012.	112
Table 3.9 Relaxation times from SVD analysis (τ ₁ & τ ₂). Rate coefficients (k ₁ , k ₂ & k ₃) and their inverse, τρ from the posterior analysis. Table from Tripathi et. al., 2012.	117
Table 3.10 Relaxation times obtained (τ _i) from the fit of rSVs for all temperature settings.....	118
Table 3.11 Relaxation times (τ _i) and corresponding macroscopic rate coefficients (A _i) for PYP in solution and for a crushed single crystal.	123
Table 4.1 On and off rates as well as binding constants (K) for several protein-NO (or CO) complexes. Table from Purwar et al., 2011.	126
Table 4.2 Calculated value of dose limits and employed dose rates for different type of proteins.	132
Table 4.3 Rate of recovery from the signaling state pB to the dark state pG for PYP photocycle determined using time-resolved spectroscopy. The observed rates are compared with those reported by others.	139

ACKNOWLEDGEMENTS

First of all, I would like to thank my PhD supervisor Prof. Marius Schmidt for his great support, not only in scientific development and implementation of novel ideas but also for teaching me to lead a research project independently. Besides that, I would like to acknowledge him for reading and providing comments on my thesis. I would like to thank my committee members Prof. Abbas Ourmzad, Prof. Andy Pacheco, Prof. Dilano Saldin and Prof. Vali Raicu for giving important and useful comments on my thesis.

I thank my collaborators, Prof. Andy Pacheco for his valuable contribution in the catalase project and Dr. Vucika Srajer for her immense support during the experiments at synchrotron beamline. I would like to acknowledge them not only for their extraordinary help in the completion of the research projects but also for their friendly and supportive personality.

I would also like to thank my colleagues for a competitive discussion as well as creating a friendly atmosphere in the laboratories. I would like to acknowledge Jason Tenboer for his contribution in assembling the micro-spectrophotometer, Shailesh Tripathi for providing PYP crystals, Jennifer M. McGarry for her contribution in growing catalase crystals, Sahil Sangani and Lavanya Ramachandran. I thank all my friends for their constant support and encouragements.

Last but not the least, I am grateful to my husband, Vikas Malik for being supportive and encouraging throughout my PhD. I thank my family members for their care, love, motivation and support in difficult times. My deepest regard is to my parents and my brother for being a great source of inspiration and for their immense love and care.

1 Introduction

Proteins and nucleic acids are the most important biomolecules synthesized by living organisms. They are involved in different types of biological functions (Garrett & Grisham, 2009). For example, Deoxyribonucleic acids (DNA) and ribonucleic acids (Adams & Tsien, 1993) store and transmit essential hereditary information. Proteins are the building blocks of life and perpetuate almost all the necessary functions in a living organism. Protein folds into a unique structure which determines its function. Different types of proteins play various and distinct roles (Berg *et al.*, 2001). For example, proteins like elastin, collagen and keratin provide structural support. Contractile proteins such as actin and myosin are involved in motion. Hemoglobin, found in red blood cells, is responsible for oxygen transport from the lungs to the body tissues. Antibodies are produced by the immune system when harmful substances such as bacteria and viruses are detected. Enzymes or bio-catalysts are the most important proteins. They are capable of catalyzing almost all the chemical reactions necessary for living beings (Cornish-Bowden, 2012).

1.1 Enzymes: structure and function

Enzymes are very specific and highly efficient. They catalyze particular reactions in a well-defined manner (Koshland, 1958). Malfunctions of enzymes may cause various types of disorders or diseases (Griffiths A.J.F, 1999, Copeland, 2000). If suitable drugs can be designed and developed, these diseases can be cured. Drug designing is possible only if the enzymes responsible for that particular disease are well understood. Enzymes are complex molecules and their specificity originate from their precise interaction with

their substrate (Koshland, 1958). This precision is a result of the unique three dimensional structure of an enzyme. To get a deeper insight into the structural-functional relationship, it is crucial to determine the atomic structure of an enzyme. For three dimensional structure determinations, X-ray crystallography is the most widely used technique.

1.2 Short history of crystallography

In 1912, Max Von Laue discovered that X-rays can be diffracted by crystals (Von Laue *et al.*, 1913). With Bragg's contribution, father and son, crystallography became a feasible technique for structure determination (Bragg, 1912). The first structure solved was that of simple inorganic salt (Bragg, 1913). In 1923, structures of a few important organic compounds such as hexamethylenetetramine were determined (Dickinson & Raymond, 1923). Several efforts were made to crystallize enzymes. Urease (EC 3.5.1.5) was the first enzyme to be successfully crystallized (Sumner, 1926). Nevertheless, it took more than 40 years from the first inorganic crystal structure to the first protein structure, sperm whale myoglobin (Kendrew *et al.*, 1958). In 1963, the atomic structure of hemoglobin, which is four times larger than myoglobin, was solved (Muirhead & Perutz, 1963). Structures of these proteins provide an insight as to how respiratory systems work. In 1965, the first structure enzyme, lysozyme was obtained (Blake *et al.*, 1965). Crystallography reached another level in 1984 when the structure of the first membrane protein, photosynthetic reaction center from *Rhodospseudomonas viridis*, was determined (Deisenhofer *et al.*, 1984). The structure of the most important rotary molecular machine named as F₁ATP-ase from *bovine heart mitochondria* was solved (Abrahams *et al.*,

1994). Ribosome is one of the largest asymmetric complexes whose structure was solved in 2000 (Wimberly *et al.*, 2000, Ban *et al.*, 2000, Schluenzen *et al.*, 2000). Soon after, the first structure of mammalian G-protein-coupled receptor (GPCR), from *bovine rhodopsin* was determined (Palczewski *et al.*, 2000).

Table 1.1 Nobel prizes in the field of X-ray crystallography (Not a complete list).

Year	Field	Name	Achievements
1914	Physics	Max Von Laue	<i>Diffraction of X-rays by crystals</i>
1915	Physics	W. H. Bragg & W. L. Bragg	<i>Usage of X-rays for structure determination</i>
1946	Chemistry	J. B. Sumner	<i>Crystallization of first enzyme</i>
1962	Chemistry	J. C. Kendrew & M. Perutz	<i>Three dimensional structures of globular proteins</i>
1988	Chemistry	J. Deisenhofer, R. Huber & H. Michel	<i>Atomic structure of the first membrane protein</i>
1997	Chemistry	P. D. Boyer, J. E. Walker & J. C. Skou	<i>Structure and function of first molecular machine (ATP-synthase)</i>
2009	Chemistry	V. Ramakrishnan, T. A. Steitz & A. E. Yonath	<i>High resolution three dimensional structure of ribosome</i>
2012	Chemistry	R. J. Lefkowitz & B. K. Kobilka	<i>Structure of first G-protein-coupled receptor (GPCR)</i>

In the 1980's, time-resolved methods were introduced to the field of crystallography (Moffat, 1989). The technique is based on the Laue method which was originally discovered by Laue back in 1912, however employed by Moffat and coworkers 70 years later. Structural changes were investigated for different type of protein complexes such as Ha-Ras p21 during GTP hydrolysis (Schlichting *et al.*, 1990) and myoglobin-CO complexes during photolysis (Srajer *et al.*, 1996). Over the years, the technique kept developing and reached a matured state in the beginning of the 21st century. Recently, very early events of the trans to cis isomerization in a photoreceptor were successfully elucidated by employing this technique (Jung *et al.*, 2013).

Apart from crystallography, other techniques such as nuclear magnetic resonance (NMR) spectroscopy (Wuthrich, 1990) and electron microscopy (Unwin & Henderson, 1975) are also used to obtain atomic structures. All the atomic structures determined from any of these techniques are stored in the Protein Data Bank (PDB) (Berman *et al.*, 2000). Currently, about 90,000 PDB entries are available, of which 80,000 are solved using crystallographic techniques. Less than 10,000 structures have been solved using either NMR or electron microscopy. This shows that X-ray crystallography has been a major technique for the determination of the three dimensional structures of bio-molecules.

1.3 From static structure to function

Static atomic structures of the macromolecules are obtained from conventional X-ray crystallography. The static information can provide a significant insight about the function; however, for a deeper understanding, one needs to watch a protein in action. For functional investigations of proteins, time-resolved techniques are exquisitely suitable. When an enzyme catalyzes a reaction, several intermediates may form and decay along the reaction pathway. Molecular interactions and motions that occur on a fast time scale can be relatively easily visualized with time-resolved spectroscopic techniques such as fluorescence (Holzwarth, 1995, Millar, 1996), infrared (Schotte *et al.*, 2003, Brudler *et al.*, 2001) and absorption spectroscopy (Topp *et al.*, 1971, van Amerongen & van Grondelle, 1995, van Stokkum *et al.*, 2004). From spectroscopic techniques, one can determine a plausible kinetic mechanism of a catalytic reaction. These spectra may also provide some limited structural information. A technique that combines kinetics and structure determination is time-resolved crystallography (Moffat, 1989).

During the time course of a reaction, subsequent structural changes can be probed with time-resolved crystallographic methods. In a reaction, some of the intermediate states are occupied for a very short period of time and are therefore difficult to detect at ambient temperature. These short-lived states are called metastable states or transient states. It is possible to probe these states, if the life time of the intermediates can be extended for a longer period of time either by lowering the temperature or by adjusting other parameters such as pH (Hajdu *et al.*, 2000, Moffat & Henderson, 1995, Stoddard, 2001). For example, the structures of short-lived intermediates involved in the ligand binding to myoglobin are determined using these trapping approaches (Schlichting *et al.*, 2000, Teng *et al.*, 1994). The disadvantage of trapping techniques is that they may perturb the kinetic mechanism (Moffat & Henderson, 1995). The goal is to study a reaction that evolves freely at physiological temperatures without any perturbation. With modern synchrotron X-ray sources and fast detectors, it is possible to probe intermediates on the order of nanoseconds and faster even at room temperature.

1.4 Catalase

Heme proteins are the most abundant proteins found in living organisms (Bertini I., 1994). They are involved in a number of different biological functions (Berg *et al.*, Paoli *et al.*, 2002). As mentioned above, hemoglobin and myoglobin are responsible for oxygen transport (Antonini & Brunori, 1971, Jain & Chan, 2003). Proteins like cytochrome c oxidase (Wikstrom, 1977) behave as an electron carrier whereas catalase protects the living cells from oxidative damage originating from excess of reactive oxygen species (Deisseroth & Dounce, 1970). These proteins contain heme (Fig. 1.1) in their active sites,

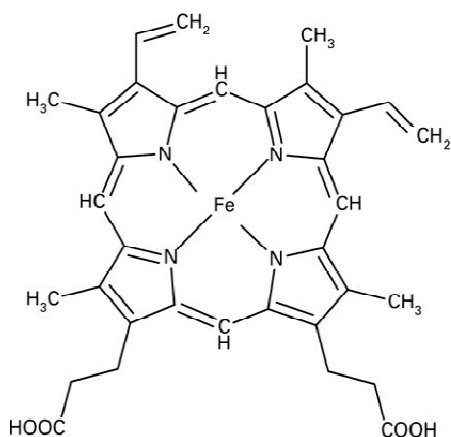


Figure 1.1 Chemical structure of the prosthetic group heme type 'B'. It consists of protoporphyrin IX ring with a central iron (Fe).

which is required for their biological function (Berg *et al.*, 2006). This prosthetic group consists of a heterocycle ring known as protoporphyrin IX with an iron (Fe^{2+}) atom at the center (Fig. 1.1). When a ligand is bound to the heme protein, even slight structural changes in the heme group can significantly affect the protein activity (Paoli *et al.*, 2002). These proteins are excellent for functional study especially if crystallographic methods are used. With the ligand binding approach, not only the function of heme proteins can be understood but also the results can be generalized to different types of proteins.

As mentioned above, catalase (E.C. 1.11.1.6) is a metalloenzyme with heme in its active site. It is found in many bacteria and almost all plants and animals (Murthy *et al.*, 1981). Catalase catalyzes the disproportionation of toxic hydrogen peroxide () into oxygen and water (Eq. 1.1)

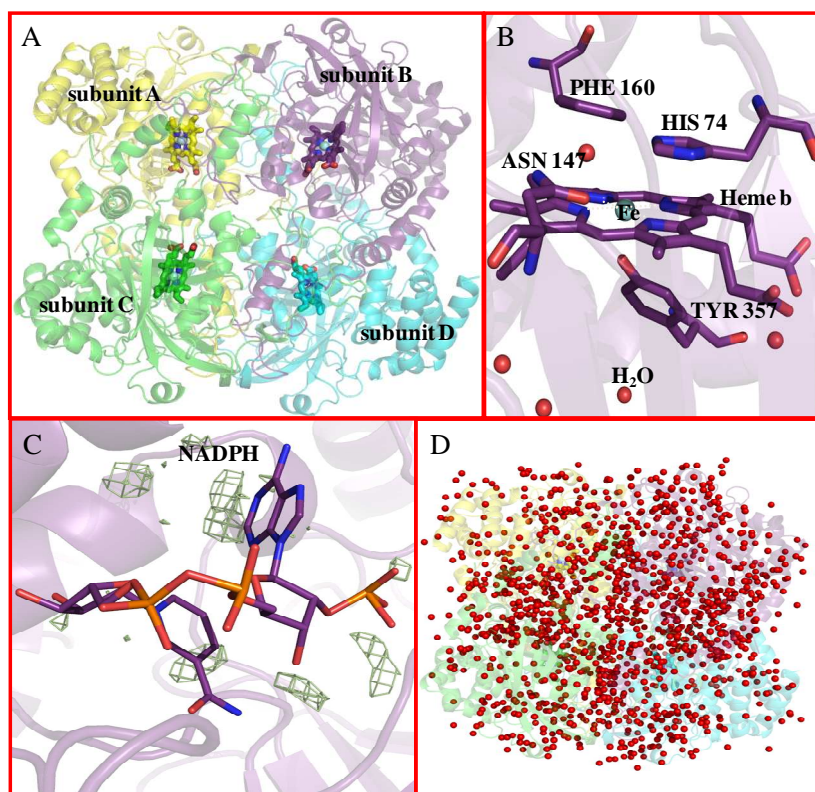
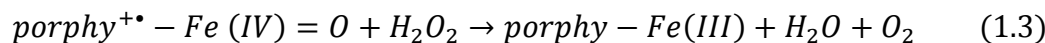
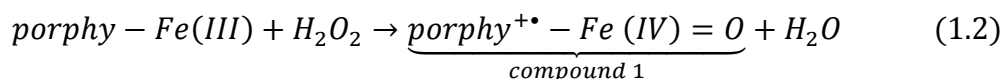


Figure 1.2 Quaternary structure of bovine liver catalase (BLC). **A.** Cartoon representation of BLC. All four subunits are colored differently. The central heme for each subunit is highlighted. **B.** All the important amino acid residues in the vicinity of heme are marked. Oxygen, nitrogen and carbon atoms are marked as red, blue and purple, respectively. Water molecules: red spheres **C.** An electron density observed in our experiments (green), at those regions where other groups have observed NADPH. A putative NADPH molecule is overlaid which shows that the presence of NADPH in our crystal structure is not supported. **D.** Water molecules found in the asymmetric unit of Cat-5 are shown as red spheres. Figure from Purwar *et al.*, 2011.

This reaction is very important to all aerobically respiring organisms. Reactive oxygen species like O_2^{2-} and O_2^- (superoxide) are inevitable byproducts of aerobic respiration, necessitating specialized enzymes for their elimination (Aebi, 1984, Halliwell & Gutteridge, 1990, Michiels *et al.*, 1994). Typical examples for mammalian catalase are bovine liver catalase, BLC (Ko *et al.*, 1999) and human erythrocyte catalase, HEC (Ko *et al.*, 2000).

BLC was crystallized for the first time in 1937 (Sumner & Dounce, 1937) and its crystal structure was determined in 1981 (Murthy *et al.*, 1981). The quality of atomic models have been subsequently improved (Reid *et al.*, 1981, Ko *et al.*, 1999). BLC is a tetramer (Fig. 1.2A) (Tanford & Lovrien, 1962, Sund *et al.*, 1967). Each of the four monomers (MW~60 KDa) consist (ASK) of 507 amino acid residues and contains a heme group (Fig. 1.2B) with the iron in the ferric state (Fe^{3+}) (Torii *et al.*, 1970, Stern, 1936, Schroeder *et al.*, 1982).

Several mechanisms have been proposed for BLC catalysis (Fita & Rossmann, 1985, Alfonso-Prieto *et al.*, 2007). Among these, the Fita-Rossmann model is the most widely accepted. Based on this model, the reaction involves a transfer of a total of four electrons in two major steps. First, two electrons are transferred from the porphyrin complex to one molecule of H_2O_2 and then two electrons are accepted from a second H_2O_2 molecule (Eq. 1.2 & 1.3). Compound 1 forms in the first part of the reaction (Eq. 1.2) and attacks another H_2O_2 molecule abstracting a hydride ion (H^-) and leaving a hydroxyl ion (OH^-) at the iron position (Fita & Rossmann, 1985). Iron itself becomes Fe(III) and one electron is transferred back to the porphyrin. A proton temporarily stored at the N atom of His 74 (Fig. 1.2B) is then transferred to the OH^- at the iron site. This leads to the formation of a water molecule, which is very weakly bound to the iron and can be quickly released (Eq. 1.3).



Within the active enzyme, the Cat-H₂O₂ adduct, the so called compound 1 (see above), is not sufficiently long-lived to be structurally characterized. Various types of ligands such as azide (Murshudov *et al.*, 2002), formate (Andreoletti *et al.*, 2003), oxo (compound I and II) (Gouet *et al.*, 1996, Alfonso-Prieto *et al.*, 2007), cyanide and 3-amino-1,2,4-Triazol (Putnam *et al.*, 2000) can be bound to the heme iron. These active site's adducts are prepared to gain an insight into the structural information about the intermediates crucial to the catalytic mechanism. If nitric oxide (NO) can be successfully bound to the catalase, the Cat-NO adduct may mimic compound 1.

NO as a ligand has been bound to the other heme proteins such as leghemoglobin Lb (Rohlfs *et al.*, 1988), Myoglobin Mb (Rohlfs *et al.*, 1988, Laverman *et al.*, 2001) and nitrophorin NP (Andersen *et al.*, 2000). Several complexes have been developed and implemented for a controlled release of NO in biological systems (Maragos *et al.*, 1991). Despite this fact, the structure of the Cat-NO complex has never been characterized before because nitric oxide tends to dissociate rapidly from the crystals. Here, we aimed at the structure determination of the nitrosylated-BLC complex using monochromatic crystallography.

1.5 PYP

As described above, heme proteins such as catalase are ideal for static structure determinations. Ligand binding to these proteins can provide an insight into the function of proteins. Our goal, however, is to investigate the dynamic behavior of the biomolecules in general. We need to develop techniques that can be applied to various types of biological systems. For this, a well-understood model system is required. Photoactive

yellow protein (PYP) provides such a model reaction that evolves with several intermediates at ambient temperatures. Apart from that, PYP crystals of small size and high stability make this protein an excellent model system for investigating functional behavior. PYP and its photocycle are now described in detail.

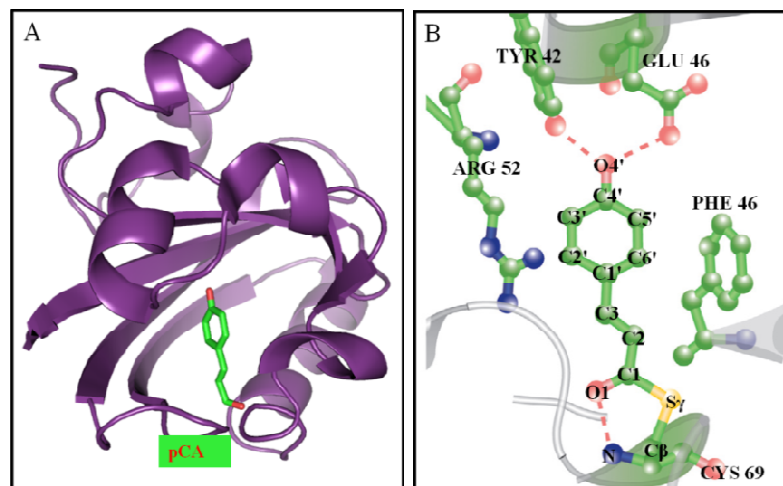


Figure 1.3 **A.** Cartoon representation of the photoactive yellow protein (in violet). The para-coumaric acid chromophore (pCA; colored green) is embedded into the protein. **B.** The chromophore and its nearby residues that play a crucial role in the photocycle. Panel B from Jung *et al.*, 2013.

PYP (Meyer, 1985) is a water-soluble protein with a molecular weight of 14kDa. It is initially isolated from the bacterium *Halorhodospira* (formerly *Ectothiorhodospira*) *halophila*. The X-ray structure of PYP (Fig. 1.3A) (Borgstahl *et al.*, 1995) shows that it shares a common structural motif with the typical PAS domain family (Meyer, 1985, Pellequer *et al.*, 1998). The para-coumaric acid (pCA) chromophore (Fig. 1.3) is embedded into this domain and is believed to play a key role in the negative phototactic effects (Sprenger *et al.*, 1993) in the various photosynthetic bacteria (Kort *et al.*, 1996). The chromophore is covalently attached to Cys69 through a thioester bond and forms

hydrogen bonds with amino acid residues Tyr42, Glu46 and with backbone amide of Cys69 (Fig. 1.3B) (Van Beeumen *et al.*, 1993).

Upon absorption of a blue photon, PYP enters into a fully reversible photocycle with several intermediates ranging from picoseconds to seconds (Fig. 1.4). The photocycle has been studied extensively with various time-resolved techniques such as UV-Vis absorption spectroscopy (Meyer *et al.*, 1989, Hoff *et al.*, 1994, Imamoto *et al.*, 2001, Ujj *et al.*, 1998), Fourier transform infrared spectroscopy (Brudler *et al.*, 2001, Imamoto *et al.*, 2001, van Wilderen *et al.*, 2006), NMR spectroscopy (Rubinstenn *et al.*, 1998), resonance Raman spectroscopy (Pan *et al.*, 2004) and Laue crystallography (Genick *et al.*, 1998, Schmidt *et al.*, 2004, Ren *et al.*, 2001, Ihee *et al.*, 2005, Rajagopal *et al.*, 2005, Schotte *et al.*, 2012, Jung *et al.*, 2013). In some cases, it is possible that PYP may not successfully enter into the photocycle even after absorbing a blue light photon (Groot *et al.*, 2003, van Wilderen *et al.*, 2006). As a result, a ground state intermediate (GSI, Grey part of Fig. 1.4A) forms on the femtosecond time scale and decays to the ground state (pG) in ~6 ps. The GSI was revealed by ultrafast infrared spectroscopy; however, the structure of this intermediate is still elusive because time-resolved crystallographic methods at ambient temperatures are lacking the time resolution that is required to capture the GSI intermediate.

The nomenclature used for the intermediates associated with this photocycle (Fig. 1.4A) is the same as used in earlier studies (Jung *et al.*, 2013, Genick *et al.*, 1997a, Ihee *et al.*, 2005, Kim *et al.*, 2012). When a protein crystal is illuminated with a photon of 485 nm, an electron jumps to an excited state. A part of the energy is immediately dissipated

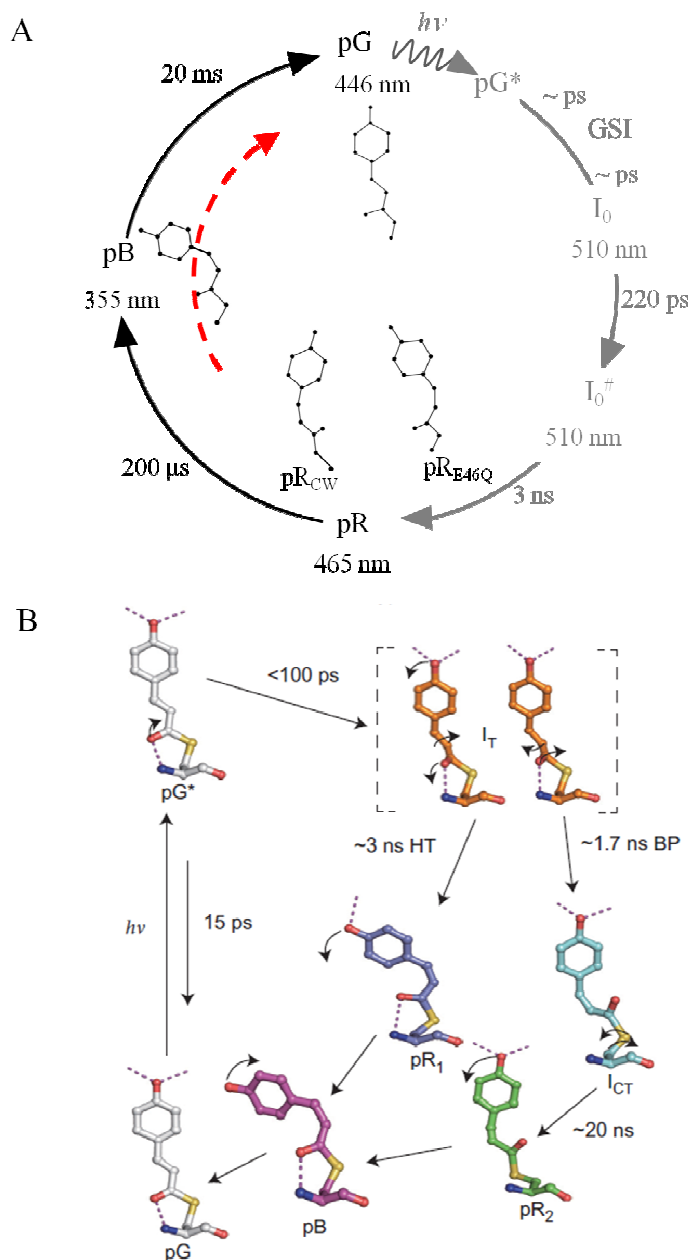


Figure 1.4 A. Photoactive yellow protein (PYP) photocycle. Solid black curves: part of the photocycle used to investigate the effect of pH on the structures, Red dashed curve: part of the photocycle used to examine the impact of radiation damage on the protein crystal. Figure from Schmidt et al., 2012 **B.** A photocycle consistent with WT-PYP time-resolved electron-density maps. Carbon atoms of the refined pG, I_T , I_{CT} , pR1, pR2 and pB intermediate structures are shown in grey, orange, cyan, dark blue, green, and purple, respectively. Oxygen, sulfur and nitrogen atoms are shown in red, yellow and blue, respectively. The arrows indicate large atomic movements from one intermediate to the next. Figure from Jung et al., 2013.

(Martin *et al.*, 1983) and the remaining energy triggers the photo-isomerization of the chromophore. A theoretical calculation performed on WT-PYP and its mutant, E46Q, revealed that the earliest intermediate I_T forms in less than 100 ps (Groenhof *et al.*, 2004). The structure of I_T (Fig. 1.4B) was recently determined by time-resolved crystallography (Jung *et al.*, 2013, Schotte *et al.*, 2012). It resembles the spectroscopically observed intermediate I_o (Fig. 1.4A) (Imamoto *et al.*, 2001, Unno *et al.*, 2004). This intermediate is not fully transformed into the *cis* conformation and exists in a highly strained state (Schotte *et al.*, 2012, Jung *et al.*, 2013, van Stokkum *et al.*, 2004). The remaining isomerization of the I_T cannot occur through the standard mechanism (Liu & Asato, 1985), because the chromophore is buried within the host protein and therefore interacts with surrounding side chains (Borgstahl *et al.*, 1995). This severely restricts the conformational mobility of the chromophore and imposes spatial constraints on it (Liu & Asato, 1985, Warshel & Barboy, 1982). Therefore, the isomerization pathway proceeds through a volume-conserving mechanism (Müller *et al.*, 1998, Liu *et al.*, 2007). The distorted intermediate I_T bifurcates into two structurally distinct *cis* intermediates I_{CT} and pR_1 (Fig. 1.4B). I_{CT} forms in 1.7 ns via a bicycle-pedal (BP) mechanism (Xie *et al.*, 1996, Genick *et al.*, 1998, Ren *et al.*, 2001, Groot *et al.*, 2003, Ihee *et al.*, 2005, van Wilderen *et al.*, 2006, Imamoto *et al.*, 2002) whereas pR_1 forms via a hula twist (HT) mechanism (Liu & Asato, 1985, Andresen *et al.*, 2005) with a life time of ~ 3 ns. The mixture of these two *cis*-intermediates is similar to the spectroscopically observed intermediate $I_o^\#$ (Fig. 1.4A). In I_{CT} the carbonyl-oxygen is flipped to the other side but the chromophore head is fixed by hydrogen bonds to Tyr42 and Glu46. In pR_1 the chromophore head hydroxyl loses one hydrogen bond. The highly strained intermediate I_{CT} relaxes to pR_2 . Both

intermediates pR1 and pR2 form in parallel (Tripathi *et al.*, 2012). The pR1 and pR2 resemble the intermediates pR_{E46Q} and pR_{CW} observed from the nanosecond crystallographic studies, respectively (Ihee *et al.*, 2005, Rajagopal *et al.*, 2005). In pR1, the hydrogen bonds to the Tyr 42 and backbone amide of Cys69 are maintained and that to the Glu46 is broken (Fig. 1.4B). On the other hand, the chromophore in pR2 maintains the hydrogen bonds to Tyr42 and Glu46 and loses the hydrogen bond to the backbone amide of Cys69. The mixture of pR1 and pR2 is equivalent to spectroscopic intermediate, pR (Fig. 1.4A), which absorbs in the range of 465 nm whereas the dark state absorbs at 446nm (Ujj *et al.*, 1998, Hoff *et al.*, 1994). Both intermediates pR1 and pR2 ultimately decay in ~200 μ s to the long lived signaling state pB, which absorbs at 355nm (Fig. 1.4) (Schmidt *et al.*, 2004, Ihee *et al.*, 2005). The chromophore head forms new hydrogen bonds with the displaced Arg52 and with an additional water that appears near the entrance to the chromophore pocket (Fig. 3.8 I.G). The phenolate oxygen and Arg52 are exposed to the solvent. At the end of the photocycle, this blue shifted intermediate reverts to its initial dark state on the millisecond time scale. When the protein structure relaxes back to the dark state, all the hydrogen bonds are re-established. The system has been thoroughly studied; however, it is unknown how this protein reacts at different parameters such as pH, temperature and X-ray dose. We investigate the effects of these parameters on the protein kinetics using time-resolved crystallographic methods.

1.6 Effect of X-rays doses on PYP

In X-ray crystallography, a protein crystal is repeatedly exposed to X-ray radiation during data collection. These exposures can potentially damage the protein and affect its

dynamics (Dubnovitsky *et al.*, 2005, Adam *et al.*, 2004, Purwar *et al.*, 2011, Schlichting *et al.*, 2000). At cryogenic temperatures, the dose limit up to which meaningful data can be collected is also known as Henderson's limit (Henderson, 1990). Below a threshold of approximately 2×10^7 Gy, the damages are not substantial because up to this limit the damage varies linearly with X-ray dose (Teng & Moffat, 2000). Above this limit, damages start to accumulate and can cause excessive damage to the protein crystals. In order to reduce the radiation damage, different types of techniques such as cryo-cooling (Kuzay *et al.*, 2001, Nicholson *et al.*, 2001) and the usage of a free-radicals scavenger (Murray & Garman, 2002) have been developed. At room temperature, protein crystals are even more susceptible to radiation damage. The damaging effects of X-rays on the kinetics of a protein have never been quantified before. Apart from X-rays, laser pulses employed in a time-resolved experiment (Moffat, 1989) may also destroy the protein crystals. Here, we performed time-resolved crystallographic experiments to assess the impact of not only X-ray doses but also laser pulses on the structural and kinetic analysis of PYP. This investigation shows how many data sets can be collected from a single crystal of PYP without affecting the kinetics.

1.7 Effect of pH on the PYP

The pCA chromophore is de-protonated and present in its anionic form when PYP is in the ground state (Baca *et al.*, 1994, Borgstahl *et al.*, 1995, Kim *et al.*, 1995). Upon entering into a photocycle (Fig. 1.4A), the net uptake of one proton is involved during the life time of the intermediate pB (Meyer *et al.*, 1993). The protonation of the chromophore may be responsible for the blue-shift of ~95 nm of the pB state (~355 nm) with respect to

the pG state (~446 nm) (Fig. 4.1). The transfer of protons takes place either from the Glu-46 (Baca *et al.*, 1994, Hendriks *et al.*, 1999) or from the solvent (Borucki *et al.*, 2002, Genick *et al.*, 1997b). Protonation and deprotonation of the chromophore as well as nearby amino acid residues may lead to pH- or salt-dependent protein activity (Genick *et al.*, 1997b, Hoff *et al.*, 1997, Harigai *et al.*, 2003). For native PYP, the photo bleaching which corresponds to the pR \rightarrow pB transition is slightly accelerated at low pH conditions (Genick *et al.*, 1997b, Demchuk *et al.*, 2000). On the other hand, recovery to the dark state (pB \rightarrow pG) is the fastest at pH 8 and decreases for all other pH conditions (Genick *et al.*, 1997b, Demchuk *et al.*, 2000). These studies show that the pH has a pronounced effect on the kinetics of the photocycle. Although it has been widely investigated using spectroscopic techniques, the effect of pH on the structures of reaction intermediates on the atomic length scale is still elusive. In this thesis, time-resolved crystallography is employed to investigate these effects.

1.8 Effect of temperature on PYP

In addition to the external parameters such as X-ray dose and pH, temperature also affects the kinetics of PYP. Several time-resolved spectroscopic studies have been performed on PYP at one (Meyer *et al.*, 1987, Genick *et al.*, 1997b, Imamoto *et al.*, 1996, Ujj *et al.*, 1998, Unno *et al.*, 2002, Meyer *et al.*, 1989) or at a few different temperature settings (Hellingwerf *et al.*, 2003, Van Brederode *et al.*, 1996). For example, picoseconds time-resolved crystallographic measurements were recently performed on PYP at room temperature (Jung *et al.*, 2013, Schotte *et al.*, 2012). This ps study thoroughly describes the isomerization pathways and provides structural information of earlier intermediates.

A detailed investigation how the temperature affects the structure and kinetics of the PYP photocycle has never been performed. Here, we employ time-resolved crystallography to investigate the photocycle rigorously at 14 different temperature settings starting from -40 °C to 70 °C (Schmidt *et al.*, 2013).

The functional study at different temperatures can also be performed using time-resolved spectroscopy. This enables us to investigate the protein kinetics with two different but widely used techniques. The results obtained from the two complementary techniques can be compared to explore the similarities and differences in the kinetic behavior. These experiments have never been previously accomplished due to unavailability of a suitable micro-spectrophotometer that can probe the spectroscopic changes on fast time scales in a temperature-controlled environment. In our lab, we designed a fast spectrophotometer fulfilling all of the aforementioned requirements. This spectrophotometer is employed to investigate the PYP photocycle at different temperatures. The function of a protein may be different in solution as compared to its crystalline phase (Yeremenko *et al.*, 2006). To determine these differences, we also performed time-resolved spectroscopic experiments on PYP in solution.

The rates of chemical reactions depend on the temperature. Their temperature dependence can be described using Van't Hoff-Arrhenius equation, which is given by

$$\Lambda = v \exp\left(-\frac{E_a}{k_B T}\right) \quad (1.4)$$

where Λ is the macroscopic rate coefficient, v is the prefactor, E_a is the energy of activation, k_B is the Boltzmann factor and T is the temperature. Eyring (Eyring, 1935) tied this equation to a transition state at top of the barrier of activation. This is

represented as a transition state equation (Eq. 4.1), which is further described in the discussion. With this information, extracting the energetics of a biomolecular reaction has been a topic of interest and has also been challenging. So far only limited information is available (Takeshita *et al.*, 2002). Here, we show how thermodynamic properties such as enthalpy, entropy and Gibbs free energy of the barrier can be extracted solely from the temperature dependent crystallographic data.

References

- Abrahams, J. P., Leslie, A. G., Lutter, R. & Walker, J. E. (1994). *Nature* **370**, 25.
- Adam, V., Royant, A., Niviere, V., Molina-Heredia, F. P. & Bourgeois, D. (2004). *Structure* **12**, 1729-1740.
- Adams, S. R. & Tsien, R. Y. (1993). *Annual Review of Physiology* **55**, 755-784.
- Aebi, H. (1984). *Meth. Enzymol.* **105**, 121-127.
- Alfonso-Prieto, M., Borovik, A., Carpena, X., Murshudov, G., Melik-Adamyanyan, W., Fita, I., Rovira, C. & Loewen, P. C. (2007). *J. Am. Chem. Soc.* **129**, 4193-4205.
- Andersen, J. F., Ding, X. D., Balfour, C., Shokhireva, T. K., Champagne, D. E., Walker, F. A. & Montfort, W. R. (2000). *Biochemistry* **39**, 10118-10131.
- Andreoletti, P., Sainz, G., Jaquinod, M., Gagnon, J. & Jouve, H. M. (2003). *Prot. Struct. Func. Gen.* **50**, 261-271.
- Andresen, M., Wahl, M. C., Stiel, A. C., Gräter, F., Schäfer, L. V., Trowitzsch, S., Weber, G., Eggeling, C., Grubmüller, H. & Hell, S. W. (2005). *Proceedings of the National Academy of Sciences of the United States of America* **102**, 13070-13074.
- Antonini, E. & Brunori, M. (1971). *Hemoglobin and Myoglobin in their Reactions with Ligands*. North-Holland Amsterdam.
- Baca, M., Borgstahl, G. E., Boissinot, M., Burke, P. M., Williams, D. R., Slater, K. A. & Getzoff, E. D. (1994). *Biochemistry* **33**, 14369-14377.
- Ban, N., Nissen, P., Hansen, J., Moore, P. B. & Steitz, T. A. (2000). *Science* **289**, 905-920.
- Berg, J., Tymoczko, J. & Stryer, L. (2001). *Biochemistry* 5ed. 2001: WH Freeman and Company.
- Berg, J. M., Tymoczko, J. L. & Stryer, L. (2006). *Biochemistry, International Edition*. WH Freeman & Co. New York.
- Berman, H. M., Westbrook, J., Feng, Z., Gilliland, G., Bhat, T. N., Weissig, H., Shindyalov, I. N. & Bourne, P. E. (2000). *Nucleic Acids Res.* **28**, 235-242.
- Bertini, I., G. H. B., Lippard, S. J., Valentine, J. S., (1994). *University Science Books, Sausalito, CA*.
- Blake, C., Koenig, D., Mair, G., North, A., Phillips, D. & Sarma, V. (1965). *Nature* **206**, 757-761.
- Borgstahl, G. E., Williams, D. R. & Getzoff, E. D. (1995). *Biochemistry* **34**, 6278-6287.

- Borucki, B., Devanathan, S., Otto, H., Cusanovich, M. A., Tollin, G. & Heyn, M. P. (2002). *Biochemistry* **41**, 10026-10037.
- Bragg, W. (1913). *Proceedings of the Royal Society of London. Series A* **89**, 248-277.
- Bragg, W. L. (1912). *Nature* **90**, 410.
- Brudler, R., Rammelsberg, R., Woo, T. T., Getzoff, E. D. & Gerwert, K. (2001). *Nature structural biology* **8**, 265-270.
- Copeland, R. A. (2000). *Enzymes: A Practical Introduction to Structure, Mechanism, and Data Analysis, Second Edition*, 109-145.
- Cornish-Bowden, A. (2012). *Fundamentals of Enzyme Kinetics*, 4 edition ed. Wiley-VCH.
- Deisenhofer, J., Epp, O., Miki, K., Huber, R. & Michel, H. (1984). *Journal of molecular biology* **180**, 385-398.
- Deisseroth, A. & Dounce, A. L. (1970). *Physiol Rev* **50**, 319-375.
- Demchuk, E., Genick, U. K., Woo, T. T., Getzoff, E. D. & Bashford, D. (2000). *Biochemistry* **39**, 1100-1113.
- Dickinson, R. G. & Raymond, A. L. (1923). *Journal of the American Chemical Society* **45**, 22-29.
- Dubnovitsky, A. P., Ravelli, R. B. G., Popov, A. N. & Papageorgiou, A. C. (2005). *Protein Sci* **14**, 1498-1507.
- Fita, I. & Rossmann, M. G. (1985). *Proc. Natl. Acad. Sci. USA* **82**, 1604-1608.
- Garrett, R. & Grisham, C. (2009). *Inc: Boston*.
- Genick, U. K., Borgstahl, G. E., Ng, K., Ren, Z., Pradervand, C., Burke, P. M., Srajer, V., Teng, T. Y., Schildkamp, W., McRee, D. E., Moffat, K. & Getzoff, E. D. (1997a). *Science* **275**, 1471-1475.
- Genick, U. K., Devanathan, S., Meyer, T. E., Canestrelli, I. L., Williams, E., Cusanovich, M. A., Tollin, G. & Getzoff, E. D. (1997b). *Biochemistry* **36**, 8-14.
- Genick, U. K., Soltis, S. M., Kuhn, P., Canestrelli, I. L. & Getzoff, E. D. (1998). *Nature* **392**, 206-209.
- Gouet, P., Jouve, H.-M., Williams, P. A., Andersson, I., Andreoletti, P., Nussaume, L. & Hajdu, J. (1996). *Nat. Struct. Biol.* **3**, 951-956.
- Griffiths A.J.F, G. W. M., Miller J.H. (1999). *New York: W. H. Freeman*.
- Groenhof, G., Bouxin-Cademartory, M., Hess, B., De Visser, S. P., Berendsen, H. J., Olivucci, M., Mark, A. E. & Robb, M. A. (2004). *J Am Chem Soc* **126**, 4228-4233.
- Groot, M. L., van Wilderen, L. J. G. W., Larsen, D. S., van der Horst, M. A., van Stokkum, I. H. M., Hellingwerf, K. J. & van Grondelle, R. (2003). *Biochemistry* **42**, 10054-10059.
- Hajdu, J., Neutze, R., Sjogren, T., Edman, K., Szoke, A., Wilmouth, R. C. & Wilmot, C. M. (2000). *Nat Struct Biol* **7**, 1006-1012.
- Halliwel, B. & Gutteridge, J. M. C. (1990). *Meth. Enzymol.* **186**, 1-85.
- Harigai, M., Imamoto, Y., Kamikubo, H., Yamazaki, Y. & Kataoka, M. (2003). *Biochemistry* **42**, 13893-13900.
- Hellingwerf, K. J., Hendriks, J. & Gensch, T. (2003). *The Journal of Physical Chemistry A* **107**, 1082-1094.
- Henderson, R. (1990). *Proc. R. Soc. Lond.* **B241**, 6-8.
- Hendriks, J., Hoff, W. D., Crielaard, W. & Hellingwerf, K. J. (1999). *The Journal of biological chemistry* **274**, 17655-17660.
- Hoff, W. D., van Stokkum, I. H., van Ramesdonk, H. J., van Brederode, M. E., Brouwer, A. M., Fitch, J. C., Meyer, T. E., van Grondelle, R. & Hellingwerf, K. J. (1994). *Biophysical journal* **67**, 1691-1705.
- Hoff, W. D., Van Stokkum, I. H. M., Gural, J. & Hellingwerf, K. J. (1997). *Bba-Bioenergetics* **1322**, 151-162.
- Holzwarth, A. R. (1995). *Methods Enzymol* **246**, 334-362.

- Ihee, H., Rajagopal, S., Srajer, V., Pahl, R., Anderson, S., Schmidt, M., Schotte, F., Anfinrud, P. A., Wulff, M. & Moffat, K. (2005). *Proceedings of the National Academy of Sciences of the United States of America* **102**, 7145-7150.
- Imamoto, Y., Kataoka, M. & Liu, R. S. H. (2002). *Photochem Photobiol* **76**, 584-589.
- Imamoto, Y., Kataoka, M. & Tokunaga, F. (1996). *Biochemistry* **35**, 14047-14053.
- Imamoto, Y., Shirahige, Y., Tokunaga, F., Kinoshita, T., Yoshihara, K. & Kataoka, M. (2001). *Biochemistry* **40**, 8997-9004.
- Jain, R. & Chan, M. K. (2003). *JBIC Journal of Biological Inorganic Chemistry* **8**, 1-11.
- Jung, Y. O., Lee, J. H., Kim, J., Schmidt, M., Moffat, K., Srajer, V. & Ihee, H. (2013). *Nature chemistry* **5**, 212-220.
- Kendrew, J. C., Bodo, G., Dintzis, H. M., Parrish, R., Wyckoff, H. & Phillips, D. (1958). *Nature* **181**, 662-666.
- Kim, M., Mathies, R. A., Hoff, W. D. & Hellingwerf, K. J. (1995). *Biochemistry* **34**, 12669-12672.
- Kim, T. W., Lee, J. H., Choi, J., Kim, K. H., van Wilderen, L. J., Guerin, L., Kim, Y., Jung, Y. O., Yang, C., Kim, J., Wulff, M., van Thor, J. J. & Ihee, H. (2012). *J Am Chem Soc* **134**, 3145-3153.
- Ko, T. P., Day, J., Malkin, A. J. & McPherson, A. (1999). *Acta Cryst. D* **55**, 1383-1394.
- Ko, T. P., Safo, M. K., Musayev, F. N., Di Salvo, M. L., Wang, C. Q., Wu, S. H. & Abraham, D. J. (2000). *Acta Cryst. D* **56**, 241-245.
- Kort, R., Vonk, H., Xu, X., Hoff, W., Crielaard, W. & Hellingwerf, K. (1996). *FEBS letters* **382**, 73-78.
- Koshland, J., D.E. (1958). *Proceedings of the National Academy of Sciences of the United States of America* **44**(2), 98-104.
- Kuzay, T. M., Kazmierczak, M. & Hsieh, B. J. (2001). *Acta crystallographica. Section D, Biological crystallography* **57**, 69-81.
- Laverman, L. E., Wanat, A., Oszejka, J., Stochel, G., Ford, P. C. & van Eldik, R. (2001). *J. Am. Chem. Soc.* **123**, 285-293.
- Liu, R. & Asato, A. E. (1985). *Proceedings of the National Academy of Sciences* **82**, 259-263.
- Liu, R. S. H., Yang, L.-Y. & Liu, J. (2007). *Photochem Photobiol* **83**, 2-10.
- Maragos, C. M., Morley, D., Wink, D. A., Dunams, T. M., Saavedra, J. E., Hoffman, A., Bove, A. A., Isaac, L., Hrabie, J. A. & Keefer, L. K. (1991). *Journal of medicinal chemistry* **34**, 3242-3247.
- Martin, J. L., Migus, A., Poyart, C., Lecarpentier, Y., Astier, R. & Antonetti, A. (1983). *Proceedings of the National Academy of Sciences of the United States of America* **80**, 173-177.
- Meyer, T. E. (1985). *Biochimica et biophysica acta* **806**, 175-183.
- Meyer, T. E., Cusanovich, M. A. & Tollin, G. (1993). *Arch Biochem Biophys* **306**, 515-517.
- Meyer, T. E., Tollin, G., Hazzard, J. H. & Cusanovich, M. A. (1989). *Biophysical journal* **56**, 559-564.
- Meyer, T. E., Yakali, E., Cusanovich, M. A. & Tollin, G. (1987). *Biochemistry* **26**, 418-423.
- Michiels, C., Raes, M., Toussaint, O. & Remacle, J. (1994). *Free-Rad. Biol. Med.* **17**, 235-248.
- Millar, D. P. (1996). *Current opinion in structural biology* **6**, 637-642.
- Moffat, K. (1989). *Annual review of biophysics and biophysical chemistry* **18**, 309-332.
- Moffat, K. & Henderson, R. (1995). *Current opinion in structural biology* **5**, 656-663.
- Muirhead, H. & Perutz, M. F. (1963). *Cold Spring Harbor Symposia on Quantitative Biology* **28**, 8.
- Müller, A. M., Lochbrunner, S., Schmid, W. E. & Fuß, W. (1998). *Angewandte Chemie International Edition* **37**, 505-507.

- Murray, J. & Garman, E. (2002). *J Synchrotron Radiat* **9**, 347-354.
- Murshudov, G. N., Grebenko, A. I., Brannigan, J. A., Antson, A. A., Barynin, V., Dodson, G. G., Dauter, Z., Wilson, K. S. & Melik-Adamyany, W. R. (2002). *Acta Cryst. D* **58**, 1972-1982.
- Murthy, M. R., Reid, T. J., Sicignano, A., Tanaka, N. & Rossmann, M. G. (1981). *J Mol Biol* **152**, 465-499.
- Nicholson, J., Nave, C., Fayz, K., Fell, B. & Garman, E. (2001). *Nucl Instrum Meth A* **467**, 1380-1383.
- Palczewski, K., Kumasaka, T., Hori, T., Behnke, C. A., Motoshima, H., Fox, B. A., Trong, I. L., Teller, D. C., Okada, T. & Stenkamp, R. E. (2000). *Science Signaling* **289**, 739.
- Pan, D., Philip, A., Hoff, W. D. & Mathies, R. A. (2004). *Biophysical journal* **86**, 2374-2382.
- Paoli, M., Marles-Wright, J. & Smith, A. (2002). *DNA Cell Biol* **21**, 271-280.
- Pellequer, J. L., Wager-Smith, K. A., Kay, S. A. & Getzoff, E. D. (1998). *Proceedings of the National Academy of Sciences of the United States of America* **95**, 5884-5890.
- Purwar, N.**, McGarry, J. M., Kostera, J., Pacheco, A. A. & Schmidt, M. (2011). *Biochemistry* **50**, 4491-4503.
- Putnam, C. D., Arvai, A. S., Bourne, Y. & Tainer, J. A. (2000). *J. Mol. Biol.* **296**, 295-309.
- Rajagopal, S., Anderson, S., Srajer, V., Schmidt, M., Pahl, R. & Moffat, K. (2005). *Structure* **13**, 55-63.
- Reid, T. J., Murthy, M. R. N., Sicignano, A., Tanaka, N., Musick, W. D. L. & Rossmann, M. G. (1981). *Proc. Natl. Acad. Sci. USA* **78**, 4767-4771.
- Ren, Z., Perman, B., Srajer, V., Teng, T. Y., Pradervand, C., Bourgeois, D., Schotte, F., Ursby, T., Kort, R., Wulff, M. & Moffat, K. (2001). *Biochemistry* **40**, 13788-13801.
- Rohlf, R. J., Gibson, J. S. & Gibson, O. H. (1988). *J. Biol. Chem.* **263**, 1803-1813.
- Rubinstenn, G., Vuister, G. W., Mulder, F. A., Dux, P. E., Boelens, R., Hellingwerf, K. J. & Kaptein, R. (1998). *Nature structural biology* **5**, 568-570.
- Schlichting, I., Almo, S. C., Rapp, G., Wilson, K., Petratos, K., Lentfer, A., Wittinghofer, A., Kabsch, W., Pai, E. F. & Petsko, G. A. (1990).
- Schlichting, I., Berendzen, J., Chu, K., Stock, A. M., Maves, S. A., Benson, D. E., Sweet, R. M., Ringe, D., Petsko, G. A. & Sligar, S. G. (2000). *Science* **287**, 1615-1622.
- Schluenzen, F., Tocilj, A., Zarivach, R., Harms, J., Gluehmann, M., Janell, D., Bashan, A., Bartels, H., Agmon, I. & Franceschi, F. (2000). *Cell* **102**, 615-623.
- Schmidt, M., Pahl, R., Srajer, V., Anderson, S., Ren, Z., Ihee, H., Rajagopal, S. & Moffat, K. (2004). *Proceedings of the National Academy of Sciences of the United States of America* **101**, 4799-4804.
- Schmidt, M., Srajer, V., Henning, R., Ihee, H., **Purwar, N.**, Tenboer, J. & Tripathi, S. (2013). *J Am Chem Soc*, submitted.
- Schotte, F., Cho, H. S., Kaila, V. R., Kamikubo, H., Dashdorj, N., Henry, E. R., Graber, T. J., Henning, R., Wulff, M., Hummer, G., Kataoka, M. & Anfinrud, P. A. (2012). *Proceedings of the National Academy of Sciences of the United States of America* **109**, 19256-19261.
- Schotte, F., Lim, M., Jackson, T. A., Smirnov, A. V., Soman, J., Olson, J. S., Phillips, G. N., Jr., Wulff, M. & Anfinrud, P. A. (2003). *Science* **300**, 1944-1947.
- Schroeder, W. A., Shelton, J. R., Shelton, J. B., Robberson, B., Apell, G., Fang, R. S. & Bonaventura, J. (1982). *Arch. Biochem. Biophys.* **214**, 397-421.
- Sprenger, W. W., Hoff, W. D., Armitage, J. P. & Hellingwerf, K. J. (1993). *J Bacteriol* **175**, 3096-3104.
- Srajer, V., Teng, T. Y., Ursby, T., Pradervand, C., Ren, Z., Adachi, S., Schildkamp, W., Bourgeois, D., Wulff, M. & Moffat, K. (1996). *Science* **274**, 1726-1729.
- Stern, K. G. (1936). *J. Biol. Chem.* **112**, 661-669.

- Stoddard, B. L. (2001). *Methods* **24**, 125-138.
- Sumner, J. B. (1926). *Journal of Biological Chemistry* **69**, 435-441.
- Sumner, J. B. & Dounce, A. L. (1937). *J. Biol. Chem.* **121**, 417-424.
- Sund, H., Weber, K. & Molbert, E. (1967). *Eur. J. Biochem.* **1**, 400-410.
- Takeshita, K., Imamoto, Y., Kataoka, M., Tokunaga, F. & Terazima, M. (2002). *Biochemistry* **41**, 3037-3048.
- Tanford, C. & Lovrien, R. (1962). *J. Am. Chem. Soc.* **84**, 1892-1896.
- Teng, T. y. & Moffat, K. (2000). *J Synchrotron Radiat* **7**, 313-317.
- Teng, T. Y., Srajer, V. & Moffat, K. (1994). *Nat Struct Biol* **1**, 701-705.
- Topp, M., Rentzepis, P. & Jones, R. (1971). *Journal of Applied Physics* **42**, 3415-3419.
- Torii, K., Iizuka, T. & Ogura, Y. (1970). *J. Biochem.* **68**, 837-841.
- Tripathi, S., Srajer, V., **Purwar, N.**, Henning, R. & Schmidt, M. (2012). *Biophysical journal* **102**, 325-332.
- Ujj, L., Devanathan, S., Meyer, T. E., Cusanovich, M. A., Tollin, G. & Atkinson, G. H. (1998). *Biophysical journal* **75**, 406-412.
- Unno, M., Kumauchi, M., Hamada, N., Tokunaga, F. & Yamauchi, S. (2004). *Journal of Biological Chemistry* **279**, 23855-23858.
- Unno, M., Kumauchi, M., Sasaki, J., Tokunaga, F. & Yamauchi, S. (2002). *Biochemistry* **41**, 5668-5674.
- Unwin, P. N. & Henderson, R. (1975). *J Mol Biol* **94**, 425-440.
- van Amerongen, H. & van Grondelle, R. (1995). *Methods Enzymol* **246**, 201-226.
- Van Beeumen, J. J., Devreese, B. V., Vanbun, S. M., Hoff, W. D., Hellingwerf, K. J., Meyer, T. E., Mccree, D. E. & Cusanovich, M. A. (1993). *Protein Sci* **2**, 1114-1125.
- Van Brederode, M. E., Hoff, W. D., Van Stokkum, I. H., Groot, M. L. & Hellingwerf, K. J. (1996). *Biophysical journal* **71**, 365-380.
- van Stokkum, I. H., Larsen, D. S. & van Grondelle, R. (2004). *Biochimica et biophysica acta* **1657**, 82-104.
- van Wilderen, L. J., van der Horst, M. A., van Stokkum, I. H., Hellingwerf, K. J., van Grondelle, R. & Groot, M. L. (2006). *Proceedings of the National Academy of Sciences of the United States of America* **103**, 15050-15055.
- Von Laue, M., Friedrich, W. & Knipping, P. (1913). *Ann. Physik* **41**, 971.
- Warshel, A. & Barboy, N. (1982). *Journal of the American Chemical Society* **104**, 1469-1476.
- Wikstrom, M. K. (1977). *Nature* **266**, 271-273.
- Wimberly, B. T., Brodersen, D. E., Clemons, W. M., Morgan-Warren, R. J., Carter, A. P., Vonrhein, C., Hartsch, T. & Ramakrishnan, V. (2000). *Nature* **407**, 327-339.
- Wuthrich, K. (1990). *The Journal of biological chemistry* **265**, 22059-22062.
- Xie, A., Hoff, W. D., Kroon, A. R. & Hellingwerf, K. J. (1996). *Biochemistry* **35**, 14671-14678.
- Yeremenko, S., van Stokkum, I. H. M., Moffat, K. & Hellingwerf, K. J. (2006). *Biophysical journal* **90**, 4224-4235.

2 Material and methods

Monochromatic X-ray crystallography is the major technique to determine the three dimensional structures of bio-molecules. To further understand the function of these molecules, time-resolved Laue crystallography is employed. As a comparison, kinetic analyses are performed with time-resolved absorption spectroscopy on solution as well as with crystals. These techniques are described in detail in the following sections.

2.1 *Monochromatic X-ray crystallography*

2.1.1 Scattering from an atom

To investigate the molecule on the atomic length scale, the wavelength of the employed radiation should be comparable to the size of the atoms or to the length of a chemical bond. Therefore, X-ray radiation with wavelengths in the range of $1 \sim 2 \text{ \AA}$ is an excellent choice. When X-rays are incident on an atom, they are scattered by electrons. The scattering power of an atom is given by the atomic form factor (f). f is proportional to the number of electrons in an atom. Therefore, scattering from a heavy atom such as iron is much stronger than the scattering from a carbon, oxygen or a nitrogen atom. The atomic form factor also depends on the scattering angle (2θ) and decreases significantly at higher values of 2θ (Fig. 2.1A).

2.1.2 Scattering from a molecule

All atoms in a molecule scatter according to their atomic form factors. The superposition of all the scattered waves results in the structure factor of a molecule which is given by

$$F^M(\vec{H}) = \sum_{j=1}^N f_j e^{2\pi i \vec{H} \cdot \vec{R}_j} \quad (2.1)$$

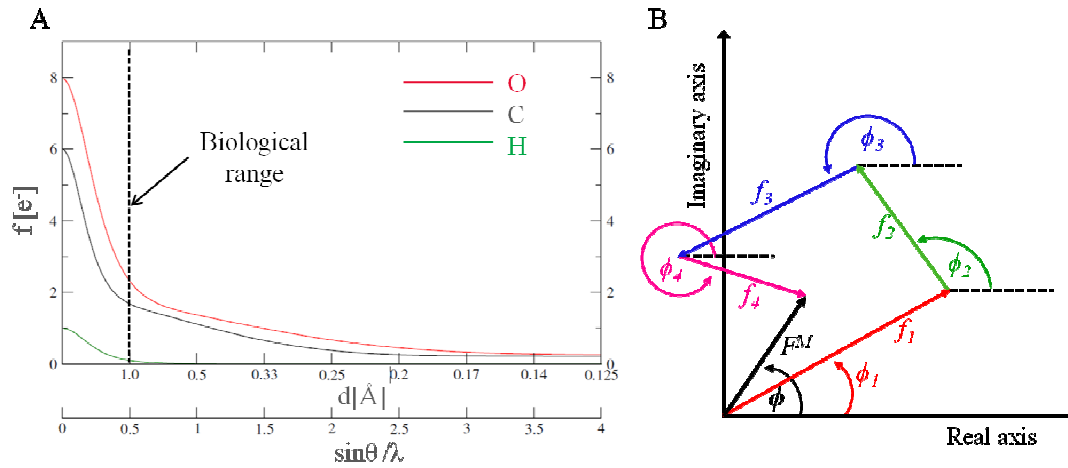


Figure 2.1 **A.** Atomic form factors of oxygen, carbon and hydrogen atoms plotted as a function of $\sin \theta / \lambda$. Dependence of atomic form factors on the resolution d (\AA) is also displayed. 2θ is the scattering angle and λ is wavelength of the incoming X-rays. The atomic form factors for each of these atoms are normalized by their corresponding atomic number at zero scattering angle ($2\theta = 0$). **B.** Atomic form factors of four different atoms f_1 (red), f_2 (green), f_3 (blue) and f_4 (magenta) with their corresponding phases ϕ_1, ϕ_2, ϕ_3 and ϕ_4 are plotted in an Argand diagram. The resultant structure factor amplitude F^M with the phase ϕ is shown in black.

where \mathbf{s} is the scattering vector, N is the total number of atoms in a molecule, f_j is the atomic form factor of the j^{th} atom, \mathbf{r}_j is the position vector of the j^{th} atom. An example for a molecule having 4 atoms with their atomic form factors and corresponding phases is drawn in an Argand diagram (Fig. 2.1B). The resultant structure factor of this molecule is

2.1.3 Scattering from a crystal

Due to the weak interaction of X-rays with matter, the intensity scattered from a molecule is very weak. An ensemble of molecules is required to intensify scattering. In a single crystal, molecules are arranged in a periodic lattice. The structure factor of a crystal is the superposition of the scattered waves from all atoms in the crystal which can be written as

where M is the total number of atoms in the crystal, f_m is the atomic form factor of the m^{th} atom and \vec{r}_m is the position vector of the m^{th} atom (Fig. 2.2A). If a crystal has N unit cells with each of them containing J atoms, the total structure factor of the crystal can be separated in two terms which can be written as

where \vec{R}_n is the lattice vector and \vec{r}_j is the position vector of j^{th} atom in the unit cell (Fig. 2.2A). The first term is known as the lattice factor G and the second term represents the structure factor of a molecule.

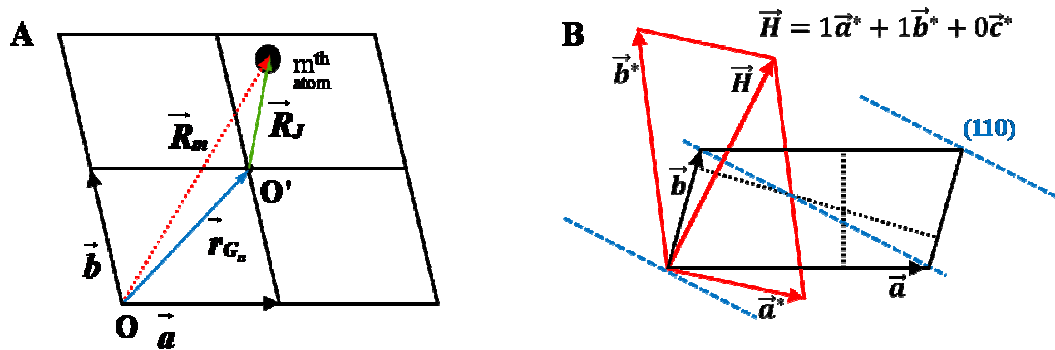


Figure 2.2 A. An example of four unit cells with the translational vectors \vec{a} , \vec{b} , and \vec{c} (not shown, lies parallel to \vec{x}) in real space. \vec{r}_m (in red) denotes the position vector of the m^{th} atom with respect to a common origin O . \vec{R}_n can be represented as a sum of lattice vector \vec{a} (in blue) and the position vector \vec{r}_j (in green) with respect to the origin O' . **B.** The representation of a real space and the associated reciprocal space. \vec{a} , \vec{b} , and \vec{c} denote real space vectors (in black) and \vec{a}^* , \vec{b}^* , and \vec{c}^* denote corresponding reciprocal lattice vectors (in red). Three parallel lattice planes of miller index (110) are shown in blue (dashed line). Scattering vector \vec{H} is represented as linear combination of reciprocal space vectors with integer multiple $h = 1$, $k = 1$ and $l = 0$.

2.1.4 The lattice factor for a crystal having an infinite number of unit cells

If a crystal has U, V and W unit cells in the direction of translation vectors \vec{a} , \vec{b} , and \vec{c} , respectively then the lattice factor G (Eq. 2.3) is expressed as a triple sum

$$G = \sum_{u=0}^U e^{2\pi i u \vec{H} \cdot \vec{a}} \cdot \sum_{v=0}^V e^{2\pi i v \vec{H} \cdot \vec{b}} \cdot \sum_{w=0}^W e^{2\pi i w \vec{H} \cdot \vec{c}} \quad (2.4)$$

where u, v and w are the integer numbers. For an infinitely large crystal, this triple sum is zero unless the scalar products of the scattering vector and the lattice vectors are integer numbers.

$$\begin{aligned} \vec{H} \cdot \vec{a} &= h \\ \vec{H} \cdot \vec{b} &= k \\ \vec{H} \cdot \vec{c} &= l \end{aligned} \quad (2.5)$$

Here h, k and l are integer numbers and these relations are known as the Laue conditions. This shows that a crystal scatters X-rays only in those directions for which the Laue conditions are satisfied. The lattice factor G is then given by

$$G = U \cdot V \cdot W = N \quad (2.6)$$

where N is the total number of unit cells. The structure factor amplitude of the crystal is amplified by N due to the lattice factor contribution.

2.1.5 Deviation of the lattice factor due to a finite size crystal

Crystal dimensions are not infinite. Their finite sizes cause certain deviations from the Laue conditions. The intensity amplification due to the lattice factor G is given by

$$G^2 = \frac{\sin^2 U \pi \vec{H} \cdot \vec{a}}{\sin^2 \pi \vec{H} \cdot \vec{a}} \cdot \frac{\sin^2 V \pi \vec{H} \cdot \vec{b}}{\sin^2 \pi \vec{H} \cdot \vec{b}} \cdot \frac{\sin^2 W \pi \vec{H} \cdot \vec{c}}{\sin^2 \pi \vec{H} \cdot \vec{c}} \quad (2.7)$$

The total area calculated under each of these functions shows that the scattered intensity is amplified by N rather than N^2 .

2.1.6 Scattering vector \vec{H}

A crystal consists of lattice lines and lattice planes. When X-rays hit these lattice planes, they are scattered such that the incident and the scattered beam make an equal angle to the planes. The direction of the scattering vector \vec{H} is perpendicular to these reflecting planes. To represent the scattering vector \vec{H} , a coordinate system in reciprocal space is constructed, in which the Laue conditions are automatically fulfilled (Fig. 2.2B). The reciprocal lattice vectors are calculated using the real space basis vectors as follows

$$\vec{a}^* = \frac{\vec{b} \times \vec{c}}{\vec{a} \cdot \vec{b} \times \vec{c}}; \quad \vec{b}^* = \frac{\vec{c} \times \vec{a}}{\vec{a} \cdot \vec{b} \times \vec{c}}; \quad \vec{c}^* = \frac{\vec{a} \times \vec{b}}{\vec{a} \cdot \vec{b} \times \vec{c}}; \quad (2.8)$$

where \vec{a}^* , \vec{b}^* and \vec{c}^* are reciprocal lattice vectors and \vec{a} , \vec{b} and \vec{c} are real space vectors.

The scattering vector \vec{H} can be represented as a linear combination of the reciprocal lattice vectors which is given by

$$\vec{H} = h\vec{a}^* + k\vec{b}^* + l\vec{c}^* \quad (2.9)$$

where h , k and l are the integer numbers. For a lattice plane of Miller index (h, k, l) , the length of scattering vector \vec{H} is given by the following equation

$$|\vec{H}| = \sqrt{(h\vec{a}^*)^2 + (k\vec{b}^*)^2 + (l\vec{c}^*)^2} = \frac{1}{d_{hkl}} \quad (2.10)$$

where d_{hkl} is the interplanar distance of a plane (h, k, l) . All the higher order planes (nh, nk, nl) share a common miller index (h, k, l) . For these set of planes, the direction of scattering vector \vec{H} is the same, however the length is different which is given by

where n is the integer multiple and \vec{H} is defined above. As a consequence, the scattering vector is a crystal property.

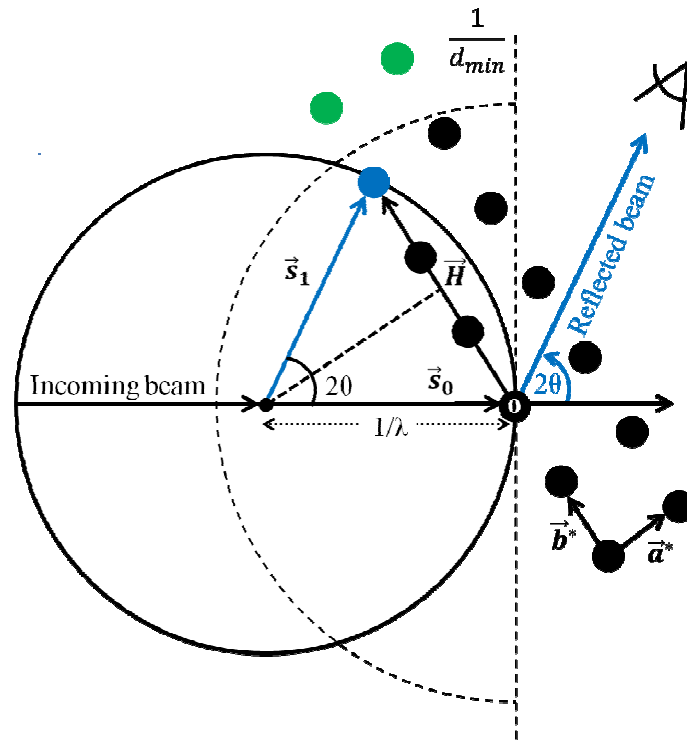


Figure 2.3 Representation of the diffraction geometry in reciprocal space for the conventional rotation method. An Ewald sphere of radius $1/\lambda$ (\AA^{-1}) is drawn where λ is the wavelength of monochromatic X-rays. The origin of the reciprocal lattice is at point O . Black dots, arranged in a periodic manner denotes the reciprocal lattice points (RLPs). The directions of incoming and scattered beam are represented by \vec{s}_0 and \vec{s}_1 , respectively. The lengths of vector \vec{s}_0 and \vec{s}_1 are the same due to the elastic scattering condition. 2θ represents the scattering angle and \vec{H} is the scattering vector. RLP in blue intersects with the Ewald sphere and satisfies the diffraction condition. A sphere of radius $1/d_{min}$ denotes the experimental resolution limit. RLPs (in green) do not diffract because they lie outside this sphere of radii $1/d_{min}$.

2.1.7 The Bragg conditions

Bragg conditions arise from the combination of Laue conditions and elastic scattering conditions. Due to the elastic scattering of X-rays, the wavelength of incoming ray λ and

that of scattered ray \vec{S}_1 are same as shown in the Fig. 2.3. The relationship between scattering angle and scattering vector is given by

$$\sin \theta = \frac{|\vec{H}|/2}{1/\lambda} \quad (2.12)$$

Using Eq. (2.11) and (2.12), the well-known Bragg condition is derived:

$$2d_{hkl} \sin \theta = n\lambda \quad (2.13)$$

2.1.8 Physical and experimental resolution limit

All the reciprocal lattice points (RLPs) for which the Bragg condition is satisfied contribute to a diffraction pattern. However, the RLPs for which the scattering vectors \vec{H} are larger than the diameter of the Ewald sphere ($2/\lambda$) never penetrate the Ewald sphere. These lattice points lie outside the physical resolution limit d which is given by

$$d = \frac{\lambda}{2} \quad (2.14)$$

where $1/\lambda$ is the radius of the sphere centered at the origin O. Protein crystals do not diffract to physical resolution limit due to certain experimental limitations. This enforces an experimental resolution limit which is given by d_{\min} (Fig. 2.3). Consequently, only RLPs lying inside the resolution sphere of $1/d_{\min}$ can contribute to the diffracted intensity.

2.1.9 Structural heterogeneity and dynamic disorder

There are two types of disorders found in the protein crystals: static and dynamic. In static disorder, no motion is observed on the time scale of the experiment. In an ideal crystal, unit cells are repeated in a regular manner in three dimensions. All the molecules in each unit cell have the same positions as well as the same orientations. However, in a real crystal, molecules or parts of the molecules do not occupy the same position and also

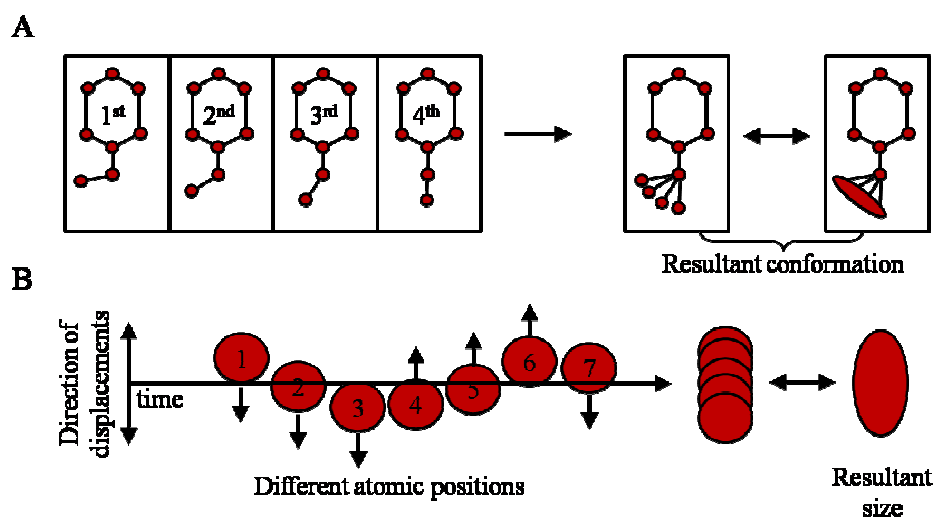


Figure 2.4 A. Several factors contribute to the static disorder and one of them is demonstrated. Four different orientations of a molecule in four unit cells are shown. The resultant conformation (red ellipsoid) is extended spatially. B. A factor causing dynamic disorder is shown. A molecule is vibrating about an equilibrium position (red spheres). An average over seven atomic positions (partially overlapped spheres) is equivalent to an enlarged electron density of the molecule (red ellipsoid). Modified version of the figure from <http://www.christian.naether.uni-kiel.de/pdf>.

may not have exactly the same orientation. This is one of the factors which contribute to the static disorder. In addition, proteins are large molecules and their structures are quite flexible. This causes structural heterogeneity in which atoms are slightly shifted in each unit cell. The conformation of a molecule can be different from one unit cell to the other (Fig. 2.4A). The disorders described above are of static type. In the case of dynamic disorder, motions are much faster than the time scale of the experiment. Atoms in the crystal vibrate about their equilibrium position and therefore, at any instance of time do not occupy identical positions in the different unit cells. As a consequence, an average over all the atomic positions is obtained which is equivalent to an enlarged electron density at a fixed atomic position (Fig. 2.4B). Additionally, molecules might fluctuate between different conformations. These factors give rise to dynamic disorder in a crystal.

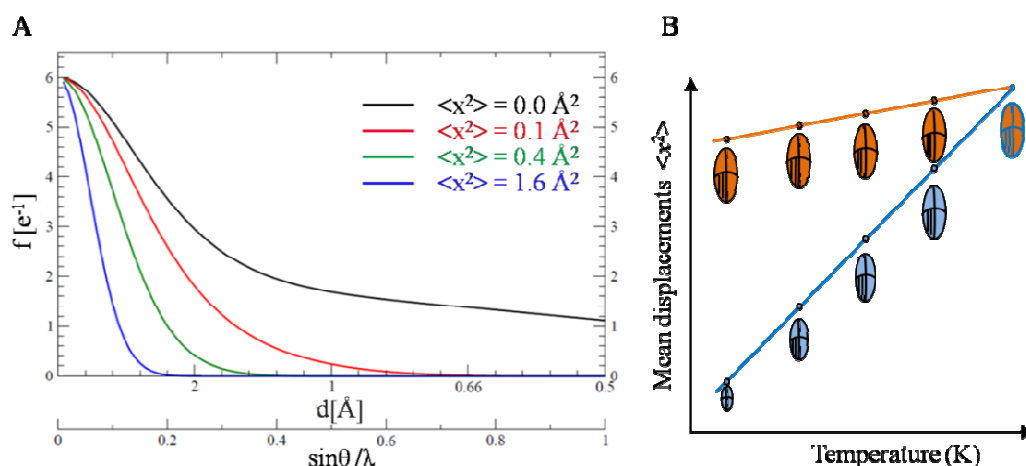


Figure 2.5 **A.** The atomic form factor of a carbon atom, normalized to its atomic number plotted against resolution d and $\sin\theta/\lambda$. The effect of an increase in the mean displacement $\langle x^2 \rangle$ on the atomic form factor is also shown. **B.** An oversimplified conceptual schematic showing the effect of lowering the temperature on static and dynamic disorders. At ambient temperature, overlapping red and blue ellipsoids indicate that static disorder (red ellipsoid) and dynamic disorder (blue ellipsoid) cannot be distinguished. When temperature is decreased, static disorders are unaffected whereas dynamic disorders start to decrease. Modified version of the figure from <http://www.christian.naether.uni-kiel.de/pdf>.

Each of these different types of disorder, static and dynamic, contribute to the Debye Waller Factor (DWF)

where $\langle x^2 \rangle$ is the mean square displacement, θ is half of the scattering angle, λ is the wavelength of the monochromatic radiation and B is the B-factor. The value of DWF is less than one except in the forward direction ($\theta=0$, Eq. 2.15). This diminishes the scattering intensity for any scattering angle larger than zero. Higher angles are significantly more affected as compared to lower angles (Fig. 2.5A). Since the DWF is parameterized by the mean square distribution of the atomic positions, it does distinguish between static and dynamic disorder. The types of disorders may be differentiated if

diffraction data are collected at different temperatures. At lower temperatures dynamic motion seems to reduce significantly whereas static disorders should be unaffected (Fig. 2.5B). X-ray crystallographic experiments are performed at cryogenic temperatures. This substantially diminishes the effects of dynamic disorders on the diffraction data.

2.1.10 The mosaicity

Perfect crystals generate sharp reciprocal lattice points whose intersection with the Ewald sphere give rise to intense Bragg peaks. Real crystals are not perfect and contain various defects. Due to these imperfections, it can be considered that a crystal is composed of

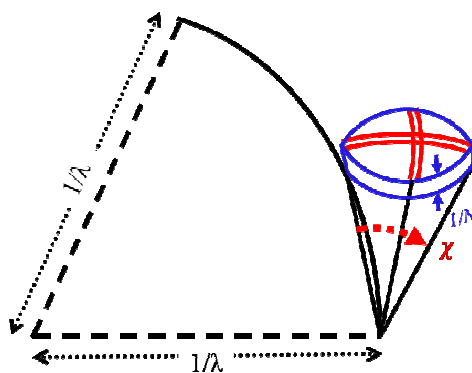


Figure 2.6 Effect of the mosaicity χ on the reciprocal lattice points. An Ewald sphere of radius $1/\lambda$ is drawn. $1/N$ represents the natural line width (in blue) of a reflection where N is the total number of unit cells in the crystal. The broadening of the reciprocal lattice points due to mosaicity are shown in red double lines.

small mosaic blocks, whose orientations are slightly different from each other. As a consequence, a given Bragg reflection is observed through an angular range which is known as the mosaicity (χ). χ determines the width of the so called rocking curve (Fig. 2.6). The rocking curve also broadens with the increase in the divergence and the bandwidth of the employed X-ray radiation. If a crystal is rotated with a rotation step $\Delta\theta$ smaller than the mosaicity, the reflections are only partially recorded in one diffraction

pattern. The remaining parts of the reflections are recorded in subsequent images. For a highly mosaic crystal, reflections start to overlap. This may affect the quality of the obtained intensities.

2.1.11 Lorentz factor

When a crystal rotates, the associated reciprocal lattice and their lattice points rotate through an Ewald sphere. A reflection remains in the diffracting position for a certain period of time given by

$$\frac{\lambda}{\omega \sin 2\theta} \quad (2.16)$$

where λ is wavelength of the incoming X-ray beam, ω is the angular velocity of rotation and 2θ is the scattering angle. In addition, the scattered intensity depends on the intersection of the reciprocal diffraction volume with the Ewald sphere. The ratio of this intersected area and the total surface area of an Ewald sphere is dependent on $1/\lambda^2$. After combining both aforementioned effects, the Lorentz factor contributes a λ^3 dependence to the scattered intensity.

2.1.12 Polarization factor

When an electron interacts with electromagnetic radiation such as X-rays, the electron accelerates and radiate like an oscillating dipole. Since no scattering is observed in the direction of the electron propagation, the scattered intensity must be corrected. This correction factor is known as the polarization factor. For the unpolarized beam, the scattered intensity is reduced by the factor $\frac{1+\cos^2 2\theta}{2}$. On the contrary, synchrotron beam is strongly polarized in the horizontal direction. If this polarized beam is used to perform an experiment, a crystal is rotated such that its rotation axis is aligned along the polarization

direction of the beam. This maximizes the scattering intensity perpendicular to the axis of rotation.

2.1.13 Total integral intensity scattered by a crystal

After incorporating all the factors described previously, the scattering intensity from a crystal is given by

$$I_{int}(hkl) = \frac{\lambda^3}{\omega} \cdot N \cdot \sigma_e \cdot I_0 \cdot \frac{1 + \cos^2 2\theta}{2 \sin 2\theta} \cdot |\mathbf{F}^M(hkl)|^2 \quad (2.17)$$

where I_{int} is the integral reflection intensity, λ is wavelength of incoming X-rays, N is the total number of unit cells, σ_e is the Thomson scattering cross section of an electron, I_0 is the intensity of the incident X-rays, 2θ is scattering angle, $|\mathbf{F}^M|$ is the structure factor amplitude of a molecule at the position h , k and l . Due to the λ^3 dependence (Eq. 2.17), the radiation with a longer wavelength such as X-ray from Cu-K $_{\alpha}$ (1.54 Å) is an excellent choice for in-house protein crystallography, where I_0 is comparatively small.

2.1.14 Sample preparation and mounting

A crystal is picked up by a cryo-loop from the hanging drop (Fig. 2.7A) or sitting drop (Fig. 2.7B) of a crystallization tray. The crystal is then soaked in a cryoprotectant, a buffer that typically contains sugar, polyethylene glycol and glycerol, for 15 ~ 25 s to reduce ice formation upon its freezing. In some cases, crystals are very sensitive. Such crystals are first soaked in a stabilization buffer for ~20 s and then in the cryoprotectant to reduce the osmotic shock. Crystals treated with cryoprotectant are mounted in a loop and shock frozen at 100K using a cryostream. If the goal is to bind a small molecule to the crystal, the crystal is soaked in a solution containing that molecule before applying the cryoprotectant. After that, it is looped and frozen as described above.

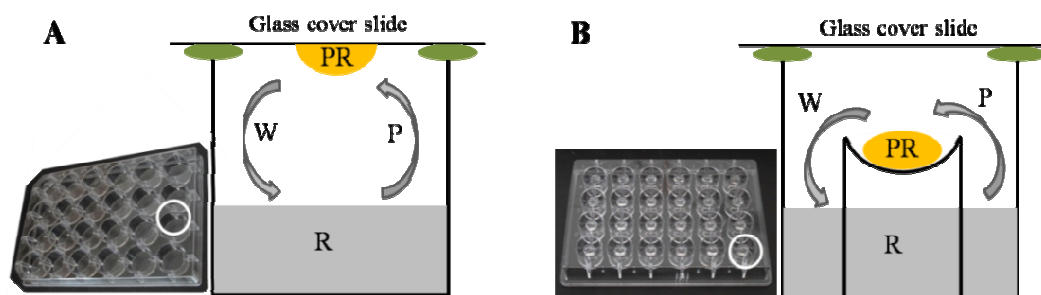


Figure 2.7 Schemes for different methods to crystallize proteins. Circle in white shows a single well of the 24-well plate. PR: protein solution, R: reservoir solution, W: water diffusing from protein solution to reservoir solution P: precipitant diffusing from reservoir to protein solution. High vacuum grease (green ellipses) is used to seal the cover slide. **A.** A wall plate (in grey) is used for the hanging drop method. The protein droplet (colored yellow) is placed upside down on the glass cover slide to allow equilibration between the protein and the reservoir solution. **B.** A wall plate used for the sitting drop method is shown in grey. The protein solution (yellow colored) is placed within a dip in the upward direction.

2.1.15 Experimental setup

All the monochromatic crystallographic experiments described in this thesis are performed at beamline BioCARS 14-BM-C at the advanced photon source (APS). A typical experimental set up of the beamline is described in the following. X-rays are generated by inserting bending magnets in the path of a high energy electron beam. A Germanium (111) single crystal is used as a monochromator (<http://biocars.uchicago.edu/page/14-bm-c-beamline>). X-rays of wavelength 0.9 Å ($E = 13.8$ keV) with $\Delta E/E = 3.1 \times 10^{-4}$ are used. The beam is focused to a typical spot size of $100 \times 300 \mu\text{m}^2$ at the sample position. The flux of X-ray beam in this spot size is $\sim 5 \times 10^{11}$ photons/s. This flux is used to illuminate the crystal during the data acquisition. A charge coupled device (CCD) area detector ADSC Q315 is used to record X-ray photons scattered from a crystal.

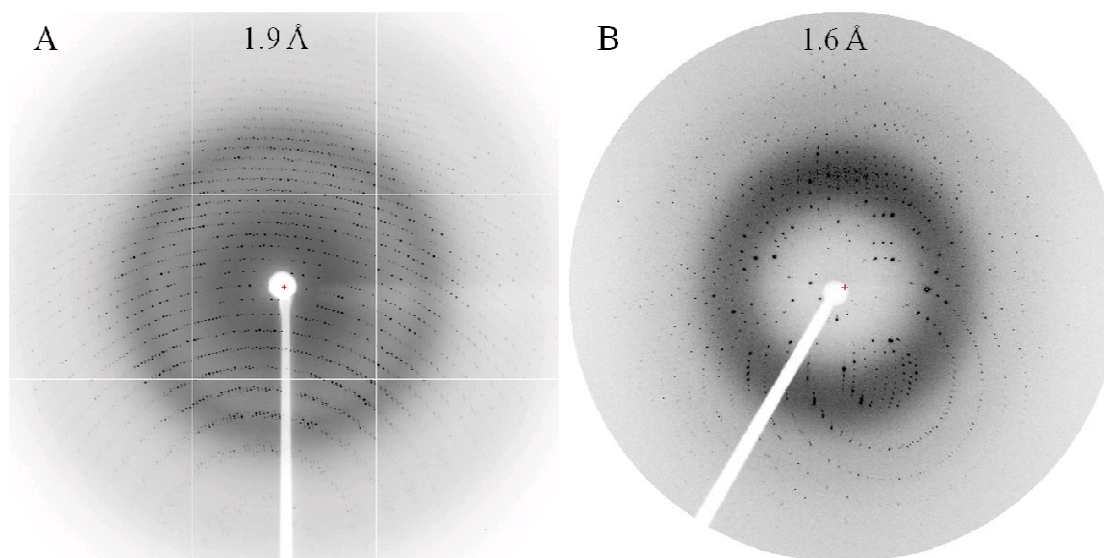


Figure 2.8 **A.** A typical diffraction pattern obtained for catalase using monochromatic x-ray crystallography. **B.** A typical Laue diffraction pattern of photoactive yellow protein using polychromatic X-rays. Resolution limits are shown for the edge of the detectors.

2.1.16 Data collection

The crystal is initially exposed to the X-rays in a random orientation. A typical diffraction pattern obtained for catalase to resolution 1.9\AA is shown in Fig. 2.8A. The crystal is then rotated through a rotation range \square (Fig. 2.9A) in steps of $\Delta\square$. The diffraction patterns obtained after each rotation step are collected. \square usually depends on the symmetry of a crystal. A smaller \square can be selected for a crystal of higher symmetry while a crystal having no symmetry must be rotated through 180° (Fig. 2.9B). $\Delta\square$ is chosen based on the mosaicity of the crystal and its typical value is $0.5^\circ \sim 1^\circ$.

2.1.17 Data analysis and refinement

All the steps associated with the data processing are shown in Fig. 2.10. Programs such as Mosflm (Leslie, 2006) and HKL2000 (Otwinowski & Minor, 1997) are widely used to reduce monochromatic data. However, we used Mosflm, because it provides the best

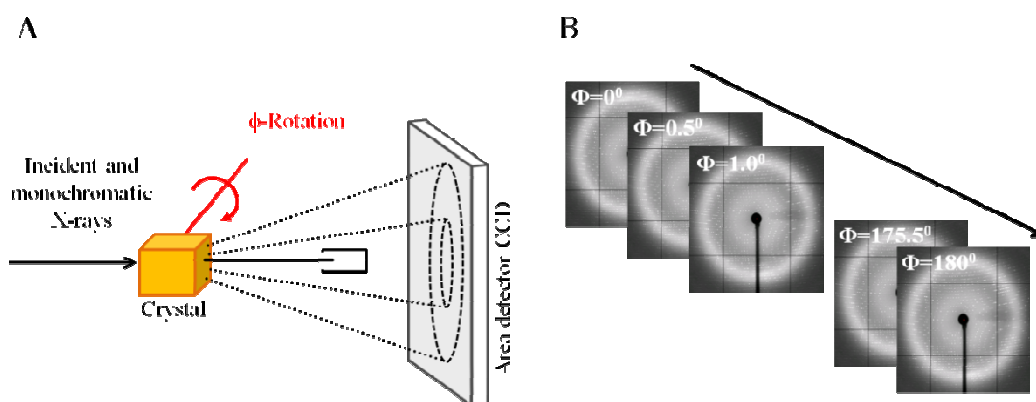


Figure 2.9 Scheme for monochromatic X-ray data collection. **A.** A crystal (yellow colored) is illuminated by X-rays and rotated about the \square -axis (in red) during data collection. The area detector CCD is shown in grey. **B.** The diffraction patterns are shown from $\square = 0^\circ$ to 180° with $\Delta\square = 0.5^\circ$.

statistics for protein crystals with large unit cells and with overlapping reflections. The quality of data statistics obtained from Mosflm is shown in Tab. 3.1. Three main steps are involved in data reduction with Mosflm: Indexing, Refinement and Integration. In indexing, crystal parameters such as unit cell dimensions and the initial crystal orientations are determined. In the next step, these two crystal parameters as well as the mosaicity are refined. Detector parameters (detector position and detector orientation) and beam parameters (beam orientation and beam divergence) are also refined. For each reflection, two masks are defined such that one mask covers the Bragg peak and another one covers the background. Background-subtracted reflection intensities are determined by integrating the photon counts found in the individual pixels. Intensities are less accurate for weak and overlapping reflections. Profile fitting is used to determine the intensity of such reflections. Sample profiles are first derived from well separated and non-overlapping reflections and then fitted to the reflections with lower intensities.

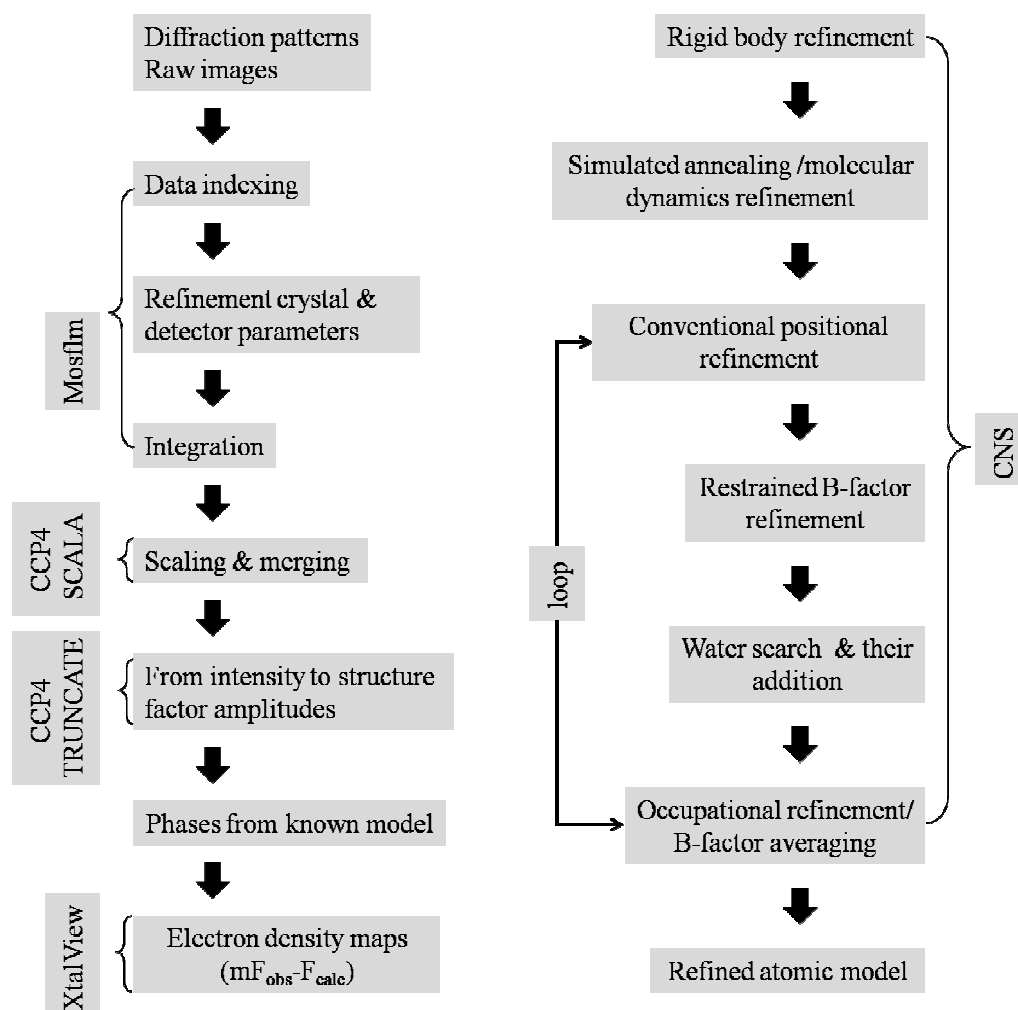


Figure 2.10 Scheme for monochromatic X-ray data analysis. Column on the left shows the steps to obtain structure factor amplitudes from the diffraction patterns. Column on the right denotes the refinement protocols to improve the quality of an atomic model, if phases are obtained from a known model. After each refinement step, obtained electron density maps are inspected with Xtalview.

The volume calculated under two dimensional fitted profile yields the integrated intensity on an arbitrary scale. A common scale factor is required to bring all the reflection intensities on the same level. For that, intensities are assumed on the same scale for an individual diffraction pattern as well as for few subsequent ones. The intensities of the partials from the subsequent images are summed up with the CCP4 program SCALA

(CCP4, 1994, Evans, 2006). The summed intensities from the partials and those from the full reflections are used to determine the scale factor for each individual diffraction pattern. By applying these scale factors, the reflection intensities from all the diffraction patterns are brought to the same scale. Symmetrically equivalent reflections as well as reflections with multiple measurements are merged and averaged to obtain unique reflections. From a list of unique reflections intensities, structure factor amplitudes and their standard deviations are calculated using the CCP4 program TRUNCATE (CCP4, 1994)(Fig. 2.10). The quality of reduced data is determined by examining the R_{merge} , I/σ_I and completeness. The R_{merge} denotes the agreement between multiple observations of a given reflection.

$$R_{merge} = \frac{\sum_{hkl} \sum_{j=1}^N |I_{hkl}(j) - \bar{I}_{hkl}|}{\sum_{hkl} \sum_{j=1}^N I_{hkl}(j)} \quad (2.18)$$

where N is a number of multiple observations for the reflection (h, k, l) and \bar{I}_{hkl} is the average intensity of this reflection. For large unit cells, overall R_{merge} values smaller than 0.08 ~ 0.1 are acceptable. I/σ_I denotes the ratio of intensity to their standard deviation which is equivalent to the signal to noise ratio. This value should be larger than two in the highest resolution shell. Completeness is a measurement of the coverage of the reciprocal space in a full data set and should be more than 75 ~ 80 %.

2.1.18 Molecular replacement and crystallographic refinement

Once structure factor amplitudes are determined, phases are required to calculate the electron density ρ . At coordinates X, Y and Z in the unit cell, ρ can be represented as

$$\rho(XYZ) = \frac{1}{V} \sum_h \sum_k \sum_l |F(hkl)| e^{i\alpha_{hkl}} \cdot e^{-2\pi i(hX+kY+lZ)} \quad (2.19)$$

where V is the volume of the unit cell, $|F(hkl)|$ and α_{hkl} are structure factor amplitude and phase of the reflection (h, k, l) , respectively. Phases can be determined using three major approaches: multiple isomorphous replacement (MIR), multiple anomalous dispersion (MAD) and molecular replacement (MR). If a protein structure that has a sequence similar to the protein under investigation is available, then molecular replacement can be used. Otherwise, one has to follow the complicated process of ab-initio phase determination with MIR or MAD. The molecular replacement method involves two important steps. The first step is rotation in which the orientation of a known atomic model is found in the crystal. The next one is translation in which the positions of correctly orientated search model are found in the unit cell. If the known structure has been determined for the same crystal form as the protein to be investigated, then rotation and translation steps are not required anymore. The known atomic model can directly be used as a starting model. However, refinements are necessary to increase the agreement between the calculated and the observed structure factor amplitudes (Fig. 2.10). Before any of the refinement steps are performed, all the water molecules and unwanted cofactors are removed from the initial atomic model. In our case, the program Crystallographic & NMR systems (CNS) (Bruenger *et al.*, 1988) is used for the model refinement. As a first step, the orientation of a protein molecule within the unit cell is refined by a rigid body refinement at low resolution such as 3Å (Fig. 2.10). All the subunits of a protein molecule are treated as rigid domains. To correct the large structural errors in the atomic model simulated annealing refinement also known as molecular dynamics refinement is performed. The temperature of a molecule is first raised sufficiently high and then the molecule is allowed to cool down slowly. Typically, a

2000K protocol to full resolution is applied for large protein molecules. After that, conventional positional refinement is performed to optimize the atomic positions. The residual between calculated (F_{hkl}^{calc}) and observed (F_{hkl}^{obs}) structure factor amplitudes is minimized in a least square method (Eq. 2.20).

$$\underbrace{\sum_{hkl} w(|F_{hkl}^{obs}| - |F_{hkl}^{calc}(X, Y, Z, B)|)^2}_{\substack{\text{X-ray term} \\ (Q_{xray})}} + \underbrace{\sum_{i=1}^{restraints} (r_i^{obs} - r_i^{calc})^2}_{\substack{\text{Geometric term} \\ (Q_{geom})}} \rightarrow \text{minimum} \quad (2.20)$$

The first term in this minimization protocol is called X-ray term or X-ray residual (Q_{xray}), in which atomic coordinates X, Y, Z and B-factors are free parameters. w is the weighting factor for this term. In order to increase the ratio of observables to free parameters, stereochemical parameters such as bond lengths, bond angles, dihedral angles, van der Waals contacts and planar groups are used. If small deviations are allowed for these parameters during the refinement, they are known as restraints. The sum of least square residuals of these restraints from its target values is known as geometrical term or geometrical residual (Eq. 2.20). Both X-ray and geometric terms are minimized simultaneously until convergence is reached. B-factors of all the atoms are determined using restrained B-factor refinement with a 20 ~ 40 step protocol. After the refinement steps, SigmaA-weighted $2mF_{obs} - DF_{calc}$ maps are generated (Rupp, 2010). These Fourier maps are inspected using a molecular viewer program Xfit from XtalView package (McRee, 1999).

2.1.19 Water search and addition

For a complete atomic structure, crystallographically visible water molecules are found and added to the atomic model of the protein. Water molecules up to a certain sigma (σ)

level are searched from a difference electron density map ($F_{\text{obs}} - F_{\text{calc}}$). These water molecules are added to the structure. However, if the binding of a small molecule to a protein is under investigation, one should avoid adding water molecules to the protein active site. After insertion of all the water molecules, atomic positions are refined using conventional refinement. Once generated, electron density map $2F_{\text{obs}} - F_{\text{calc}}$ and difference map $F_{\text{obs}} - F_{\text{calc}}$ are inspected. In the $F_{\text{obs}} - F_{\text{calc}}$ map, positive electron density may indicate the positions of additional water molecules or that of ligands expected to be bound. The negative electron density may denote badly refined regions. If the electron density map reveals misorientations of amino acid residues, they are manually reoriented into the electron density map using Xfit (McRee, 1999). Positional refinement is performed again after these model corrections. Both of these steps are repeated until no obvious misorientations are detected.

2.1.20 Structure validation

Once the atomic model is properly refined, the residual between observed and calculated structure factor amplitudes can be determined. This residual is known as R-factor, which can be written as

$$R = \frac{\sum_{hkl} (|F_{\text{obs}}(hkl)| - |F_{\text{calc}}(hkl)|)}{\sum_{hkl} |F_{\text{obs}}(hkl)|} \quad (2.21)$$

where $|F_{\text{obs}}(hkl)|$ and $|F_{\text{calc}}(hkl)|$ are the observed and calculated structure factor amplitudes, respectively. An atomic model whose R-factor is less than about 0.25 can be considered reliable. A Ramachandran plot can also be used to judge the geometric quality of an atomic model. This plot shows the possible peptide bond angles (ϕ , ψ) of the protein main-chain. Unrealistic values can be identified for an incorrect atomic model. In

addition, Luzzati plots (Drenth, 1999) are used to estimate the coordinate error of the calculated model by plotting the R-factor as a function of resolution.

2.2 Laue and time-resolved X-ray crystallography

2.2.1 Polychromatic X-rays

In the Laue technique, a single crystal is illuminated with polychromatic X-rays to obtain a diffraction pattern (Fig. 2.8B). Due to the broad bandwidth of these X-rays, a wide

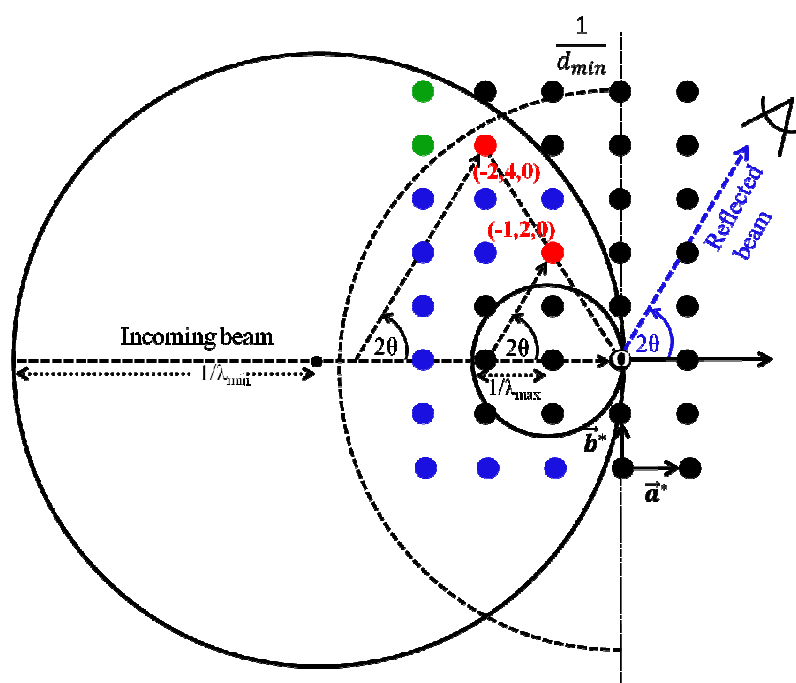


Figure 2.11 A reciprocal space representation of Laue diffraction by a stationary crystal. A reciprocal lattice with the origin at O is shown. Two Ewald spheres of radii $1/\lambda_{\min}$ and $1/\lambda_{\max}$ are drawn where λ_{\min} and λ_{\max} indicate the minimum and the maximum wavelength of the polychromatic X-rays, respectively. Basis vectors of reciprocal lattice are represented as \vec{a}^* and \vec{b}^* . Blue colored reciprocal lattice points (RLPs) lie between both the Ewald spheres and therefore satisfy the diffraction condition. Corresponding reflections are obtained on the detector with scattering angle 2θ . RLPs shown in black are not in the reflecting positions. Red colored RLPs $(-1, 2, 0)$ and $(-2, 4, 0)$ generate harmonically overlapping reflections. RLPs (in green) do not diffract because they lie outside a sphere of radii $1/d_{\min}$ where d_{\min} represents the maximum resolution limit.

range of the reciprocal lattice is covered. The minimum (λ_{\min}) and the maximum (λ_{\max}) wavelength limit of the polychromatic radiation gives rise to two Ewald spheres of radii $1/\lambda_{\min}$ and $1/\lambda_{\max}$ (Fig. 2.11). The diffraction condition is satisfied for all those reciprocal lattice points (RLPs) which lie between both the Ewald spheres.

2.2.2 Instantaneous recording of integral intensity

The use of polychromatic radiation provides an opportunity to collect integrated reflection intensities instantaneously without rotating the crystal. As described in monochromatic technique (Sec. 2.1.11), the λ -dependence of the Lorentz factor comes from the rotation. This term is absent in Laue method. As a consequence, Laue scattering intensity depends only on λ^2 .

2.2.3 Spatially overlapping reflections

A Laue diffraction pattern is typically very crowded with reflections as compared to that obtained from the monochromatic method. Consequently, a large number of spatially overlapping reflections is present. This overlap occurs due to a very small angular separation of the adjacent diffracted X-ray beam. The density of overlapping spots depends on the scattering angle 2θ as well as on the geometrical conditions such as the unit cell parameters (Cruickshank *et al.*, 1991). The spatial overlap can be resolved by using analytical and numerical reflections profiles. These profiles are derived from the well-separated, non-overlapping reflections and then used to separate these spatial overlaps (Ren & Moffat, 1995).

2.2.4 λ -curve for wavelength normalization

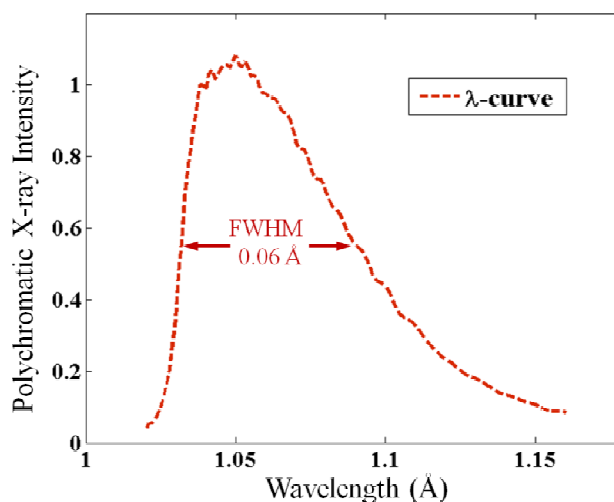


Figure 2.12 A typical λ -curve determined from an experimental data set collected at beamline BioCARS 14-ID-B at Advanced Photon Source (APS). Full width half maximum (FWHM) of the curve is 0.06 Å.

The intensity of the polychromatic radiation varies as a function of wavelength. Therefore, reflections are excited by different frequencies and intensities depending on the orientation of the crystal (Schmidt, 2008, Ren *et al.*, 1999). These reflection intensities must be brought to a common scale. This procedure is known as wavelength normalization that results in a so called λ -curve (Srajer *et al.*, 2000). The λ -curve can be determined directly from the data set of original and unscaled reflection intensities using single order Bragg reflections also known as singlets. This curve corrects for all wavelength-dependent parameters such as the source spectrum, detector response, the overall absorption correction and scattering from a crystal. If the X-ray spectrum of employed X-rays is not stable, the determination of the λ -curve is difficult. A typical λ -curve of full width half maximum (FWHM) of 0.057 Å obtained from a synchrotron X-ray source as shown in Fig. 2.12.

2.2.5 Harmonically overlapping reflections

When Bragg's law is applied, many orders of each Bragg reflections such as (d, λ) , $(d/2, \lambda/2)$, $(d/n, \lambda/n)$ may be stimulated simultaneously. All of them are scattered at the same angle and therefore exactly superimpose on the diffraction pattern (Fig. 2.11). This is called harmonic or energy overlap. For example, reflections $(2\ 4\ 6)$ and $(4\ 8\ 12)$ generate harmonics and share a common index $(1\ 2\ 3)$. The harmonic overlap mainly applies to reflections at low resolution. If these reflections are dismissed from the analysis, the completeness of the low resolution data is reduced. This effect is referred as the 'low resolution hole'. To resolve the harmonic overlap, a particular harmonic and its symmetry mates are measured multiple times at different crystal orientations (Ren & Moffat., 1995). The λ -curve must be already determined as described in the Sec. 2.2.4. As an example, here we show how to resolve a harmonic in which three orders of reflections are superimposed. The observed intensity of a given harmonic I_i^{obs} at different crystal orientations can be written as linear combination of individual intensities

$$\begin{cases} I_1^{obs} = \lambda_{11}I_1 + \lambda_{12}I_2 + \lambda_{13}I_3 \\ I_2^{obs} = \lambda_{21}I_1 + \lambda_{22}I_2 + \lambda_{23}I_3 \\ I_3^{obs} = \lambda_{31}I_1 + \lambda_{32}I_2 + \lambda_{33}I_3 \end{cases} \quad (2.22)$$

where I_i^{obs} is the intensity of a given harmonic at i^{th} orientation, I_i is the individual reflection intensity of i^{th} order reflection and λ_{ii} are the component of λ -curve, which is known. Eq. 2.22 can be rearranged in a matrix representation

$$\mathbf{I}^{obs} = \mathbf{\Lambda} \mathbf{I} \quad (2.23)$$

where \mathbf{I}^{obs} are observed intensities of a particular harmonic, $\mathbf{\Lambda}$ can be determined from the λ -curve. Individual intensities \mathbf{I} can be calculated by matrix inversion.

2.2.6 Scattering background

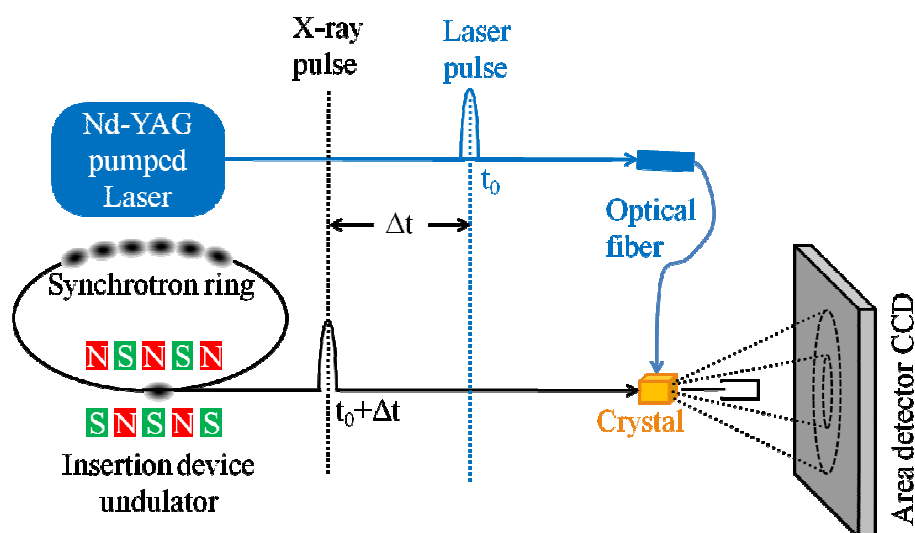


Figure 2.13 A scheme of time-resolved Laue crystallography. A short laser pulse (blue) generated from a pulsed laser is used for reaction initiation in a crystal (yellow) at time t_0 . Pulsed X-rays are generated by the undulator, which consists of a series of magnets as shown in red and green. The X-ray pulses (black) are used to probe the subsequent structural changes at time delays Δt_i after the laser pulse. Laue reflections are recorded on the CCD area detector (grey).

A large fraction of the polychromatic X-rays does not diffract into Bragg reflections. This fraction generates scattering background. This background could be due to various factors such as crystal disorder, scattering by the capillary, scattering by air and Compton scattering. As a consequence, it is difficult to determine very weak reflection intensities that usually appear at high resolution. The background can be significantly reduced by using radiation with smaller bandwidth. A highly intense X-ray beam of a narrow band pass (Graber *et al.*, 2011) can be generated by using an undulator. One has to ensure that the beam is large enough to cover the band width accepted by each reflection. With this undulated radiation, data collection at higher resolution becomes possible and reflection intensities can be measured with higher accuracy (Srajer *et al.*, 2000).

2.2.7 The mosaicity

The Laue method is very sensitive to the crystal mosaicity. If the mosaicity is increased, Laue diffraction spots become elongated. In most cases, the elongation of these spots further increases when a reaction evolves in a protein crystal. Visual inspection of the spots-elongation in the Laue patterns may be a potential method to check whether reaction initiation is successful or not. Higher mosaicity causes additional spatial overlap in an already crowded Laue image. Therefore, crystals with the mosaicity in the range of $0.2 \sim 0.4^\circ$ should be used for time-resolved experiments (Schmidt *et al.*, 2005a, Ihee *et al.*, 2005).

2.2.8 Time-resolved Laue method

The use of the entire bandwidth of X-ray reduces the exposure time by several orders of magnitude as compared to the monochromatic method (Srajer *et al.*, 2000). A Laue image can be collected on the order of 100 picoseconds. Such short exposure times make this technique an excellent choice to investigate the dynamics of bio-molecules (Amorós *et al.*, 1975, Cruickshank *et al.*, 1987). In time-resolved investigations, a reaction is first initiated and then subsequent changes are probed with polychromatic X-rays at different time delays (Δt_i) (Fig. 2.13). The time resolution of these experiments depends on the duration of the laser pulse or the X-ray pulse, whichever is longer. Reaction initiation can be achieved by various methods such as a rapid change in the concentration of substrates, cofactors, protons or electrons or by a rapid change in the temperature or pressure. However, the photo-activation of a chromophore molecule embedded within the protein is the most convenient one and widely used. For example, the photoreceptor PYP can be easily activated on the order of picoseconds and even higher. .

2.2.9 Sample mounting

Time-resolved diffraction experiments are performed at ambient temperature. A protein crystal is mounted in a glass or quartz capillary of 1mm diameter (Fig. 2.14A). A small drop of stabilization buffer is placed at the end of the capillary to keep the crystal moist (Schmidt *et al.*, 2005a). If the crystal is dry, it degrades faster during its repetitive exposure to the consecutive laser pulses. On the other hand, a crystal embedded into too much liquid can easily move from its mounting position after exposure to a laser pulse. The capillary is mounted on the goniostat in a direction perpendicular to both the X-ray pulse and the laser pulse (Fig. 2.14A).

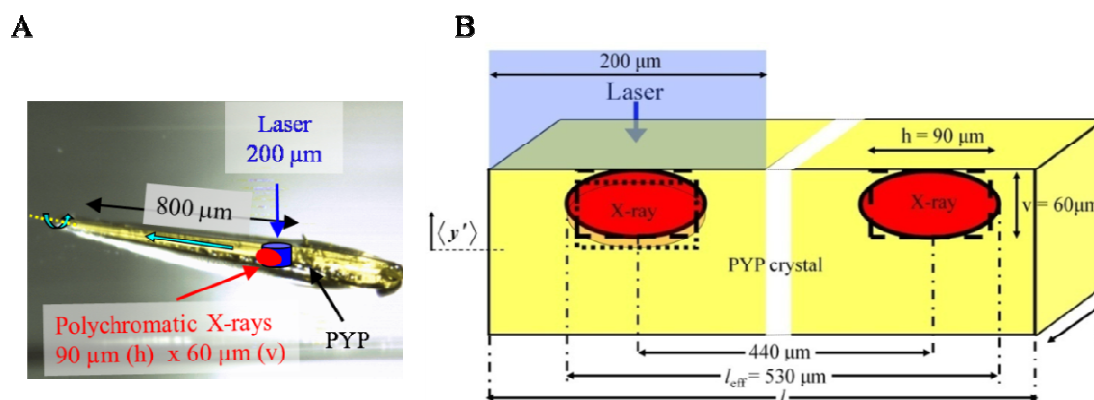


Figure 2.14 A. A pencil-shaped long PYP crystal mounted in a glass capillary for the time-resolved experiments. Black solid line represents the total translation of the crystal during the entire data collection. The rotation axis of the crystal is shown in green. Laser spot size (blue) and X-ray spot size (red) are shown. Figure from Schmidt *et al.*, 2010. **B.** Geometry of PYP crystal settings while illuminated by X-ray and laser pulses. The X-ray beam (red ellipsoids) probes the volume near the surface of the crystal that is illuminated by the laser light. The diameter of the laser beam (blue) is 200 μm , which is substantially larger than the horizontal component of the X-ray beam ($h = 90 \mu\text{m}$). This facilitates the alignment procedure. Arrow on the left denotes positive y' -displacements of the crystal. A part of elliptical region (in orange) shows the new position of X-ray beam after y' -displacement. The crystal translation along the long axis is 440 μm . The length, $l_{\text{eff}} = 530 \mu\text{m}$ is used for the dose calculation. t is the thickness of the crystal. Dashed box: approximation of the beam with a rectangular box, dotted box: new position of the X-ray beam after displacement y' . Figure from Schmidt *et al.*, 2012.

2.2.10 Experimental setup

All time-resolved crystallographic experiments described in this thesis are performed at beamline BioCARS 14-ID-B at the Advanced Photon Source (APS). A typical experimental setup is described in the following. A pulse from an Nd:YAG pumped laser (Opolette HE II) is used to initiate the reaction in the crystal. The full width half maximum (FWHM) of the pulse is about 4ns. It is transported through a tapered fiber and focused to $\sim 200\text{ }\mu\text{m}$ spot at the sample position. The measured energy density of the laser pulse at the sample is 4 mJ/mm^2 . After reaction initiation, subsequent structural changes that may range from nanosecond to second are probed by polychromatic X-rays. Short and intense X-ray pulses of 100 ps are generated from an undulator. The average wavelength (λ_{ave}) of the X-ray radiation is $1.05\text{ }\text{\AA}$ (Fig. 2.11) which corresponds to an average energy (E_{avg}) of 11.8 keV. The bandwidth $\Delta E_{\text{avg}}/E_{\text{avg}}$ is 10%. Each X-ray pulse contains 3.5×10^{10} photons (Graber *et al.*, 2011). The X-ray pulse is focused at the sample position to a typical spot size of $90\mu\text{m}$ (h) X $60\text{ }\mu\text{m}$ (v), where h and v denote the full width half maximum (FWHM) of the pulse in the horizontal and vertical direction, respectively (Fig. 2.14A). The Laser pulse and the X-ray pulse are orientated perpendicular to each other as well as to the capillary in which the crystal has been mounted (Sec. 2.2.9). In most cases, protein crystals are exquisitely optically thick and therefore, the laser pulse penetration into the crystal is shallow (Fig. 2.14B). This results a reaction initiation primarily close to the illuminated crystal surface. The crystal is positioned in the X-ray beam such that only this surface layer is probed by X-rays (Schmidt *et al.*, 2012). To determine the precise position of this surface layer, the crystal is translated in the vertical direction across the X-ray beam and several diffraction

patterns are collected. Once the X-ray beam crosses the edge of the crystal, diffraction pattern starts to fade. By analyzing these patterns, the edge can be determined. With this, the overlap of X-ray beam with the laser illuminated volume can be maximized (Fig. 2.14B). This procedure is known as edge scan (Schmidt *et al.*, 2012, Graber *et al.*, 2011).

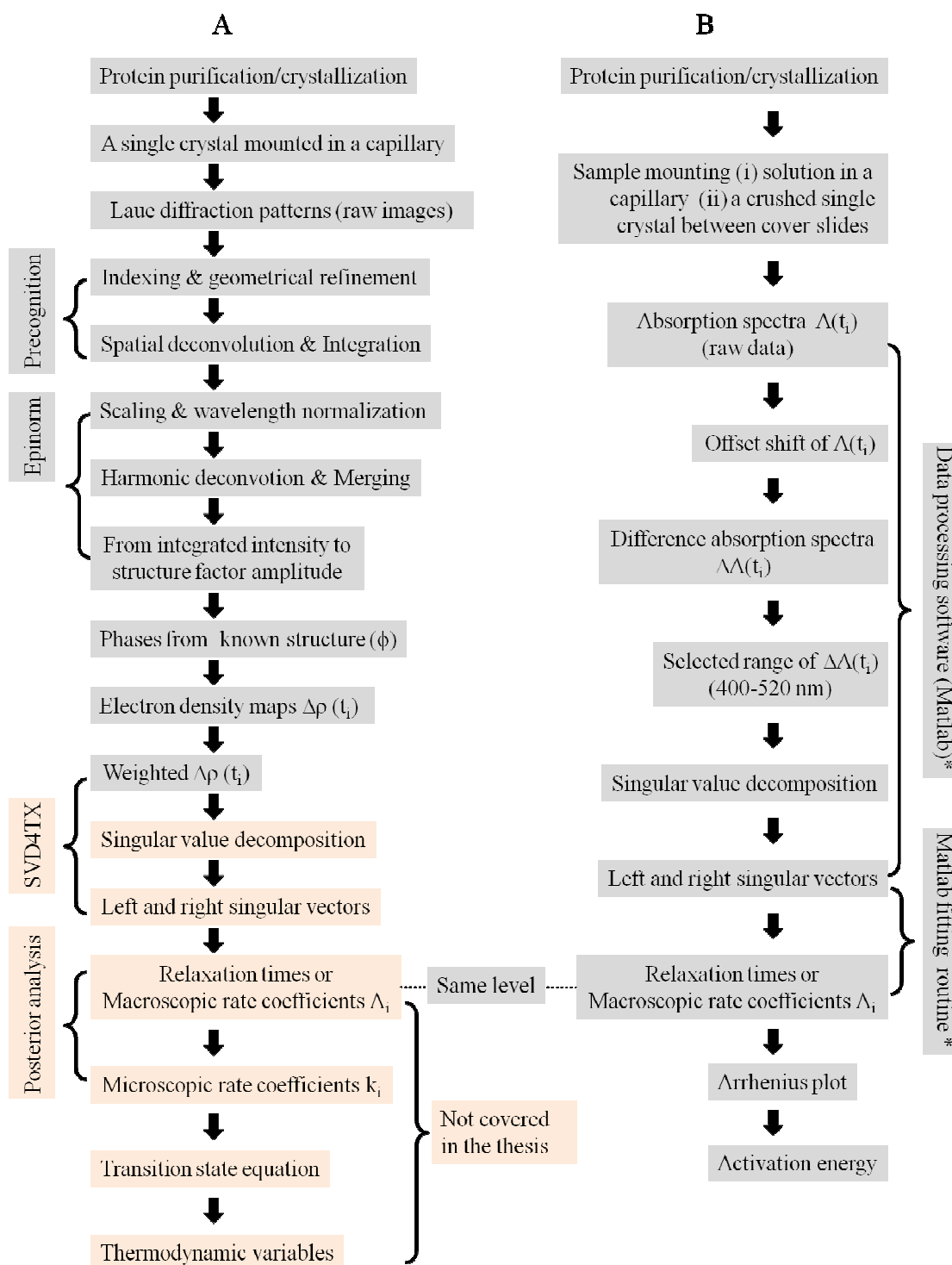
2.2.11 Data collection

A time range that covers a reaction from the nanoseconds to the end is selected. Time delays (N_t) are equally distributed on the logarithmic scale with typical 3 time points per logarithmic decade. Once a time series is collected from one particular crystal orientation, the crystal is rotated by an angle $\Delta\theta$ for another orientation. These orientations are selected such that they are maximally spaced across reciprocal space. The advantage of this protocol is that if an experiment terminates prematurely, the collected data don't have any preferred orientation. One can calculate a meaningful electron density map even from an incomplete data set. The angular range $\Delta\theta$ depends on the bandpass of the employed radiation (Ren *et al.*, 1999). The values of $\Delta\theta$ between $2 \sim 3^\circ$ are usually sufficient. Each time when a crystal is reoriented, it is also translated along its long axis so that a fresh volume can be exposed (Fig. 2.14B). In this type of data collection, time acts as a fast variable and orientation as a slow one. For a complete data set, Laue images at several different orientations (N_o) of the crystal must be collected. Usually, the number of photons in a single pulse even from the strongest X-ray source is not enough to produce a sufficiently strong diffraction pattern. Three to seven X-rays exposures (N_p) are required per diffraction pattern for an acceptable signal to noise ratio depending on the crystal size. A typical Laue diffraction pattern obtained for PYP with 4 X-ray exposures is

shown in Fig. 2.8B. Between two exposures, one should wait for enough time so that the sample can revert to its initial state. The waiting time depends on the velocity of the reaction. For a fast reaction, the waiting time can be short. A reference or dark data without laser illumination must be collected for each crystal to minimize the crystal specific errors.

2.2.12 Data reduction by Precognition

The goal of data reduction is to determine the accurate reflection intensities from the raw Laue diffraction images (Fig. 2.15A). For that, a software package *Precognition* and *Epinorm* (RenzResearch) is used. The first steps are indexing and integration, which are performed with *Precognition*. The final steps is scaling for which *Epinorm* is used. Indexing is the assignment of the Miller indices to all spots on a Laue image. Indexing is typically required only for one image because angular relations between the indexed and all other patterns are known. An initial estimate of the unit cell parameters and crystal orientations is obtained. The best orientation can then be selected based on number of matched spot as well as on the root mean square deviations (RMSD). With this selected orientation, the displacements between the observed and predicted spots in the indexed pattern are then minimized by adjusting the geometrical parameters such as unit cell and detector parameters. This process is known as geometrical refinement. The RMSD and the number of matched spots are the two criteria, which are inspected to judge the quality of refined data. Once the indexed image is properly refined, its best orientation is distributed to all other images. These images are refined with respect to the first indexed image. The next step is to integrate the Laue spots in the images. Before we do that, overlapping spots must be separated.



For example, spatially overlapped reflections are deconvoluted using analytical profile fitting as discussed in the Sec. 2.2.3. On the other hand, resolving harmonically overlapped spots (Sec. 2.2.5) is not straightforward. As mentioned, a lambda curve (Sec. 2.2.4 & Fig. 2.12) is first generated and then applied to separate these spots. Integrated intensities for the resolved diffraction spots are then obtained.

2.2.13 Scaling by *Epinorm*

Integrated reflection intensities from diffraction images corresponding to the different orientations are on different scale. *Epinorm* is used to bring them on the same scale. For that, an initially estimated λ -curve is used for wavelength normalization (Sec. 2.2.4). Scaling parameters are then applied to these normalized integrated intensities. Once all the reflection intensities are brought to the same scale, the final step is to merge all the redundant and symmetry-related intensities. As a result, a list of unique reflection intensities is obtained, from which structure factor amplitudes can be determined.

2.2.14 From structure factor amplitudes to electron density maps

After data processing, structure factor amplitudes of the initial dark state $|F_{obs}^D(hkl)|$ and a corresponding set of time dependent structure factor amplitudes $|F_{obs}(hkl, t)|$ are obtained (Fig. 2.15A). To generate electron density maps, not only structure factor amplitudes but also phases are required. For time-resolved experiments, the dark state model must be available. From this model, the calculated structure factor amplitudes $|F_{calc}^D(hkl)|$ with their phases ϕ_{calc}^D can be obtained. Observed structure factor amplitudes of dark $|F_{obs}^D(hkl)|$ are scaled to the calculated one $|F_{calc}^D(hkl)|$ and hereby brought to the absolute scale (Schmidt *et al.*, 2010). The time-dependent observed

amplitudes $|F_{obs}(hkl, t)|$ are then scaled to the reference data in order to bring them also on the absolute scale. Difference structure factor amplitudes $\Delta F_{obs}(hkl, t)$ for each time point are calculated by subtracting $|F_{obs}^D(hkl)|$ from the $|F_{obs}(hkl, t)|$. The difference amplitudes $\Delta F_{obs}(hkl, t)$ corresponding to each time point are multiplied by a weighing factor w , which is given by

$$w = \frac{1}{1 + \frac{\sigma^2}{\langle \sigma^2 \rangle} + \frac{\Delta F(hkl, t)^2}{\langle \Delta F(hkl, t)^2 \rangle}} \quad (2.24)$$

where σ is the standard deviation of $|\Delta F_{obs}(hkl, t)|$. This ensures that the observations with large uncertainties and those with large differences in structure factor amplitudes are down-weighted for the difference map calculation. The weighted difference structure factor amplitudes are normalized by the average weighing factor to keep them on the absolute scale. Phases ϕ_{calc}^D calculated from the dark state model are combined with weighted difference structure factor amplitudes $w|\Delta F_{obs}(hkl, t)|$. Weighted time-dependent difference electron density $\Delta\rho(t)$ are calculated as

$$\Delta\rho(t) = \frac{1}{V_e} \sum_{hkl} w|\Delta F_{obs}(hkl, t)| e^{i\phi_{calc}^D(hkl)} e^{-2\pi i(hX+kY+lZ)} \quad (2.25)$$

where X , Y , and Z are components of the position vector in the coordinate system of unit cell, h , k , and l are indices of Laue reflections, V_e is the volume of unit cells, w is the weighting factor of the difference structure factor amplitudes $|\Delta F_{obs}(hkl, t)|$. Electron density on an absolute scale directly relates to the occupancy or fractional concentration if the structural differences are small and noise is moderate. This is referred to as the

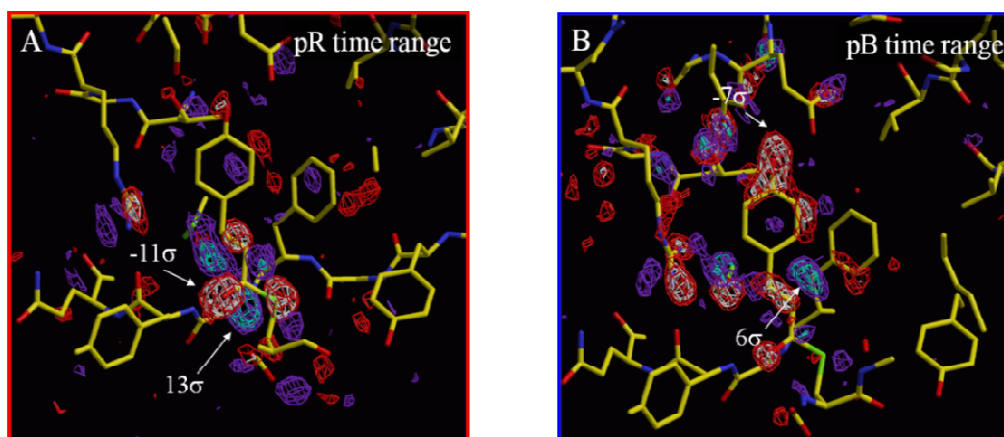


Figure 2.16 Difference maps near the p-cinnamic acid (pCA) chromophore in PYP. The dark state model is shown in yellow, red and blue representing carbon, oxygen and nitrogen atoms, respectively. Positive electron density features: blue or cyan, negative electron density features: red or white. Contour levels: red/white ($-3\sigma/-4\sigma$), blue/cyan ($+3\sigma/+4\sigma$) **A.** Dark subtracted from intermediate state pR. **B.** Dark subtracted from intermediate pB.

difference approximation. The obtained electron density maps can be inspected with the program Xfit as also mentioned in the monochromatic method. A typical difference electron density map is shown in Fig. 2.16. Positive and negative electron density peaks are observed in these difference maps. Negative electron density features represent the loss of electrons and account for those atoms which were present at a given position in the dark model and have moved away from their positions to occupy new positions. On the other hand, the positive electron density features denotes the gain of electrons and account for the new positions occupied by atoms.

2.2.15 Singular value decomposition of difference electron density map

The time courses of weighted difference electron density maps are analyzed by singular value decomposition (SVD) using the program SVD4TX (Schmidt *et al.*, 2003, Zhao & Schmidt, 2009).

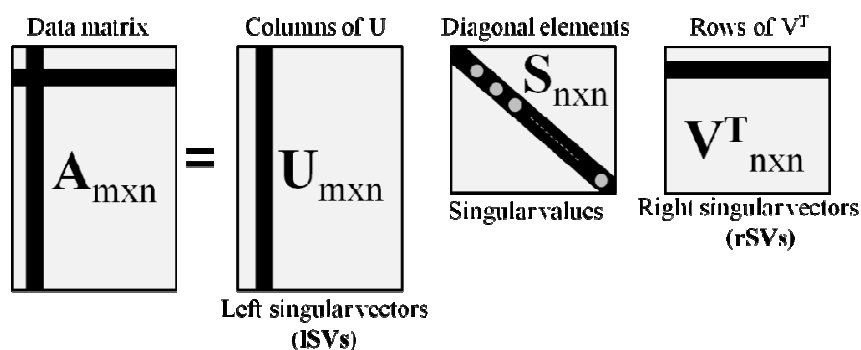


Figure 2.17 A scheme of Singular value decomposition (SVD). The data arranged in a matrix $A_{m \times n}$. The matrix A is decomposed into the matrix $U_{m \times n}$ containing left singular vectors, the diagonal matrix $S_{n \times n}$ having diagonal elements and the matrix $V_{n \times n}^T$ with right singular vectors.

In the difference electron density map, a confined region is specified for the SVD analysis because other parts of the map do not contain valuable information and add only noise to the analysis. First, those regions are selected for the mask where large changes in the electron density map are expected. The mask is then evolved by allowing only those grid points where the difference electron density is above or below a certain σ level that occur at least in one time point (The σ value represents the root mean square deviation of the difference electron density maps from the mean value determined for all the grid points). The masked data is arranged in a data matrix (A) which is then decomposed by SVD into left singular vectors (columns of U), right singular vectors (columns of V) and corresponding singular values (diagonal elements of S) such that $A = USV^T$ (Fig. 2.17). The left singular vectors (LSVs) contain the time independent structural information. The temporal variations of these LSVs are contained in corresponding right singular vectors (rSVs). Singular values obtained from the diagonal matrix imply the number of significant rSVs. Typically, the first couple of rSVs are significant and all other contain noise. For example, if two significant singular vectors are present, the first LSV represents

an average of the difference electron density maps and first rSV describes its time dependence. The second lSV contains the deviation from the average difference maps and its temporal variation is described in the second rSV. In general, the number of significant vectors is equal to the number of kinetic processes involved in a reaction.

2.2.16 Kinetic analysis of Laue data

A major step to perform the kinetic analysis involves the determination of relaxation times of the associated kinetic processes. The time-traces of significant rSVs are a linear combination of the true time-dependent concentrations of the associated intermediates. The significant rSVs are fitted globally with a sum of exponentials. The equation for fitting of j rSVs with i relaxation times can be written as

$$rSV_j = A_{0,j} + \sum_{i,j} A_{i,j} e^{-\frac{1}{\tau_i}t} \quad (2.26)$$

where j is the number of significant rSV, i is the number of exponentials required for the fitting, A_{ij} is the amplitude of i^{th} exponent term for the j^{th} rSV. Associated relaxation times (τ_i) and corresponding macroscopic rate coefficients ($\Lambda_i = 1/\tau_i$) can then be calculated which infer the number of kinetic processes evolved after reaction initiation.

2.2.17 Posterior analysis

In a time-resolved diffraction experiment, each time-dependent difference electron density map $\Delta\rho_t$ in a time-series may consist of a mixture of two or more intermediates. The extent of this mixture depends on the underlying chemical kinetic mechanism. Once the structures of these intermediates are known, the observed $\Delta\rho_t$ can be fitted by the

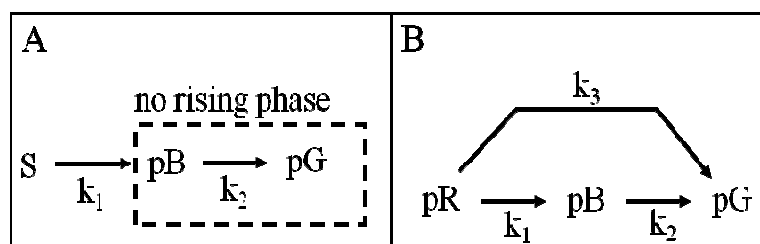


Figure 2.18 Two examples of kinetic mechanisms used for slower part of the PYP photocycle. **A.** From source S , intermediate pB forms with rate coefficient k_1 . The pB decays into ground state, pG with the rate coefficients k_2 . **B.** From the intermediate pR , another intermediate pB forms with k_1 , which then further decays into the ground state pG with the k_2 . An alternate path from the early intermediate pR to the pG with rate coefficient k_3 is also possible.

calculated time-dependent difference electron densities using posterior analysis. This analysis is equivalent to kinetic target analysis (van Stokkum *et al.*, 2004) and is performed using the program GetMech (Schmidt *et al.*, 2004, Schmidt, 2008). A given reaction can be appropriately defined by several kinetic mechanisms; however for the analysis, a simplified mechanism should be selected. For example, two kinetic mechanisms that can be employed for the slower part of the PYP photocycle are shown in Fig. 2.18. In the first one (Fig. 2.18A), the intermediate pB forms from a not nearer specified source S with the rate coefficient k_1 . The pB then decays to the ground state pG with k_2 . In Fig. 2.18B, two intermediates pR and pB are involved. pB forms from the pR with the k_1 and decays into pG with the k_2 . An alternate path from the pR to pG is also possible with k_3 . All the calculations regarding posterior analysis are performed by Prof. M. Schmidt. However, for a better understanding, the results obtained from these analyses are also discussed in the thesis.

2.3 Time-resolved spectroscopy

2.3.1 UV-Vis radiation

The chromophore (Fig. 2.19) is responsible for the color of biomolecules. If this molecule is excited, the energy difference between the ground and excited state may fall within the range of either the visible or the ultraviolet spectrum. Therefore, these portions of the electromagnetic spectrum are appropriate for UV/Vis spectroscopic investigations.

2.3.2 Chromophore

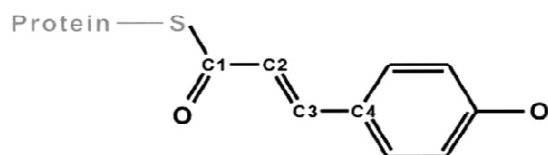


Figure 2.19 Chromophore of photoactive yellow protein (PYP). *S* denotes the thioester bond through which the chromophore is linked to the protein.

The chromophore is an aromatic system in which mesomerically coupled double bonds exist. The valence band electrons are delocalized and can freely move within the bonding network. When a chromophore molecule is illuminated with visible light of a certain wavelength, configurational (*trans/cis*) changes occur. This may trigger conformational changes of the protein. For example, if the chromophore of photoactive yellow protein (PYP) absorbs a blue photon, it isomerizes from the *trans* to the *cis* configuration. As a result, large conformational changes may occur in the surrounding protein matrix of PYP.

2.3.3 Beer-Lambert law

When visible light passes through a sample, certain wavelengths are absorbed and others are transmitted. Absorption depends on the chemical species present in the sample. The absorbance of a chemical species in a given sample can be calculated using the Beer-Lambert law which is given by

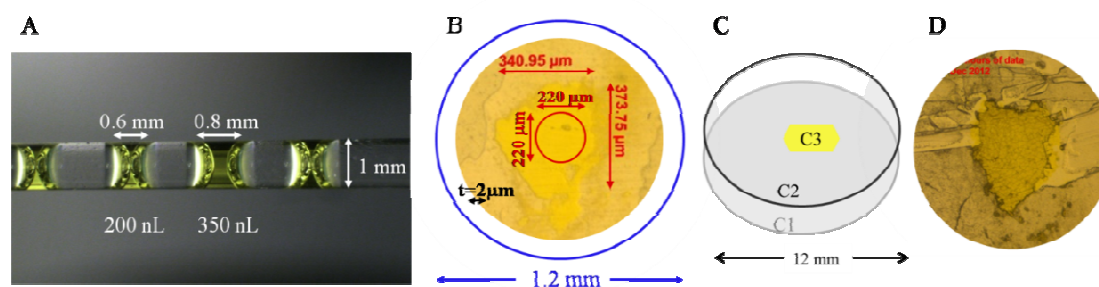


Figure 2.20 Two types of samples are used for the time-resolved spectroscopic experiments. **A.** An image of the capillary with the PYP solution. Three drops of size ~200 nL and one drop of size ~350 nL are mounted together in a single capillary. **B.** A PYP crystal crushed between two cover slides. The thickness of the crushed crystal is approximately ~2 μm . Laser light (blue circle) and visible light (red circle) are focused to a spot size of $1.2 \times 1.2 \text{ mm}^2$ and $220 \times 220 \mu\text{m}^2$, respectively. **C.** Scheme of a crystalline sample, where C1 and C2 represent two cover slides placed on the top of each other and C3 denotes a protein crystal (yellow) squeezed in between. **D.** Sample not sealed properly. Crystals of ammonium sulfate start to form.

where A is the absorbance of a particular specie, I_0 is the intensity of incident light, I is the intensity of light transmitted through the sample, ϵ is the extinction coefficient ($\text{cm}^2 \text{mmol}^{-1}$) also known as absorptivity, l is the optical path length, c is the concentration of that specie in the sample. The absorbance is reliable below ~1.5 absorption units (a.u.), because nonlinear effects start to appear for values higher than that.

2.3.4 Time-resolved spectroscopic investigations

Similar to time-resolved crystallography (Chapter 1 & 2), a laser pulse of a particular wavelength is used to trigger a reaction in a protein. The subsequent spectroscopic changes are then probed with visible light at different *time delays* Δt_i after the laser pulse. Instead of probing structural changes with X-rays, here we monitor spectroscopic

changes. With time-resolved spectroscopy, the evolution as well as the decay of several intermediates in the protein can be examined.

2.3.5 Sample preparation

2.3.5.1 Protein solution in a capillary

The concentration of a protein sample is optimized such that its maximum absorbance A_{max} lies in the range of ~ 1 a.u.. A suitable buffer (2.7M ammonium sulfate, 50mM sodium phosphate, pH 7.0) is used for the dilution of the protein in order to adjust its concentration. The optimum concentration varies for different proteins and its typical value varies from 1 to 4 mg/mL. A drop of 200~800 nL protein solution is placed in a glass capillary of diameter 1mm (Fig. 2.20 A). A similar sized drop of dilution buffer (not shown) is also placed in the capillary so that the absorption spectrum collected for the buffer can be subtracted from those obtained for the protein. This eliminates the effects of the dilution buffer on the protein spectra. Three to five drops of a protein may be mounted in a single capillary so that several experiments may be performed with the same capillary. This avoids the mounting of a new sample each time when the sample in a particular drop is bleached or destroyed. Epoxy is used to properly seal the capillary in order to avoid drying out of the protein solution.

2.3.5.2 Protein crystals crushed between the cover slides

Protein crystals may be unusually optically thick. PYP for example has a molar absorption coefficient of $45500 \text{ cm}^2 \text{ mmol}^{-1}$ at 446 nm. The monitoring light is significantly absorbed. If the PYP concentration in its crystalline form is ~ 100 mM, a crystal of thickness $200 \text{ }\mu\text{m}$ corresponds to ~ 100 a.u.. These high values are impossible to measure. To obtain absorption spectra whose absorbance unit ~ 1 a.u., a crystal of

thickness 2 μm is required. To fulfill this requirement, crystals are crushed to produce a micron thin layer of crystalline sample. This significantly reduces the optical path of the probing beam through the sample. For the sample preparation, a small drop of stabilization buffer is placed on the siliconized cover slide (Hampton Research) of diameter 12 mm (Fig. 2.20B & C). A protein crystal is then looped and immersed properly in the drop of buffer. The stabilization buffer is not only necessary to prevent the disintegration of protein crystals but also it keeps the crystal moist. The crystal is covered by another cover slide of the same size and then gently squeezed in between to achieve the required thickness. This assembly is quickly sealed with epoxy. If the sample is not sealed properly, crystals of ammonium sulfate used in the stabilization buffer start to form (Fig. 2.20D).

2.3.6 Sample mounting

A setup where we have mounted the sample is shown in the Fig. 2.21A. A capillary Cp containing the protein solution can be easily mounted on the goniometer such that its long axis is perpendicular to both the laser and the visible light (IVL) (Fig. 2.21A & B). This ensures that the sample volume which is illuminated by the laser pulse can be probed. On the other hand, mounting of the cover slide is not that straightforward, because the cover slide has a flat circular area and cannot be placed perpendicular to both laser and visible light. To probe the illuminated volume, the cover slide has to be tilted by $40\sim 45^\circ$ towards the direction of laser light as shown in the Fig. 2.21C. The illuminated volume is further maximized by tilting the laser beam about $\sim 30^\circ$ from the horizontal direction (Fig. 2.21C). With these geometrical adjustments, a given sample volume that lies in a tilted

plane can be easily illuminated with the laser pulses. The illuminated volume can then be probed with the visible light.

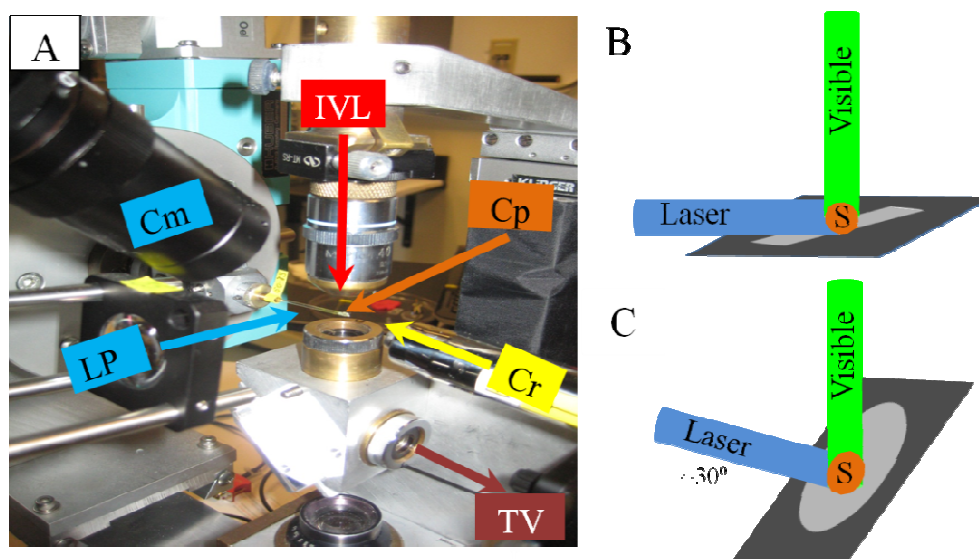


Figure 2.21 *A. Image of the sample environment of our micro-spectrophotometer setup. LP: laser pulse, IVL: incident visible light, TVL: light transmitted through the sample, Cm: camera Cr: cryojet stream, Cp: Capillary. Cp containing protein solution is mounted on the goniostat. B. A drop of protein solution, S (orange) mounted in the capillary (light grey rectangle). The capillary is in the horizontal plane (dark grey). It is also perpendicular to both the laser (blue) and the visible light (green). C. A crystal, S (orange) is crushed between two cover slides (light grey ellipses). The cover slides are in a plane that is tilted (dark grey) towards the laser light. To optimize the overlap between laser and visible light, the laser beam is also tilted around 25~30° towards the visible light as shown.*

2.3.7 Setup of a self-designed fast micro-spectrophotometer

A scheme for all the components involved in the setup is shown in Fig. 2.22A. For a reaction initiation in the sample, a nanosecond laser pulse (PL) from an Opotek HE 355II laser is used. A polarizer, POL (Glan Laser ThorLabs) is used to attenuate the laser beam as necessary. The beam is focused and coupled to a 600 μm fiber OF1, which is used to transport the light to the sample. The intensity of a laser beam should be tuned such that it contains enough photons to effectively trigger a reaction but does not destroy the protein.

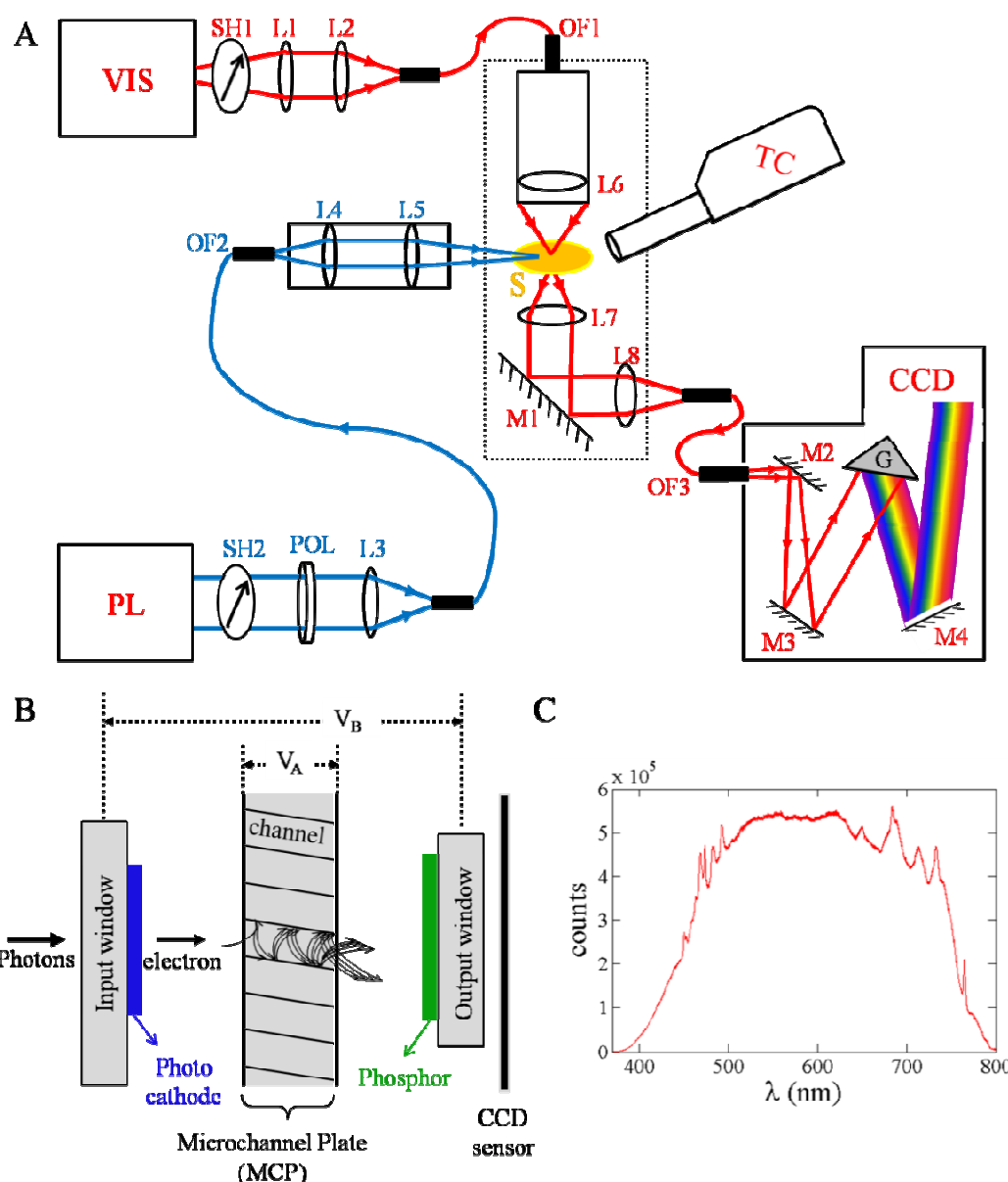


Figure 2.22 A. A scheme of the in-house microspectrophotometer designed in our lab. PL: Opollete HE II pulsed laser, VIS: visible light source, SH1-2: Shutters, POL: polarizer, OF1-3: optical fibers, L1-8: lenses, M1-4: mirrors, G: grating, TC: cryojet stream. **B.** Scheme of the image intensifier tube equipped with a microchannel plate, MCP. A photocathode (in blue) emits electrons upon incident photons of a particular wavelength. V_A : voltage between input and output window, V_B : voltage across the MCP. The MCP comprises many channels (slightly tilted horizontal lines). The photoelectrons accelerate while passing through these channels. The accelerated electrons generate secondary electrons (curved lines), which are converted to photons by the phosphor screen (in green). The amplified intensity is finally detected by CCD sensor (vertical line). **C.** A typical spectrum of the Xenon light source employed for optical monitoring of a protein sample.

Shutter, SH2 (ThorLab, SC10) is used to avoid accidental exposure to the laser beam. To probe the spectral changes in the sample after the laser excitation, a continuous visible light source (VIS, Asahi spectra Xe 300W) is employed. Its spectrum acquired from our spectrophotometer is shown in the Fig. 2.22C. Another shutter, SH1 (ThorLabs, SC10) is used to expose the sample to the visible light only for a short period of time. The minimum opening time depends not only on the shutter mechanism but also on the employed electronics. For our setup, a minimum opening time of 12~15 ms is possible. The visible light is coupled into tapered fiber, OF2, and focused to a spot size of $220 \times 220 \mu\text{m}^2$ at the sample position, S. Light transmitted through the sample is collected into a $400 \mu\text{m}$ optical fiber, OF3, which is focused using a lens (L6-L8) and mirror (M1) assembly (courtesy Bio-cars, enclosed in black dashed rectangular box as shown in the Fig. 2.22A). The light is then sent to the spectrophotometer, Shamrock 303 (Andor technology), where it is dispersed into different wavelengths by a diffraction grating, G. The dispersed beam is captured by a charge coupled device (CCD) sensor which is open for a certain period of time referred to as *exposure time*¹. In our spectrophotometer, the CCD camera (Andor istar) is equipped with an image intensifier tube (Fig. 2.22B). The tube contains a photocathode which emits electrons while photons are incident on it. Depending on the voltage V_B , these photoelectrons reach the microchannel plate, MCP, of thickness 1 mm (Andor iStar manual). This plate consists of many channels whose widths are $10 \mu\text{m}$. Since a high voltage V_A in the range of 600 ~ 1000 V is applied across

¹ Words in italic in chapter 3 represent the terms that are related with synchronization and timing scheme of the micro-spectrophotometer.

the MCP plate, photoelectrons cascade down the channel. As a result, secondary electrons are generated. The clouds of electrons are then converted to visible light photons by a phosphor screen. This way, the incident light is amplified and reaches the CCD chip. The amplification factor depends on the voltage V_A , which is denoted as the *MCP gain*. A higher MCP value may be selected for those spectra having a weak photon count. Signal to noise ratio can also be improved by averaging multiple spectra. The number of spectra to be averaged is referred to as *accumulation number*. The image intensifier can also be time-gated such that the intensifier is open for a given period of time at a desired *time delay* Δt_i after a trigger. The Q-switch pulse from the laser may act as a trigger. The duration for which the intensifier tube opens is referred to as *pulse width*. In a typical spectrophotometer, there is a minimum response time between receiving an external trigger as an input and the execution of a program initiated by the trigger. This response time is denoted as *insertion delay* here. This delay defaults to a certain value which varies for different spectrophotometers. The delay for our spectrophotometer is 34 ns. A cryojet stream (Oxford HT II) is used to control the temperature at the sample position. Temperatures in the range of -150 to 300 °C can be maintained by using the gas stream.

2.3.8 Timing scheme for synchronization

The synchronization scheme as shown in the Fig. 2.23 is described in the following. The laser flash lamp is operated with a frequency of 20 Hz. An electronic pulse of the laser flash lamp output is fed into a digital delay generator (DG645, Stanford Research Systems). As a result, the DG645 is externally synchronized with the laser flash lamp. A

100 μ s pulse is generated with the DG645 and then delayed by 146 μ s with respect to the flash lamp pulse. This pulse is used to externally trigger and activate the Q-switch. A delay of 146 μ s is selected because with this delay the maximum intensity of the output laser pulse can be obtained. After 40 ns of the Q-switch trigger, the light pulse exits from the laser and subsequently excites the sample. The Q-switch output is sent to the iStar camera of the spectrophotometer which has an *insertion delay* of 34 ns as mentioned earlier. The value of *insertion delay* smaller than 40 ns ensures that the data collection sequence can be started 6 ns before the sample is hit by the laser pulse. All the important variable settings such as *time delays*, *accumulation numbers*, *pulse widths*, *CCD exposure times*, *relaxation times* between two successive frames and *MCP gains* are provided by the data collection software. These variables are explained in section 3.3.8. The electronic output pulse from the spectrophotometer also called *gate monitor pulse* is amplified with another digital delay generator (DG545 courtesy BioCARS). The amplified pulse is then delayed before it is used to operate the visible light shutter SH1 as shown in the Fig. 2.22A. With this generator, the time at which the shutter is opened can be exactly controlled and changed accordingly for all the *time delays*.

The timing scheme for synchronization has recently been modified in our lab (Purwar *et al.*, 2013) (not used in this thesis). In the updated scheme, the pulse that activates the iStar CCD and collects a time-point is externally delayed by the DG645. The dependency of the *exposure time* on the *time delays* is eliminated. Consequently, the effects of dark currents that were large in the previous scheme can be greatly minimized. The flashlamp TTL output is directed to DG645 as an external trigger as in the original scheme, however the Q-switch is activated by a pulse from DG645 delayed by about 50 ms. This

provides enough time to open the Xe light shutter (SH1 in Fig. 2.22A). As a result, the first laser pulse can be utilized for the data collection purposes. Time-resolution is also improved.

2.3.9 Display of selected pulses during data collection

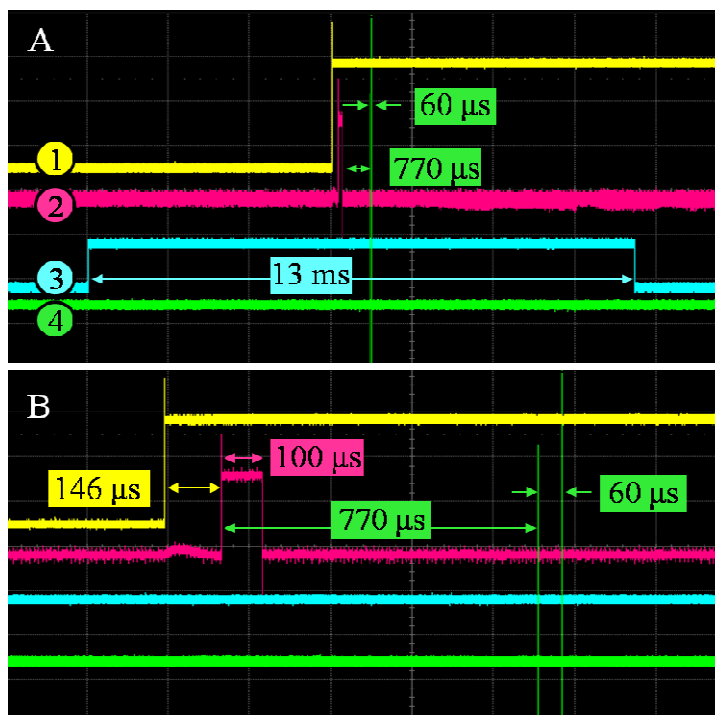


Figure 2.23 Electronic pulses monitored with the oscilloscope during time-resolved spectroscopic experiments. Pulse 1 (yellow): reference pulse from the DG645; Pulse 2 (magenta): output pulse from the Q-switch of the laser; Pulse 3 (cyan): output pulse from the visible light shutter; Pulse 4 (green): output gate monitor pulse from the Andor iStar spectrophotometer. The 4th pulse denotes the time during which the image intensifier of iStar is open. **A.** A reaction is started with the laser pulse and changes are probed for 60 μ s at the time delay of 770 μ s. The minimum possible time 13 ms is shown during which the visible light shutter is open. **B.** An enlarged view of panel A. The delay of 146 μ s between the flash lamp pulse (yellow) and the Q-switch pulse (magenta) is selected to maximize the intensity of the laser pulse. 3rd and 4th pulses are the same as described above.

A digital oscilloscope (LeCroy40S, 400MHz) is used to monitor input and output pulses before and during the experiments. Four pulses can be inspected at the same time (Fig.

2.24). The selection of these pulses is described in the following. The reference pulse from DG645 that trigger and operate the Q-switch is selected as the first one to be displayed. This pulse is also used as a trigger for the oscilloscope. Output pulses from the Q-switch and from the visible light shutter are displayed as second and third ones, respectively. The last pulse to be monitored is the output gate monitor pulse from the Andor iStar spectrophotometer.

2.3.10 Description of the Andor Basic data collection software

The data collection software is written in an Andor proprietary programming language called Andor Basic. A list of desired *time delays* is generated with a Matlab script such that all the *time delays* are equally distributed on a logarithmic time scale with at least 3 to 4 time points per logarithmic decade. Typically a time range from several nanoseconds to seconds can be covered. The Matlab generated *time delays* are scripted manually into the data collection sequence. The correct *exposure times* has to be determined for each *time delay*. The *exposure time* must at least be equal to the sum of a particular *time delay* and the corresponding *pulse width*. This is one of the limitations for the *exposure time* mandated by the Andor spectrophotometer. Another imperative limitation is that the minimum possible *exposure time* is 2 ms. With our current setup, time points as fast as 20 μ s can be investigated. For time points faster than that, not enough photons reach the sensor. For fast *time delays* a pulse width of 20 μ s is selected to obtain absorption spectra. Then the corresponding *exposure times*, that fulfill the minimum criteria set by the instrument as described before, are computed. For time scales such as 25 μ s ~ 500 ms, the ratio of the *pulse width* and the *exposure time* falls between 0.8 ~ 0.04 (Fig. 2.25A). The effects of the dark current are negligible for these spectra (Fig. 2.25D). In order to further

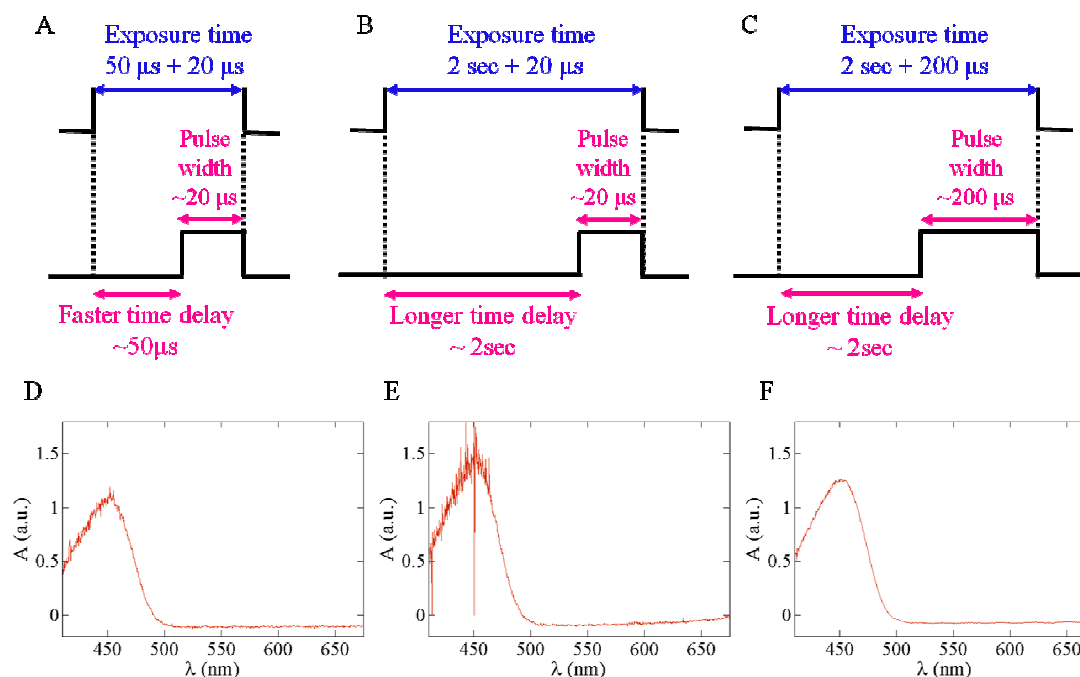


Figure 2.24 Reasons for the CCD dark current and their effects on the absorption spectra at different time delays. **A.** For the time delay $50\ \mu\text{s}$ with pulse width of $20\ \mu\text{s}$, the ratio of pulse width to exposure time is large enough and almost no effects of the dark current are observed in the spectrum (Panel D) **B.** For the time delay $2\ \text{s}$ with the pulse width of $20\ \mu\text{s}$, this ratio is very small which leads to significant dark current. The spectrum becomes noisy (Panel E). **C.** For the same time delay of $\sim 2\ \text{sec}$, the pulse width is increased to $200\ \mu\text{s}$. This setting provides a higher pulse width to exposure time ratio. This can substantially suppress the dark noise (Panel F).

enhance the intensity of these spectra, a *MCP gain* of 50 is applied. With this gain, smooth spectra can be obtained for *time delays* from $25\ \mu\text{s}$ to $\sim 500\ \text{ms}$. In the case of longer *time delays* ($1 \sim 5\ \text{s}$), the *exposure times* become relatively large due to instrument limitations; however, the *pulse width* is short as mentioned earlier. As a consequence, the ratio of *pulse width* to *exposure time* is extensively small (Fig. 2.25B) and the spectra become very noisy (compare Fig. 2.25D & E). In order to reduce the effects of dark current, a relatively large *pulse width* between $1\sim 2\ \text{ms}$ can be selected. This leads to a high *pulse width* to the *exposure time* ratio (Fig. 2.25C), which minimizes the influence

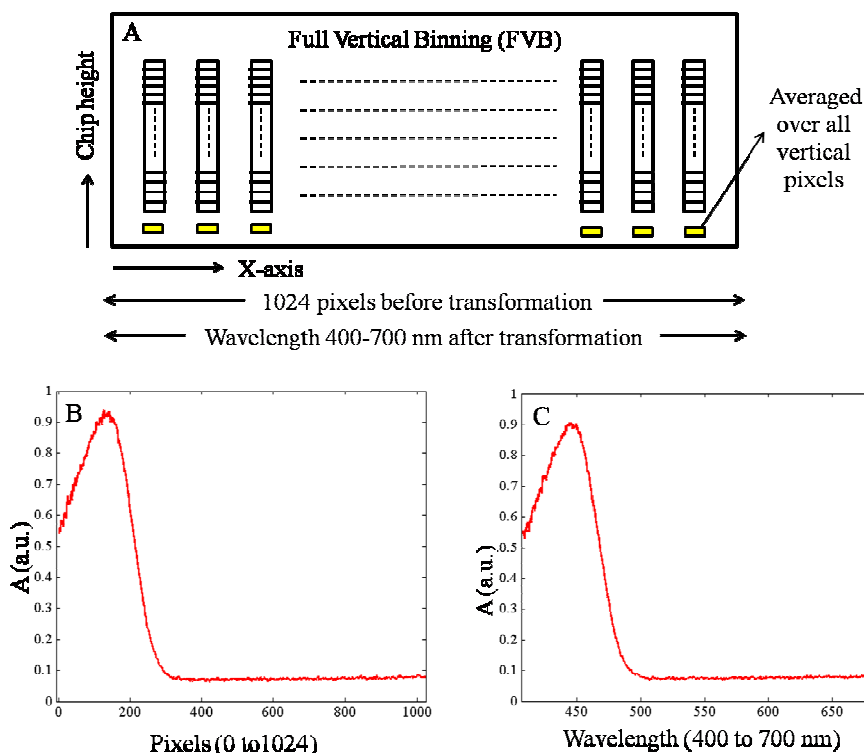


Figure 2.25 A. A charge couple device (CCD) of the Andor iStar with full vertical binning (FVB) as a read out mode. 1024 pixels are distributed on the X-axis. These pixels can be mapped to a given wavelength range. Absorption spectra of PYP plotted as a function of B. CCD pixels before calibration. C. wavelength after calibration.

of the dark current (Fig. 2.25F). If the *pulse widths* are long and a *MCP gain* of 50 is applied, the spectra start to saturate. The *pulse width* must be selected such that both the dark current and saturation effects are the smallest possible. For the longer *time delays* (1 ~ 5 s), *pulse widths* from 170 to 200 μ s are suitable. A common *MCP gain* of 50 is chosen for all the *time delays* to minimize the background effects. These background noises originate when different *MCP gains* are selected for different *time points*. To improve the signal to noise ratio even more, multiple frames can be averaged for each *time delay*. About forty to fifty *accumulations* are necessary for *time delays* up to 100 μ s whereas 15 ~ 20 exposures are enough for longer *time delays*. Once all the parameters

such as *pulse widths*, *exposure times*, *accumulations* and *MCP gains* are set for each *time delay*, transmitted spectra at these settings can be collected. First, the background transmission spectra $T(\lambda)_{\Delta t}^{bg}$ without any visible light and then the reference spectra $T(\lambda)_{\Delta t}^{ref}$ with visible light and without any protein are collected for each *time delay*. After that, the signal spectra $T(\lambda)_{\Delta t}^{sig}$ at the sample position are collected. From these, absorption spectra at different time delays $A(\lambda)_{\Delta t} = -\log\left(\frac{T(\lambda)_{\Delta t}^{sig} - T(\lambda)_{\Delta t}^{bg}}{T(\lambda)_{\Delta t}^{ref} - T(\lambda)_{\Delta t}^{bg}}\right)$ can be calculated. As a reference, dark absorption spectra $A(\lambda)_D$ without any laser excitation are also obtained before and after collecting the time-resolved data. The data collected at different *time delays* are saved according to their progression in time and a comprehensive time series is obtained.

During the data collection, wavelengths in the absorption spectra (Fig. 2.25B) are by default mapped to pixel positions on the CCD chip (Fig. 2.25A). There are total 1024 pixels in the x-direction. The pixel positions must be transformed into wavelengths (Fig. 2.26A & C). This requires calibration. Our system can be easily calibrated by using a known calibration source such as CAL2000. It produces mercury and argon atomic emission lines from 253 to 922 nm, whose pixel positions are known. Few distinct peaks are selected and their pixel positions are captured. These data points can be fitted by a linear, quadratic or a cubic fit. Although the spectral resolution of the detector is 12 nm due to its point spread function, the use of grating with 1199 lines/mm enables us to distinguish peaks that are only 0.1 nm apart with an accuracy of ± 0.2 nm.

2.3.11 The Matlab data analysis program

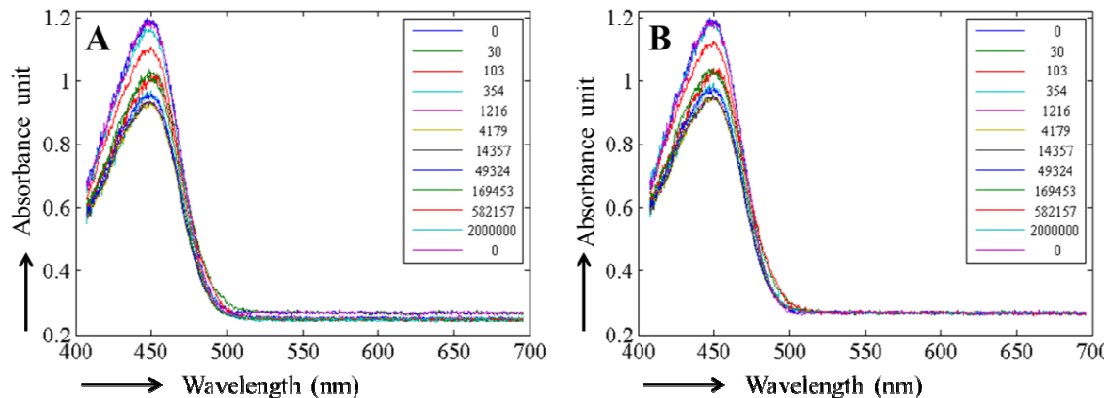


Figure 2.26 Typical examples of time-resolved absorption spectra collected on PYP solution at ambient temperature. **A.** A time series of ten absorption spectra from 30 μ s to 2 sec. As evident, offsets corresponding to each spectrum are slightly different from each other. **B.** The absorption spectra are shifted with respect to the reference spectra and brought to the same level.

For the analysis of the dark and the light data, a self-written Matlab program is used. The absorption spectra for each *time delay* are plotted (Fig. 2.27A). There is a slight offset relative to the X-axis which is different for each spectrum. These offsets are shifted to the offset of the corresponding dark spectrum (Fig. 2.27B). For that, the spectral range from 550 to 700 nm, where no spectral changes occur, is used. Once brought to the same offset, time-dependent difference absorption spectra are calculated. The time and wavelength dependence of the difference spectra are analyzed by SVD. This analysis has already been discussed for time-resolved crystallography, where it is applied to the difference electron density maps (Sec. 2.2.15). The basic concept is the same whether SVD is applied to the X-ray data or to the spectroscopic data. Here, we focus on the details that apply to the spectra. A wavelength range in which largest changes in the difference absorption spectra occur is selected. For example, in Fig. 2.27 significant changes are observed in the wavelength range from 400

to 520 nm and therefore this range should be selected for the SVD analysis. Spectral changes in other than the specified regions are omitted from the analysis because they do not contain signal and add only noise. Difference spectra in the selected wavelength range are arranged in a data matrix for the SVD (Fig. 2.17). After decomposition, the obtained left (lSVs) and right (rSVs) singular vectors contain spectral and kinetic information, respectively. All the significant rSVs are globally fit with a sum of exponentials using a fitting routine written in Matlab. Data fitting is tested with different number of exponentials. Too few exponentials do not fit the data properly, whereas too many exponentials do not improve the quality of fitting any further. Associated relaxation times (τ_i) and corresponding rate coefficients ($\Lambda_i = 1/\tau_i$) can then be calculated. τ_i infer the number of kinetic processes that evolve after a reaction is initiated.

2.4 Biochemical procedures

So far, we have described the employed techniques with experimental setups and associated hardware. In the following sections, we describe how biological samples such as catalase and PYP are prepared for our experiments. From the purification to the crystallization of these proteins, all necessary steps are described.

2.4.1 Beef liver catalase (BLC)

2.4.1.1 Purification

Bovine liver catalase (BLC) is obtained from sigma (C3155). To purify the protein, size exclusion chromatography is used in which proteins are separated based on their sizes or their molecular weights. Superdex 200 (GE) is selected as a gel filtration medium which is equilibrated with buffer consisting of 10mM Tris, 50mM NaCl, pH 8.5. Protein

molecules larger than the gel pore size are unable to diffuse into the gel and therefore eluted first. On the other hand, smaller protein molecules penetrate into the gel pores and elute later. The eluted catalase is collected in small fractions of 2 mL. Concentration of all these fractions can be calculated using the Beer-Lambert law. UV-Vis spectra obtained for each fraction provides the absorbance at 405nm (A_{405}). The extinction coefficient (ϵ) at the same wavelength is also known (Reid *et al.*, 1981). Its value is $420000 \text{ cm}^2 \text{ mmol}^{-1}$ for the tetramer. This allows us to quantify the catalase.

2.4.1.2 Purity assessment using absorption spectra

The 405nm band of catalase is due to the presence of four heme prosthetic groups which absorb at 405 nm. Aromatic residues are present in almost all proteins, and they absorb at 276 nm. The ratio ($A_{405\text{nm}}/A_{276\text{nm}}$) of the absorbance at 405 nm to that at 276 nm can be used to assess the purity of catalase. Only those catalase fractions whose ratio is larger than one are pooled. These protein fractions are concentrated to ~15 mg/mL. To the concentrated and purified catalase solution, 1-5 wt % of NH_4OH (30% in water) is added right before starting crystallization trials.

2.4.1.3 Crystallization

Catalase crystals are grown by the hanging drop vapor diffusion method. The crystallization conditions are used as reported previously (Ko *et al.*, 1999). Briefly, protein concentration of 12~13 mg/mL containing NH_4OH as described before is used. Four microliters of the catalase solution is mixed with an equal volume of the reservoir solution that contains 45~60 mM magnesium formate. After 2-3 weeks, crystals of typical size $100 \times 100 \times 200 \mu\text{m}^3$ are obtained.

2.4.2 Photoactive yellow protein (PYP)

2.4.2.1 Overexpression of PYP in *E. coli*

PYP-DNA from the original bacterium *E. halophila* is expressed in the host bacterium *E. coli*. Luria broth with ampicillin is used as a medium to grow bacteria. Once the OD₆₀₀ reaches to ~0.6, the bacterial growth is stopped by keeping them on the ice. Isopropyl β -D-1-thiogalactopyranoside (IPTG) is added to a final concentration of 1mM to induce overexpression of apo-PYP. Bacteria are further grown at 16 °C for ~22 hours. These bacteria are then collected by centrifugation and cell walls are ruptured by sonication. Lysozyme and protease inhibitor are added into the culture right before sonication. p-coumaric anhydride (pCA anhydride; 3M DCC, p-coumaric acid solution, DMF as solvent) is added to apo-PYP. The holo-PYP attached with the Chromophore is further purified to remove unwanted proteins or impurities.

2.4.2.2 Purification

Histidine-tags (His-tags) introduced in the PYP sequence were used to purify the PYP. For this, an immobilized metal ion affinity chromatographic column (IMAC) charged with Ni²⁺ resin is used. When PYP solution passes through the column, His-tag PYP are adsorbed to the resin and remain in the column. These His-tag proteins are then displaced by imidazole and are eluted from the column. In order to cleave the His-tags from the PYP, Enterokinase is used. For further purification of PYP, ion exchange chromatography where negatively charged PYP are adsorbed to positively charged gel medium (Q-sepharose GE healthcare) is used. A gradient from zero to 1M NaCl is used to elute PYP depending on its charge. Fast protein liquid chromatography (FPLC, AKTA prime) is used to operate all chromatographic columns involved in the purification process. For long term storage, the purified PYP is flash-frozen in liquid nitrogen.

Glycerol (5%) is added to the purified protein because it prevents ice formations and promotes stability of the protein. All the purification steps are assessed by sodium dodecyl sulfate polyacrylamide gel electrophoresis (SDS-PAGE). For this electrophoresis, proteins samples are denatured by heating and stabilized by addition of an anionic detergent SDS and a reducing agent β -mercaptoethanol. Denatured samples pass through the gel. Upon applying an electric field across the gel, linearized proteins start to move according to their sizes. To visualize the separated bands corresponding to different protein samples, staining and destaining are performed using conventional dyes (Lameelie blue dye).

2.4.2.3 Crystallization

Large crystals of PYP were grown as reported in (Borgstahl *et al.*, 1995). Briefly, crystals are grown with sitting drop vapor diffusion method using a stablization buffer containing 2.7M ammonium sulfate, 50mM sodium phosphate, pH 7.0. PYP of concentration 18~22 mg/mL is used for the crystallization trials. Crystals grow very slowly and they are highly twinned. To obtain high quality crystals and to accelerate their growth, these twinned crystals are used as a seed. To prepare a microseed solution, a few crystals are crushed in the stablization buffer. The micro-seed is added to the protein drops after equilibration at ambient temperature for 2 to 3 days. To add the micro-seeds, a cat whisker is used. Large crystals with typical sizes of $\sim 120 \times 120 \times 700 \mu\text{m}^3$ are then obtained.

2.5 Experimental details to investigate interaction of nitric oxide (NO) with catalase

Two techniques, monochromatic X-ray crystallography and micro-spectrophotometry are used to investigate the interaction of NO with catalase. In the following sections, we will

first describe the details of crystallographic experiments and then those of spectroscopic experiments. The latter experiments are not performed with our newly designed in-house spectrophotometer but with a much slower spectrometer available at BioCars14.

2.5.1 Monochromatic X-ray crystallographic experiments

2.5.1.1 Preparation of different forms of Catalase

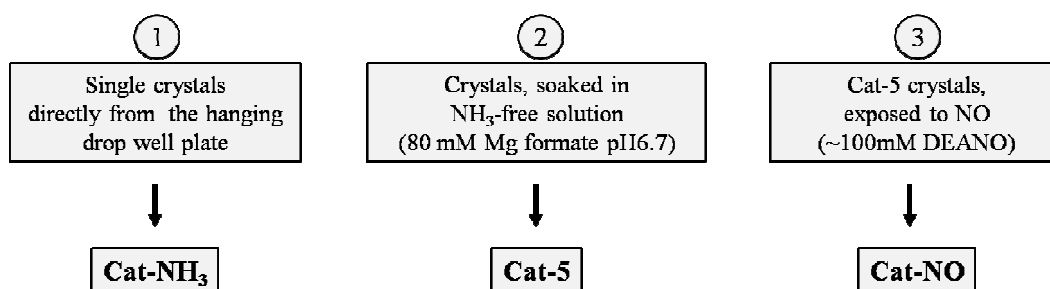


Figure 2.27 Scheme to prepare all three crystal forms of catalase. *Cat-NH₃* crystals are soaked in a NH₃ free solution for 14~16 hours to prepare *Cat-5*. *Cat-5* crystals are then exposed to 100mM DEANO (nitric oxide generator) for the *Cat-NO* form.

Three crystal forms are prepared (Fig. 2.28). Crystals obtained directly from the well plate are termed as Cat-NH₃ because NH₄OH was added into catalase solution as mentioned in the Sec. 2.4.1.2. Consequently, NH₃ binds to the active site. To prepare a second form where the NH₃ is removed, Cat-NH₃ crystals are first soaked overnight in 80 mM magnesium formate solution, pH 6.7 and then washed two more times with the same solution. These crystals are referred as Cat-5 (Fig. 2.28). Since the goal here is to bind nitric oxide (NO) to the Cat-5 crystals, the third form of the crystals is prepared by soaking the Cat-5 crystals with an appropriate NO generator. For this, the crystals are soaked for 5 minutes in a solution containing 80 mM magnesium formate, 150mM Bis-Tris as a buffer and 1-(N,N-diethylamino)diazen-1-ium-1,2-diolate (DEANO, Fig. 2.29A) as a NO generator. The concentration of DEANO was varied from 10 to 200 mM.

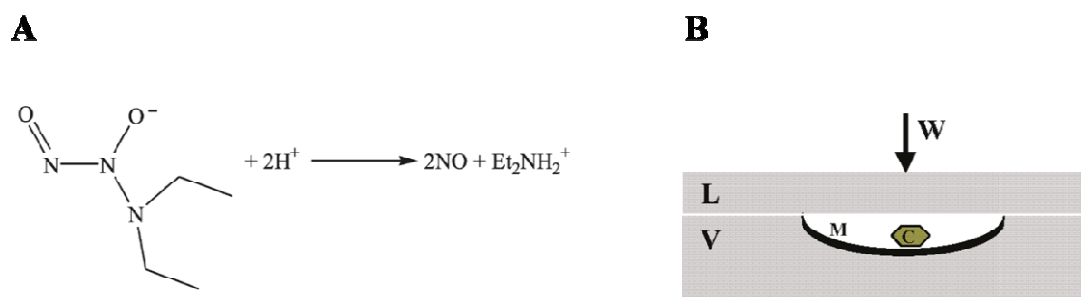


Figure 2.28 A. Molecular structure of DEANO. DEANO decomposes into NO and diethylamine. **B.** A scheme of the apparatus used to generate NO from DEANO. V: glass vessel with a 200 μ l cavity, M: mother liquor, C; Catalase crystal (in green), L: lid of the glass vial, W: Weight kept on the top of lid, L to prevent the escape of NO from the glass vessel V. Figure from Purwar *et al.*, 2011.

The reaction of NO with O₂ generates acidic products (Cotton *et al.*, 1999). This can cause a pH shift, which can be avoided by immersing these crystals in a well buffered solution. To minimize the escape of NO into the atmosphere during the crystal nitrosylation process, a simple device is used. As shown in the Fig. 2.29B, this apparatus consists of two glass plates with the mating surfaces ground to provide a very tight seal. The glass vessel V has a hemispherical depression with a capacity of ~ 200 μ L. A Cat-5 crystal is placed in the depression, which is then filled with the stabilization buffer/DEANO mixture. The depression is quickly covered with the top lid L so that NO escape can be prevented. A heavy weight was placed on the top of upper plate to maintain high internal pressure. Thus obtained crystals are termed as Cat-NO (Fig. 2.28).

2.5.1.2 Data collection

All three crystal forms are soaked in a cryoprotectant consisting of 20% polyethylene glycol 4000, 20% sucrose, 50mM Tris, pH 8.5. For the Cat-NO crystals, it is imperative to quickly remove the crystals from the pressure cell and immediately freeze them in the cryojet because NO starts to diffuse out of the crystals as soon as the pressure are

released. NO occupancy at the active site drops to an undetectable level within ~10 minutes unless the crystal is frozen. For all three crystal forms (Cat-NH₃, Cat-5 and Cat-NO), data sets are collected at cryogenic temperatures. Mosaicity of these crystal forms is estimated prior to the actual data collection. The crystals are rotated through 180° in steps of 0.5° to cover the reciprocal space for a complete data set.

2.5.1.3 Data analysis

Data sets for the crystal forms Cat-NH₃, Cat-5 and Cat-NO are reduced with Mosflm (Sec. 2.1.17). Reflection intensities are scaled and merged with SCALA. From these intensities, structure factor amplitudes are calculated using TRUNCATE. The three dimensional crystal structure of beef liver Catalase is already solved for the orthorhombic crystal form and available as a PDB entry 4BLC (Ko *et al.*, 1999). Therefore, molecular replacement is not required in this case, and the model 4BLC is used directly as an initial model. To prepare a basic starting model, all the water molecules and the cofactors (nicotinamide adenine dinucleotide phosphate, reduced NADPH) are removed from the model. This model is refined using rigid body refinement at 3Å. After that, simulated annealing refinement using a 2000K protocol up to full resolution is performed. Positional conventional refinement is performed until convergence. B-factors are refined using a 40-step restrained B-factor refinement. Water molecules are searched up to 3σ level in the difference electron density map ($F_{\text{obs}} - F_{\text{calc}}$) and added to the structure. Some of the waters are found in cavities. These cavities are determined with the program 'voidoo' (Kleywegt & Jones, 1994) using a probe with radius 1.4 Å on a 0.5 Å grid.

2.5.1.4 Insertion of small molecules such as NH_3 or NO

The active site heme and its vicinity are examined for the presence of any putative molecule. If a positive feature is identified in the difference map ($F_{\text{obs}} - F_{\text{calc}}$), it can be interpreted as NH_3 or NO, depending on how the crystal was treated. The occupancy of the ligand is roughly estimated by calculating the total number of electrons in the positive feature. For that, the positive electron density feature is integrated using the program *Probe* (Srajer *et al.*, 2001). The electron count is less than 10 for Cat- NH_3 form and less than 15 for Cat-NO form. Therefore, it is necessary to determine the exact occupancy of the ligand in each crystal form. For that, the nitrogen atom of either ligands, NH_3 or NO, is connected to the heme iron at a fixed distance using a very weak bond length restraint. NO is also aligned into a particular orientation with weak angular restraints which is not applicable for the Cat- NH_3 . Refinement commences using the grouped occupational refinement option in CNS. Then, positional conventional refinement is performed to refine the position and orientation of these ligands.

2.5.1.5 B-factor averaging

For the Cat-NO, B-factors are determined for the nitrogen and the oxygen atoms of the NO. B-factors for these two atoms as well as for the iron and the four nitrogen atoms of the heme are averaged (Fig. 2.30B). The average B-factor is then assigned to both N and O. Similarly, an average B-factor is obtained for NH_3 . The obtained B-factors are refined with restrained B-factor refinement and then conventional positional refinement is performed. Both of these refinements are repeated until convergence is reached.

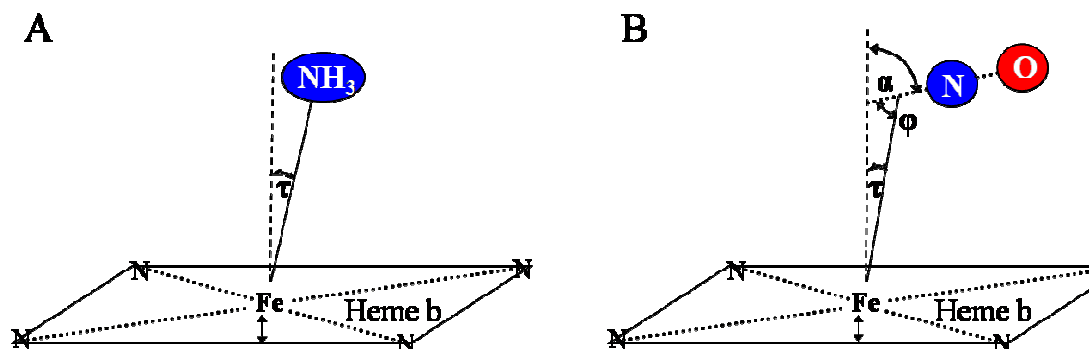


Figure 2.29 Tilt (τ), bending (ϕ) and tilt+bend (α) angles for two different ligands with respect to the heme plane. The plane is defined by the four porphyrin nitrogens. A double headed arrow marks potential iron out of plane displacements. **A.** NH₃ (Blue ellipse) is bound to the heme iron in Cat-NH₃. **B.** NO (blue sphere: N, red sphere: O) is bound to the heme iron. Panel B from Purwar *et al.*, 2011.

2.5.1.6 Geometry of the ligand molecule

To describe the orientation of the ligand molecule, the tilt (τ) angle, the bend angle (ϕ) and their sum (α) with respect to a given plane can be used (Fig. 2.30). Two ligands NH₃ and NO are bound to the catalase. The ligand NH₃ consists of a single atom (ignoring hydrogen atoms). For NH₃, only the tilt angle with respect to normal of the heme plane can be determined where heme plane is defined by the four porphyrin nitrogens (Fig. 2.30A). For NO, all angles τ , ϕ and α with respect to the heme plane can be calculated (Fig. 2.30B). The iron out of plane distance can be calculated using Planefit (Tab. 3.1) (Nienhaus *et al.*, 2005).

2.5.2 Micro-spectrophotometric experiments (performed at BioCARS)

2.5.2.1 Data collection and analysis

A microspectrophotometer (4DX) equipped with a Deuterium/Tungsten light source (DH2000, Ocean Optics) and a USB mini-spectrometer (USB 2000, Ocean Optics) is mounted in line with the X-ray beam at BioCARS 14BM-C. The spectroscopic

experiments for the three crystal forms, Cat-NH₃, Cat-5 and Cat-NO are performed at 100 K. The absorption spectra, $A(\lambda)_{\Delta t}$ of all species are recorded for up to 10 minutes in intervals of 10 s during X-ray exposure. Subsequent exposure times can be written as 10s, 20s, 30s.....600s. Difference spectra, $\Delta A(\lambda)_{\Delta t}$ are generated by subtracting the $A(\lambda)_{\Delta t}$ from the reference spectrum, $A(\lambda)_D$ recorded before X-ray exposure. Absolute differences are integrated from wavelength 500 to 700 nm for each exposure time. They are denoted as $\Delta A_{\text{int}}(t)$ and plotted against exposure time. Data are fitted empirically either by a single exponential, a sum of two exponentials or by an exponential and a linear phase.

2.6 Experimental details to investigate the kinetic dose limit in PYP

2.6.1 Data collection

Two PYP crystals of dimensions 170 x 170 x 700 μm^3 (PYP1) and 150 x 150 x 900 μm^3 (PYP2) are equilibrated at pH 7 and mounted individually in a capillary as described in sec. 2.2.9. The crystal PYP1 is used for actual experiment and PYP2 for a control experiment (Schmidt *et al.*, 2012). The time-resolved technique is described extensively in sec. 2.2.10 and all the variables are defined in Sec. 2.2.11. Here we report some details specific to this experiment. Four X-rays exposures ($N_p = 4$) are accumulated per diffraction pattern. The slower part of the PYP photocycle (Fig. 1.4) is selected to investigate radiation damage. A time range from 256 μs to 32 ms is used. A short time-series, containing $N_t = 8$ time delays (256 μs , 512 μs , 1 ms, 2 ms, 4 ms, 8 ms, 16 ms and 32 ms) and one dark exposure, is obtained. $N_o = 20$ different crystal orientations are used. Between subsequent orientations, the crystal is translated by 22 μm and therefore

total crystal translation is 440 μm (Fig. 2.31B & Fig. 2.14B). The entire experiment is repeated 12 times and corresponding 12 short time-series are obtained (Fig. 3.3A). As a control experiment, crystal PYP2 is used to examine the damage due to laser pulses. The same protocol as described above is used without exposure to X-rays. The experiment is repeated 16 times which are equivalent to 16 virtual time-series. During these 16 time-series, 5 dark exposures are collected at equal intervals. The crystal is exposed to 512 laser pulses per orientation. A total of 10240 laser pulses are accumulated during the entire control experiment.

2.6.2 Absorbed dose calculation

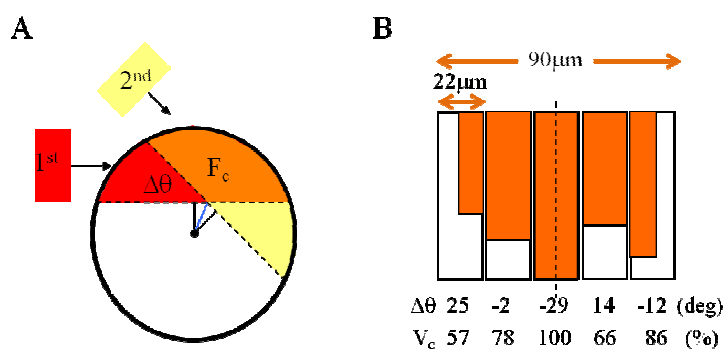


Figure 2.30 A model used to determine the common area F_c . X-ray beam falls on the PYP crystal. As the crystal is re-oriented by $\Delta\theta$, it is irradiated from one direction (red rectangle) to another direction (yellow rectangle). **A.** The common area (colored orange) is F_c which is used to calculate the common volume V_c (not shown). **B.** A sequence of angular settings, $\Delta\theta$, (in degrees). These settings are also separated by translations of 22 μm . Five settings are fully or partially exposed with the employed X-ray beam. The orange bars denote the relative sizes of the V_c for each angular setting. Figure from Schmidt et al., 2012.

Since the goal is to find out how many data sets can safely be collected without extensive damage, the energy deposited in the crystal due to the ionizing radiation must be determined. To calculate the absorbed dose in $\text{Joule/kg} = \text{Gy}$, the program ‘Raddose’ (Murray et al., 2004) is used. If the crystal PYP1 is irradiated by a single X-ray pulse of

90 (h) \times 60 (v) μm^2 , the illuminated voxel is equal to beam size times the crystal thickness ($t = 170 \mu\text{m}$). The dose absorbed by the illuminated voxel, d_{vox} , is calculated. If l_{eff} is length of the crystal that is exposed to X-ray beam, the total irradiated crystal volume is $l_{eff} \times v \times t \mu\text{m}^3$. The sum of overall crystal translation in 20 orientations (440 μm) and X-ray beam size in the horizontal direction (90 μm) provides a l_{eff} of 530 μm (Fig. 2.14B). The dose absorbed by this crystal volume (d_{crys}) due to each single X-ray pulse is computed as

$$d_{crys} = \frac{h \times v \times t}{l_{eff} \times v \times t} d_{vox} = \frac{h}{l_{eff}} d_{vox} \quad (2.28)$$

Each short time-series consists of 8 time delays, one dark exposure and one exposure due to edge scan (Sec. 2.2.10). If 20 crystal orientations and 4 X-ray pulses per diffraction are taken into account, the average dose absorbed in one comprehensive time series, d_{ts} , can be written as

$$d_{ts} = d_{crys} \times (N_t + 2) \times N_o \times N_p \quad (2.29)$$

where N_t , N_o and N_p are defined in Sec. 2.2.11. In order to determine the total dose (D_{nc}) during the entire experiment, the dose for one time-series is multiplied by the total number of collected time-series. The intensity values are used to address radiation damage. The steps involved in the determination of intensities from the raw Laue diffraction pattern are described in Sec. 2.2.12-13 & Fig. 2.15A. $\langle I \rangle$ and $\langle I/\sigma_I \rangle$ are plotted as a function of uncorrected dose D_{nc} (Fig.3.3A). Two types of correction are required. The first correction is due to the subsequent crystal settings. Since the thickness of the crystal (t) is larger than the vertical X-ray beam size (v), each time when the crystal is rotated by an angle, $\Delta\theta$, from one orientation (in red) to another (in yellow), some fresh

crystal volume is exposed (Fig. 2.31A). As a result, the dose deposited into the given crystal volume is decreased. To calculate the correction term, the common area F_c and the common volume V_c between two consecutive crystal settings can be determined (Fig. 2.31). If the size of X-ray beam $h = 90 \mu\text{m}$ is divided by the translation step in each setting ($22\mu\text{m}$), five crystal settings are affected as shown in Fig. 2.31B. Among these 5 settings, three are covered fully by the X-ray beam while two are covered partially. The V_c for each of the five neighboring settings are calculated and averaged (Fig. 2.31B). The average volume, $\langle V_c \rangle$ is the first correction term for the absorbed X-ray dose for all the short time-series (Fig. 2.31B). The second type of correction is required due to the edge scan method. Edge scan is performed once at the beginning of each crystal setting. After each edge scan, the x and y coordinates of the goniometer are recorded. The relative vertical displacements, y' , of the crystal across the X-ray beam for each setting can be calculated (Fig. 2.31). The individual y' are averaged to obtain $\langle y' \rangle$. The crystal displacement about $\langle y' \rangle$ exposes a fresh crystal volume to the beam that further reduces the deposited dose. Using $\langle y' \rangle$, the dose can be corrected for each sweep. In addition, the crystal damage due to laser pulses during the entire experiment must be determined and corrected. Since the crystal is exposed to only laser pulses without exposing to the X-ray pulses, these laser pulses can be assumed equivalent to virtual X-ray doses. Once the virtual dose is calculated, corrections due to different crystal orientations and due to the edge scan can be applied to the virtual data as described for X-ray exposure. The adjusted virtual dose corresponding to each of the 16 virtual time-series D_L is obtained. $\langle I \rangle$ and $\langle I/\sigma_I \rangle$ corresponding to all five dark data sets are plotted as a function of adjusted virtual dose, D_L (Fig. 3.3B). The intensities and their standard deviations both are fitted with

straight lines. The y-intercept at zero absorbed-dose is normalized to unity and then the slope (S_L) is determined. Assuming that the damage due to the laser pulses and X-ray pulses are independent events, the intensities $\langle I \rangle$ corresponding to all 12 time series, for which X-ray as well as laser exposures are used, are corrected for the laser damage (Fig. 3.3B). The Intensities free from the laser damage $\langle I \rangle_{\text{free}}$ are given by

$$\langle I \rangle_{\text{free}} = \langle I \rangle (-S_L D_{\text{corr}} + 1) \quad (2.30)$$

2.6.3 SVD analysis

For all the 12 time-series, difference structure factor amplitudes are calculated as reported (Sec. 2.2.14)(Ren *et al.*, 2001, Ihee *et al.*, 2005). PDB (Berman *et al.*, 2002) entry 2PHY is used to provide phases to calculate time-dependent difference maps. A total of 96 difference maps are obtained corresponding to 12 time-series. Each of these time-series is analyzed by SVD (Schmidt *et al.*, 2003, Zhao & Schmidt, 2009). The difference electron density at the chromophore region is included in analysis (sec. 2.2.16). Grid points including the chromophore as well as the amino acid residues that line the chromophore pocket such as Tyr-42, Glu-46, Met-100 and Arg-52 are masked out (Schmidt *et al.*, 2012). The mask is evolved by allowing only grid points that are above $+2.5\sigma$ or below -2.5σ in at least one of the difference maps of the time-series. The SVD is performed on the masked difference maps and right singular vectors (rSVs) are obtained (Fig. 3.4). From the fitted rSVs, relaxation times are extracted. The kinetic mechanism shown in Fig. 2.18A is used for the Posterior analysis. If no rising phase is detected in the rSVs, the mechanism used for the analysis is given in the dashed box of

Fig. 2.18A. Once microscopic rate coefficients k_i are obtained, their inverse relaxation times (τ_{post}) can be calculated (Fig. 3.6A).

2.7 Experimental details to investigate the pH dependence of PYP photocycle

2.7.1 Data Collection

PYP crystals of size $\sim 100 \times 100 \times 700 \mu\text{m}^3$ are soaked for 5 minutes in stabilization buffer (2.7M Ammonium sulfate, 50mM Sodium phosphate) adjusted to pH 4, 7 and 9 (Tripathi *et al.*, 2012). The crystals are mounted in capillaries (Sec. 2.2.9 & Fig. 2.14A) and equilibrated for at least 12 hours in the respective buffer before data collection. The diffraction experiments for all three pH conditions are performed at 25 °C. The slower part of the photocycle is selected for the time-resolved investigation. At pH 4 a time range from 4 μs to 1 sec is employed and distributed through 18 time points (N_t). At pH 7 eighteen time delays are collected in the range from 1 μs to 512 ms, whereas at pH 9 twenty time delays are collected from 1 μs to 1 s. A comprehensive time-series, consisting of N_t time delays and one dark exposure without any laser illumination, is collected for each pH condition. To recover the dark state, the waiting time between two consecutive laser pulses is 30 s, 4 s and 12 s at pH 4, 7, and 9, respectively. Twenty different crystal orientations ($N_o = 20$) are used. X-ray pulses (N_p) accumulated per diffraction pattern are 3, 11 and 9 in the case of pH 4, 7 and 9, respectively. The edge scan is used to maximize the overlap of laser and X-ray illuminated volume (Sec. 2.2.10 & Fig. 2.14B). The time-resolved Laue data sets are processed by Precognition/Epinorm as described in Sec. 2.2.12-13. Phases are determined from PDB entry 2PHY. Difference electron density maps on the absolute scale are calculated. The difference electron

density of the chromophore region is used for the SVD analysis. From rSVs, relaxation times (τ_1 & τ_2) are calculated as described in Sec. 2.2.16.

2.7.2 Kinetic analysis

For the posterior analysis (Schmidt, 2008), the kinetic model shown in Fig. 2.18B is used. The rate coefficients, k_i of the mechanism are refined against observed electron density maps and concentration profiles are determined. Once k_i 's are known, the corresponding relaxation times (τ_p) can be calculated.

2.7.3 Extrapolated maps

The difference maps corresponding to the time points $t_i < \tau_1$ contain structural information about the pR intermediates, while those time points $\tau_1 < t_i < \tau_2$ contain information about pB. The maps in the respective pR and pB regions are averaged (Tripathi *et al.*, 2012). Fourier inversion of these average maps provide time-independent difference structure factors (ΔF_{tind}) for both pR and pB. Extrapolated structure factors F_{tind}^{ext} are then calculated as given by

$$F_{tind}^{ext} = F_d^{calc} + N\Delta F_{tind} \quad (2.29)$$

where F_d^{calc} is structure factor of the dark state model and N is the multiplication factor. N has to be determined such that it compensate the missing scale between ΔF_{tind} and F_d^{calc} . To do that, we start with N=1 and corresponding F_{tind}^{ext} are calculated. From these F_{tind}^{ext} , extrapolated electron density maps are obtained. The negative electron density features in these extrapolated maps are integrated. The factor N is increased and the above steps are repeated. Once N reaches up to a certain characteristic N_c , the procedure is stopped because after N_c large negative features start to appear in the extrapolated

maps. Using the N_c and respective F_{tind}^{ext} , conventional extrapolated electron density maps are obtained (Schmidt *et al.*, 2004, Tripathi *et al.*, 2012). The structural models for pR and pB are interpreted into the extrapolated difference maps and their atomic models are refined against the $|F_{tind}^{ext}|$ using CNS (Sec. 2.1.18). The improved model phases (ϕ_{new}) are combined with the $|\Delta F_{tind}|$ to calculate new extrapolated structure factors and also new extrapolated maps.

2.8 Experimental details to investigate the temperature dependence of the PYP photocycle

The effect of temperature on the structure and kinetics of the PYP photocycle is investigated using two techniques: time-resolved crystallography and time-resolved spectroscopy. In the first few sections, experimental details related with crystallography are described. Spectroscopic experimental details are described in the later sections.

2.8.1 Time-resolved crystallography

2.8.1.1 Data collection

PYP crystals of typical sizes $100 \times 100 \times 700 \mu\text{m}^3$ are mounted in capillaries as described in Sec. 2.2.9 (Fig. 2.14A). Diffraction experiments are performed at 14 different temperatures. The temperature is varied from -40°C to 70°C . For experiments above 30°C , the capillaries must be insulated from the brass pins as shown in Fig. 2.32A. Otherwise severe distillation effects due to the cold brass pin dry out the crystals.

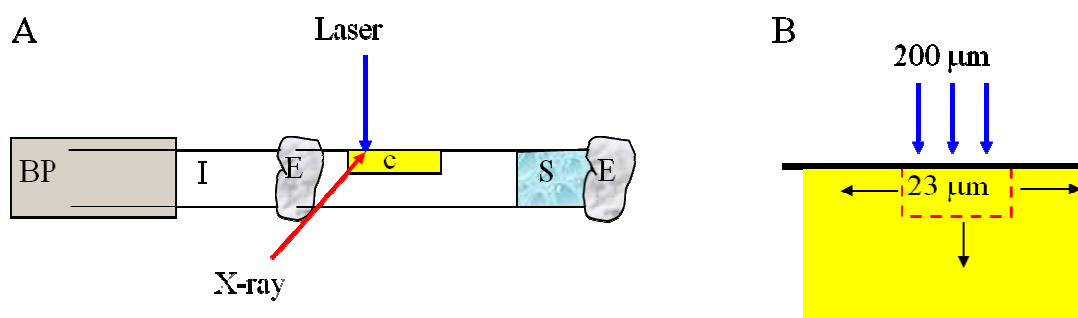


Figure 2.31 **A.** Protein sample mounted in the capillary for $T > 30\text{ }^{\circ}\text{C}$. *P*: brass pin, *I*: insulating glass capillary, *E*: epoxy glue, *c*: PYP crystal (colored yellow), *S*: stabilizing solution. **B.** Laser illuminated volume of the crystal (red dashed box). Capillary wall (thick black line) is temperature controlled. Black arrows show the directions of heat diffusion. Figure from Schmidt et. al., 2013.

For temperature up to $40\text{ }^{\circ}\text{C}$ time delays range from 2 ns to several seconds whereas for temperatures equal to or higher than $50\text{ }^{\circ}\text{C}$, the time delays start at 100ns (Tab. 2.1). The waiting time between two subsequent laser pulses is varied from 1 s at higher temperatures to 20 s at lower temperatures (Tab. 2.1). Twenty different crystal orientations (N_o) are used. For the data collection, edge scan is used as described before. Data collected at all temperatures are processed with Precognition/Epinorm (Sec. 2.2.12-13). Weighted difference structure factor amplitudes are calculated (Sec. 2.2.14). With these amplitudes and phases from the PDB entry 2phy, time-dependent difference maps ($\Delta\rho^{\text{obs}}$) are calculated.

2.8.1.2 Kinetic analysis

SVD analysis is performed using the difference electron density maps. Relaxation times () and their inverse relaxation rates are obtained for each of the 14 temperature settings from the rSVs as described in Sec.2.2.16. The observed relaxation rates are plotted as a function of temperature and fitted by the Van't Hoff-Arrhenius

equation (Eq. 1.4). From the fitting, prefactor ν and activation energy E_a are calculated for the relaxation rates Λ_2 , Λ_3 & Λ_4 .

Table 2.1 Data collection statistics of PYP at different temperatures. Table from Schmidt *et al.*, 2013.

T _{jet} (°C)	T diode [K]	N _p (time points)	time range	wait time ^a	completeness (last shell)	I/ σ_I (last shell)	R _{merg} ^e (%) ^b	R _{scale} (%) @ Δt^c	$\Delta\rho_{\min}/\sigma_{\Delta\rho}$ $\Delta\rho_{\max}/\sigma_{\Delta\rho}$ @ Δt
-40	235.5	31	2 ns to 15 s	20 s	82.5 (75.9)	16.9 (11.0)	8.3	7.7 (3 μ s)	-6/+10 (3 μ s)
-30	245.1	27	1 ns to 4 s	12 s	77.3 (73.4)	28.3 (21.8)	5.3	6.8 (2 μ s)	-11/+13 (2 μ s)
-20	254.7	34	2 ns to 8 s	12 s	82.7 (78.2)	29.3 (21.4)	4.9	5.4 (4 μ s)	-11/+11 (4 μ s)
-15	259.5	29	2 ns to 8 s	10 s	88.0 (82.3)	23.0 (18.5)	6.8	6.9 (4 μ s)	-7/+9 (4 μ s)
-10	264.3	23	4 ns to 8 s	10 s	71.5 (66.2)	27.4 (24.8)	5.0	4.8 (4 μ s)	-9/+11 (4 μ s)
0	274.0	27	8 ns to 512 ms	10 s	75.1 (68.0)	27.1 (18.8)	5.4	5.7 (4 μ s)	-9/+9 (4 μ s)
10	283.6	27	2 ns to 128 ms	4 s	82.2 (77.8)	30.3 (26.9)	5.2	3.9 (4 μ s)	-10/+11 (4 μ s)
20	293.2	27	2 ns to 128 ms	4 s	81.7 (75.3)	20.1 (14.9)	6.8	6.9 (4 μ s)	-7/+7 (4 μ s)
25	293.7	27	2 ns to 512 ms	2 s	78.3 (73.4)	25.5 (20.0)	5.3	5.2 (4 μ s)	-11/+12 (4 μ s)
30	298.5	27	2 ns to 128 ms	2 s	83.5(75.9)	25.3 (16.1)	5.6	6.8 (4 μ s)	-11/+10 (4 μ s)
40	308.9	24	2 ns to 64 ms	2 s	84.7 (80.3)	30.6 (21.7)	4.7	7.1 (4 μ s)	-9/+10 (4 μ s)
50	318.9	22	100 ns to 256 ms	4 s	77.0 (73.0)	31.3 (24.8)	4.6	4.8 (4 μ s)	-9/+9 (4 μ s)
60	328.8	24	100 ns to 1 s	4 s	84.5 (79.3)	30.0 (18.1)	4.8	5.6 (2 μ s)	-8/+9 (2 μ s)
70	338.8	21	100 ns to 1 s	4 s	84.6 (80.3)	30.6 (21.7)	4.7	4.4 (800 ns)	-6/+6 (800 ns)

^a Waiting time between two subsequent laser pulses ^b $R_{\text{merge}} = \left[\sum_{hkl} \sum_j |I_{hkl,j} - \langle I_{hkl} \rangle| \right] / \left[\sum_{hkl} \sum_j I_{hkl,j} \right]$ ^c $R_{\text{scale}} = \left[\sum_{hkl} |F_{hkl}^{\Delta t} - F_{hkl}^D| \right] / \sum_{hkl} F_{hkl}^D$

2.8.2 Time-resolved spectroscopy

2.8.2.1 Data collection: PYP in solution

A 400 nL drop of protein concentration 2-3 mg/mL is mounted as described in the Sec.

2.3.5. A time series of 10 time delays starting from 30 μ s to 2 s at T = 22 °C is obtained.

The waiting time between two consecutive laser pulses is 5 s. The accumulations numbers and pulse widths are set for each time delay (Tab. 2.2).

2.8.2.2 Data collection: Crushed single PYP crystal

A crystal of size $\sim 200 \times 200 \times 200 \mu\text{m}^3$ is crushed between two cover slides as described in the Sec. 2.3.6. Data sets at two different temperatures 30°C and 0°C are collected. At 30°C 24 time points covering the range from $25 \mu\text{s}$ to 2 s are obtained. Waiting time between two subsequent laser pulses is 5 sec. At 0°C , a time range from $25 \mu\text{s}$ to 3s is covered by 34 time delays. Waiting time between two subsequent laser pulses is 10 s. For both temperatures, the accumulation numbers and pulse widths are different depending on the time delay (Tab. 2.2). The slower part of the photocycle is selected for all spectroscopic experiments as in the pH and dose experiments. Reaction initiation is achieved with $380 \mu\text{J}$ of a 6 ns laser pulse at 446 nm.

Table 2.2 Data collection parameters assigned to different time delays for time-resolved spectroscopic experiments.

Time delay (range)	Pulse width	Accumulation
25 μs - 80 μs	20	45
81 μs - 200 μs	40	20
201 μs - 1ms	60	20
1ms - 500ms	100	20
501ms - 3s	170	20

2.8.2.3 Data Analysis

Difference absorption spectra are obtained for solution (Fig. 3.12A) and crushed crystal (Fig. 3.13A-B) using the data analysis program described in Sec. 2.3.12. Spectral changes in the wavelength range from 400 to 520 nm are selected for the SVD analysis. rSVs obtained from these analysis are inspected for the presence of kinetic phases (Fig. 3.12B

& Fig. 3.13C-D). Relaxation times obtained from crushed crystal are compared at different temperatures to examine the effect of temperature on the photocycle.

References

- Amorós, J. L., Buerger, M. J. & Amorós, M. C. (1975). *Academic Press. New York*, 375.
- Berman, H. M., Battistuz, T., Bhat, T. N., Bluhm, W. F., Bourne, P. E., Burkhardt, K., Feng, Z., Gilliland, G. L., Iype, L., Jain, S., Fagan, P., Marvin, J., Padilla, D., Ravichandran, V., Schneider, B., Thanki, N., Weissig, H., Westbrook, J. D. & Zardecki, C. (2002). *Acta crystallographica. Section D, Biological crystallography* **58**, 899-907.
- Borgstahl, G. E., Williams, D. R. & Getzoff, E. D. (1995). *Biochemistry* **34**, 6278-6287.
- Bruenger, A. T., Adams, P. D., Clore, G. M., Delano, W. L., Gros, P., Gross-Kunstleve, R. W., Jiang, J. S., Kuszewski, J., Nilges, M., Pannu, N. S., Read, R. J., Rice, L. M., Simonson, T. & Warren, G. L. (1988). *Acta Cryst. D* **54**, 905-921.
- CCP4, N. C. C. P. (1994). *Acta Crystallog. sect. D*, **50**, 760-763.
- Cotton, F. A., Wilkinson, G., Murillo, C. A. & Bochmann, M. (1999). 6th ed., pp. 309-379. New York, NY: John Wiley and Sons, Inc.
- Cruickshank, D. W. J., Helliwell, J. R. & Moffat, K. (1987). *Acta Crystallographica Section A: Foundations of Crystallography* **43**, 18.
- Cruickshank, D. W. J., JR T. Helliwell & Moffat., a. K. (1991). *Acta Crystallographica Section A: Foundations of Crystallography* **47**, 21.
- Drenth, J. (1999). *Principles of protein x-ray crystallography*, 2nd ed. New York: Springer.
- Evans, P. (2006). *Acta Cryst. D Biol. Cryst* **62**, 72-82.
- Graber, T., Anderson, S., Brewer, H., Chen, Y. S., Cho, H. S., Dashdorj, N., Henning, R. W., Kosheleva, I., Macha, G., Meron, M., Pahl, R., Ren, Z., Ruan, S., Schotte, F., Srajer, V., Viccaro, P. J., Westferro, F., Anfinrud, P. & Moffat, K. (2011). *J Synchrotron Radiat* **18**, 658-670.
- Ihee, H., Rajagopal, S., Srajer, V., Pahl, R., Anderson, S., Schmidt, M., Schotte, F., Anfinrud, P. A., Wulff, M. & Moffat, K. (2005). *Proceedings of the National Academy of Sciences of the United States of America* **102**, 7145-7150.
- Ko, T. P., Day, J., Malkin, A. J. & McPherson, A. (1999). *Acta Cryst. D* **55**, 1383-1394.
- Leslie, A. G. (2006). *Acta Cryst. D* **62**, 48-57.
- McRee, D. E. (1999). *J. Struct. Biol.* **125**, 156-165.
- Murray, J. W., Garman, E. F. & Ravelli, R. B. G. (2004). *J Appl Crystallogr* **37**, 513-522.
- Nienhaus, K., Ostermann, A., Nienhaus, G. U., Parak, F. G. & Schmidt, M. (2005). *Biochemistry* **44**, 5095-5105.
- Otwinowski, Z. & Minor, W. (1997). *Methods enzymol*, **276**, 307-326.
- Purwar, N.**, Tenboer, J., Tripathi, S. & Schmidt, M. (2013). *International journal of molecular sciences* **14**, 18881-18898.
- Reid, T. J., Murthy, M. R. N., Sicignano, A., Tanaka, N., Musick, W. D. L. & Rossmann, M. G. (1981). *Proc. Natl. Acad. Sci. USA* **78**, 4767-4771.

- Ren, Z., Bourgeois, D., Helliwell, J. R., Moffat, K., Srajer, V., & Stoddard, B. L. (1999). *Journal of Synchrotron Radiation*, **6**, 26.
- Ren, Z. & Moffat, K. (1995). *J Appl Crystallogr* **28**, 461-481.
- Ren, Z. & Moffat, K. (1995). *J Appl Crystallogr* **28**, 22.
- Ren, Z., Perman, B., Srajer, V., Teng, T. Y., Pradervand, C., Bourgeois, D., Schotte, F., Ursby, T., Kort, R., Wulff, M. & Moffat, K. (2001). *Biochemistry* **40**, 13788-13801.
- Rupp, B. (2010). *Biomolecular crystallography : principles, practice, and application to structural biology*. New York: Garland Science.
- Schmidt, M. (2008). *Ultrashort Laser Pulses in Medicine and Biology*, edited by W. Zinth, Braun, M., Gilch, P., pp. 201-241. Heidelberg, New York: Springer Verlag.
- Schmidt, M., Graber, T., Henning, R. & Srajer, V. (2010). *Acta crystallographica. Section A, Foundations of crystallography* **66**, 198-206.
- Schmidt, M., Ihee, H., Pahl, R. & Srajer, V. (2005a). *Methods Mol Biol* **305**, 115-154.
- Schmidt, M., Pahl, R., Srajer, V., Anderson, S., Ren, Z., Ihee, H., Rajagopal, S. & Moffat, K. (2004). *Proceedings of the National Academy of Sciences of the United States of America* **101**, 4799-4804.
- Schmidt, M., Rajagopal, S., Ren, Z. & Moffat, K. (2003). *Biophysical journal* **84**, 2112-2129.
- Schmidt, M., Srajer, V., **Purwar, N.** & Tripathi, S. (2012). *J Synchrotron Radiat* **19**, 264-273.
- Srajer, V., Crosson, S., Schmidt, M., Key, J., Schotte, F., Anderson, S., Perman, B., Ren, Z., Teng, T. Y., Bourgeois, D., Wulff, M. & Moffat, K. (2000). *J Synchrotron Radiat* **7**, 236-244.
- Srajer, V., Ren, Z., Teng, T. Y., Schmidt, M., Ursby, T., Bourgeois, D., Pradervand, C., Schildkamp, W., Wulff, M. & Moffat, K. (2001). *Biochemistry* **40**, 13802-13815.
- Tripathi, S., Srajer, V., **Purwar, N.**, Henning, R. & Schmidt, M. (2012). *Biophysical journal* **102**, 325-332.
- van Stokkum, I. H., Larsen, D. S. & van Grondelle, R. (2004). *Biochimica et biophysica acta* **1657**, 82-104.
- Zhao, Y. & Schmidt, M. (2009). *J Appl Crystallogr* **42**, 734-740.

3 Results

3.1 Interaction of Nitric Oxide (NO) with Catalase: X-ray crystallographic analysis

3.1.1 Crystal structures

All three crystals forms obtained are orthorhombic with space group $P2_12_12_1$. The unit cell dimensions vary slightly depending on the crystal form, in the range of $a = 83 \sim 86$ Å, $b = 139 \sim 140$ Å, $c = 228 \sim 229$ Å and $\alpha = \beta = \gamma = 90^\circ$ (Tab. 3.1). Multiple datasets are collected for each crystal form and the best one is picked based on high resolution, low degree of mosaicity, low R_{sym} values and high completeness. For these data sets, typical resolution extends to 1.9 Å and mosaicity is about $\sim 0.3^\circ$. Data completeness is more than 90% with an $R_{\text{sym}} < 10\%$. I/σ_I value found in the last resolution cell is 2.5.

Table 3.1 Data collection statistics for the three crystal forms of the catalase. Table from Purwar et al., 2011.

Dataset	CAT-NH ₃	CAT-5	CAT-NO
Soaking	Directly from hanging drop	14 hours NH ₃ -free buffer	5 minutes 100 mM DEANO
a (Å)	83.48	83.22	86.11
b (Å)	140.72	140.92	139.94
c (Å)	229.52	229.37	228.02
$\alpha = \beta = \gamma$ (deg)	90	90	90
Spacegroup	$P2_12_12_1$	$P2_12_12_1$	$P2_12_12_1$
Unit cell volume(Å ³)	2696241	2689905	2747694
Resolution(Å)	1.99	1.90	1.88
R_{sym} (last shell)	9.4(30.3)	8.9(34.3)	9.1(32.9)
Completeness (last shell) (%)	92.8(92.8)	97.9(97.1)	92.2(89.9)
Redundancy (last shell)	5.7(5.5)	3.6 (3.3)	5.1 (4.3)
I/σ_I (last shell)	5.0(2.5)	5.1(2.5)	5.6(2.1)
$R_{\text{crys}}/R_{\text{free}}$ no water (%)	23.68/27.05	24.1/26.9	24.05/27.05
Water molecules	2126	1277	2013
$R_{\text{crys}}/R_{\text{free}}$ with water (%)	16.83/20.69	22.16/25.82	18.56/22.05

rmsd bond length ^a	0.006	0.007	0.006
rmsd bond angle (deg)	1.3	1.3	1.3
Ramachandran outliers	53 (2.9%)	62 (3.3%)	53 (2.9%)
Occupation from electron count (%)			
Heme A	70	6.0	51
Heme B	71	3.7	40
Heme C	82	1.4	35
Heme D	95	1.7	74
	80±10	3.2±1.8	50±11
Refined Occupancy (%)			
Heme A	82		55
Heme B	100		52
Heme C	77		45
Heme D	101		61
	90±12.3		53.3±5.8
FE out of plane distance (Å)			
Heme A	0.063	0.014	0.016
Heme B	-0.054	0.123	-0.035
Heme C	-0.044	0.132	-0.020
Heme D	-0.052	-0.005	0.019
	-0.02±0.06	0.066±0.07	-0.020±0.027
tilt angle (τ) / bend angle (φ) / tilt+bend angle (α) (deg)			
Heme A	7.98		9.14/19.6/28.74
Heme B	6.01		8.17/5.03/3.13
Heme C	0.51		12.28/11.78/24.06
Heme D	5.33		8.23/9.72/17.96
	5.0±2.75		9.46±1.68/11.53±5.6/ 18.47±9.65
RMS coordinate error (Å)			
	0.181	0.262	0.214
Iron-Nitrogen distance (Å)			
Heme A	2.10		1.92
Heme B	2.11		1.88
Heme C	2.11		1.85
Heme D	2.10		1.83
	2.105±0.01		1.87±0.034
Nitrogen (NH3) –Water/ Oxygen (NO) -Water (Å)			
Heme A	3.05		2.42
Heme B	3.05		2.69
Heme C	2.96		2.58
Heme D	2.76		2.52

	3.0±0.13		2.55±0.11
Iron-TYR distance (Å)			
Heme A	2.01	2.00	2.02
Heme B	2.00	1.92	1.99
Heme C	1.96	1.89	1.96
Heme D	2.04	2.01	1.96
	2.0±0.03	2.0±0.06	1.98±0.025
iron – water distance^b (Å)			
Heme A	4.37	4.00	4.27
Heme B	4.41		4.20
Heme C	4.11		4.25
Heme D	4.10	3.98	4.21
	4.25±0.17	3.99±0.01	4.23±0.029

^aRoot mean square deviation (RMSD) from ideal geometry, RMSDs of dihedrals and impropers were 23° and 1°, respectively, for all models. ^bDistance from the heme iron to the closest water molecule near His 74

3.1.2 Ammonia-bound Catalase form (Cat-NH₃)

A refined model with an R_{cryst} value of 23.7% at 1.99Å is obtained. As shown in Fig. 1.2A, a catalase molecule has four subunits and each subunit contains a heme B as an active site. Previously-solved crystal structures, under the same conditions as ours, show that the BLC typically incorporates one tightly bound NADPH per subunit (Kirkman and Gaetani, 1984, Fita & Rossmann, 1985). However, our structure shows no electron density due to NADPH in the expected region (Fig. 1.2C). From this, we conclude that the NADPH is lost during purification by size exclusion. The total number of water molecules is around 2100 suggesting the catalase is a wet protein (Fig. 1.2D). A large number of water molecules are found in 140 cavities (Tab. 3.2). Adding all the waters to the structure, the R-factor is decreased to 16.8%. For Cat-NH₃, a strong positive electron density feature is present

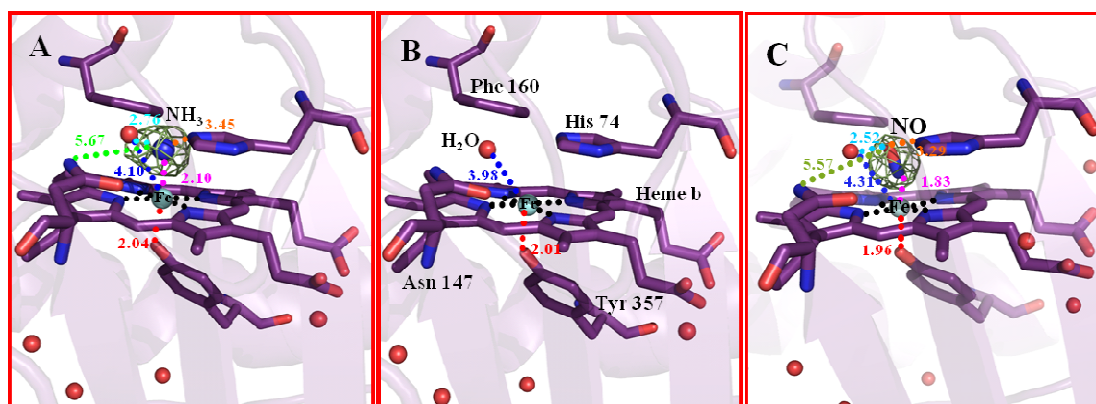


Figure 3.1 Structure of the heme pocket in the three different catalase forms. Water molecules within 8Å of the heme iron are displayed (red spheres). A sigmaA weighted *mFobs-DFcalc* simulated annealing difference map is shown in green (3.7 σ). **A.** Cat-NH3 **B.** Cat-5 **C.** Cat-NO. All the relevant residues in the heme pocket are marked in panel B. Figure from Purwar et al., 2011.

near the heme iron (Fig. 3.1A). Since high concentrations of ammonium are present in the crystallization buffer, we propose that the electron density arises from an ammonia molecule bound to the heme iron. For each of the four hemes, the electron density at the 6th coordination site is integrated. The electron count at each active site is around $\sim 9 e^-$, which supports the fact that the sites are fully occupied by NH_3 . An NH_3 model is placed into the electron density at a distance of 1.9 Å using a bond length restraint of $\sim 50 \text{ kcal mol}^{-1} \text{ Å}^{-2}$ and its position is refined. The occupancy of the NH_3 molecule refined to ~ 1.0 for all four subunits. The model precision is 0.18 Å as estimated by a Luzzati plot (Sec. 2.1.20). The Number of Ramachandran outliers is around ~ 53 (Tab. 3.1). For all four subunits, tilt angle of NH_3 molecule with respect to the heme plane is calculated (Tab. 3.1). An average value of the tilt angle is $\sim 5^\circ$. For this crystal form, iron out of plane distance for each heme is approximately $\pm 0.05 \text{ Å}$ which indicates that the iron is almost in plane (Tab. 3.1).

3.1.3 The five-coordinate Cat-5

The final model of Cat-NH₃ is used as a starting model to refine Cat-5. After removing the ammonia molecule at the 6th coordination site of the iron, as well as the water molecules, the model is refined to 1.9Å (Tab. 3.1). Inclusion of water molecules lowered the R-value from 24.1% to 22.1%. About 1200 waters are found. Almost no positive density appeared at the heme active site (Fig. 3.1B) where NH₃ molecule is bound in the first crystal form Cat-NH₃. By integrating the faint electron density features around the sixth coordination site, the average electron count is less than 1 (Tab. 3.1). This demonstrates that NH₃ molecule is successfully removed from this crystal form, leaving a vacant 6th coordination site at the iron. The heme iron is 5-coordinate and therefore we call this crystal form Cat-5.

Table 3.2 Number of cavities in some selected proteins. Table from Purwar *et al.*, 2011.

	# of cavities	H ₂ O in cavity/total H ₂ O	%	PDB-entry
Catalase ^a	140	100/1282	8	This work
Catalase (human, 1.5 Å) ^b	108	197/2298	9	1DGF
Cytochrome-c oxidase ^c	95	85/1579	5	3ABK
L29W-Mbdeoxy ^d	2	1/100	1	2BLI
Mbdeoxy (to 1.15 Å) ^e	2	0	0	1A6N

^a This study; ^b (Putnam *et al.*, 2000); ^c (Ohta *et al.*, 2010); ^d (Nienhaus *et al.*, 2005),

^e (Vojtechovský *et al.*, 1999)

3.1.4 Cat-NO Structure

The amount of NO needed to observe significant binding to the catalase crystals is optimized by varying the DEANO concentration from 10 to 200 mM. DEANO concentrations above 100 mM provide more than 50% NO occupancy in the heme pocket. Data are collected to 1.88Å (Tab. 3.1). The ammonia-free (Cat-5) structure without the water molecules is used as the initial model for the refinement. After inserting the waters, the R-value drops from 24.1% to 18.6%. For this crystal form, total

~2000 water molecules are found. Similar number of water molecules was observed for Cat-NH₃ form whereas for Cat-5, only 1200 waters were observed (Tab. 3.1). A positive electron density feature appears at the 6th coordination site of the heme iron (Fig. 3.1C), which was absent in Cat-5. This positive electron density is identified as a NO molecule. The refined NO occupancy is around ~ 55% on average (Tab. 3.1). A single water molecule is observed in the vicinity of the NO for all four hemes. This seems to be an important factor in defining the binding geometry of the NO with respect to the heme plane (see Discussion). The NO is slightly bent with respect to the heme plane as described above (Fig. 2.30B, Fig. 3.1C and Tab. 3.1). For the different subunits the bending angle varies between 5° and 20°, with an average of 12°. Note, that the bending angle strongly depends on the restraints employed. If the bending angle is allowed to vary in an unrestrained fashion, the bending angle increases up to ~ 70° (data not shown). The distance from the iron to the NO nitrogen refined to 1.85 Å, and the distance from the NO oxygen to the heme-pocket water is 2.5 Å. This indicates a strong hydrogen bond (Fig. 3.1C and Tab. 3.1).

Table 3.3 Tilt+bend angles for NO found in different heme-iron proteins with the iron in different oxidation states (Mb: myoglobin, NP4: nitrophorin 4). Table from Purwar *et al.*, 2011.

Nitrosyl complexes	tilt+bend [°]
Mb(Fe ²⁺)NO ^a	60
Mb(Fe ³⁺)NO ^a	33
NP4(Fe ³⁺)-NO ^b	70/3
NP4(Fe ³⁺)-NO ^c	24
NP4(Fe ²⁺)-NO ^d	40
Catalase (Fe ⁺³) (this study)	19

^a (Copeland *et al.*, 2003); ^b (Weichsel *et al.*, 2000); ^c (Roberts *et al.*, 2001), ^d (Maes *et al.*, 2005)

Table 3.4 Structural differences in Å relative to Cat-5 averaged over all 4 subunits. Table from Purwar et al., 2011.

	Cat-NH ₃	Cat-NO
Fe out of plane and heme nitrogens [Å]	0.1±0.01	0.1±0.01
	proximal side of the heme [Å]	
TYR 357-O _η	0.11±0.02	0.14±0.04
	distal side of the heme [Å]	
HIS 74-N _{δ1} / N _{ε2}	0.12±0.06	0.14±0.06
ASN 147-O _{δ1} / N _{δ2}	0.12±0.07	0.16±0.08
PHE 160-C _ζ	0.15±0.03	0.13±0.07
Total RMS differences ^a	0.34±0.04	0.37±0.05

^a The structures were superimposed by a least-squares fit (Xfit) (McRee, 1999).

3.2 Interaction of Nitric Oxide (NO) with Catalase: Micro-spectrophotometric analysis

3.2.1 Spectral changes for Cat-5, Cat-NH₃ and Cat-NO

For Cat-5 a total of 60 absorption spectra $A(\lambda)_{\Delta t}$ and the corresponding $\Delta A(\lambda)_{\Delta t}$ and $\Delta A_{\text{int}}(t)$ are plotted in Fig. 3.2A, 3.2D & 3.2G, respectively. Spectral changes that are characteristic to the reduction of heme iron from Fe(III) (met) to Fe(II) (deoxy) appear for exposure time over ~100s (Fig. 3.2A & 3.2D)(Shimizu et. al., 1988). On longer timescales the area of the integrated difference spectrum $\Delta A_{\text{int}}(t)$ decreases which may indicate crystal degradation (Fig. 3.2G). When the experiment is repeated with other crystals of the Cat-5 form, the rate of initial rise remains fairly invariant. However, the rate of subsequent decay varies significantly from one experiment to the other (data not shown). For Cat- NH₃, $A(t_i)$, $\Delta A(t_i)$ and $\Delta A_{\text{int}}(t_i)$ are plotted in panel B, E and H, respectively. The observed spectral changes for Cat-NH₃ are bit more complicated than for Cat-5, but they still exhibit features characteristic of heme reduction (Fig. 3.2B & 3.2E). Panels C, F and I represent $A(t_i)$, $\Delta A(t_i)$ and $\Delta A_{\text{int}}(t_i)$ for Cat-NO, respectively.

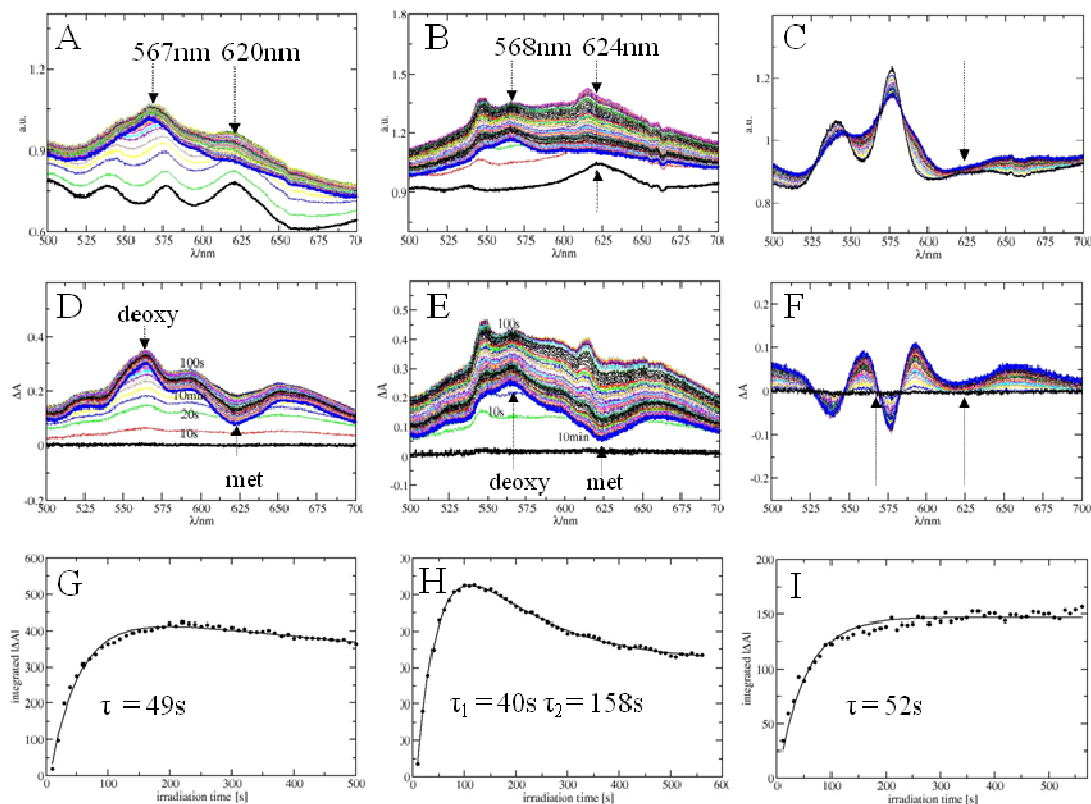


Figure 3.2 Spectral changes of catalase crystals after X-ray exposure (500 nm to 700 nm). Soret-band region (~ 410 nm) is excluded due to the saturation effects originating from the high absorption through the crystal. **A-C.** The absorption spectra for the Cat-5, Cat-NH₃ and Cat-NO crystals are shown in panel A, B and C, respectively. Thick black lines: reference spectra, thick blue lines: spectra after 10 min of the X-ray exposure. Note that for the Cat-5 (A) and Cat-NH₃ (B), the met-peaks (vertical dotted arrows) around 630 nm disappear and the deoxy peaks (vertical dotted arrows) around 560 nm appear. **D-F.** The corresponding difference spectra obtained by subtracting the reference spectra. Thick black lines: difference spectra directly after opening the X-ray shutter, thick blue lines: difference spectra collected after 10 min. The met and deoxy peak positions are again indicated by dotted arrows. **G-I.** The temporal progression of the integrated absolute differences for the 3 crystal forms. For Cat-5 (G), data are empirically fitted by an exponential and a linear decay. For Cat-NH₃ (H) data is fitted by two exponentials and for Cat-NO (I) data is fitted by a single exponential. Fitted data: black solid curves. The characteristic times are indicated. Figure from Purwar et al., 2011.

Interestingly the broadening of the signal is observed in this crystal form (Fig. 3.2C & 3.2F). A similar type of behavior is observed when nitrosylated myoglobin (Hoshino et.

al., 1996) or nitrophorin (Weichsel *et al.*, 2005) are reduced. Note that almost no decay is observed in $\Delta A_{\text{int}}(t)$ (Fig. 3.2I) whereas this decay is immediately evident for Cat-5 as well as for Cat-NH₃ (Fig. 3.2H & I). Our spectrophotometric data show that catalase is reduced after 10 minutes while illuminated with X-ray beam.

3.3 Time-resolved Laue crystallography: Effect of X-ray dose on PYP

3.3.1 Data processing

Laue data are processed up to 1.6 Å (Tab. 3.5). Since the data quality is poor in the last resolution shell, the difference maps are calculated to 1.8 Å. In order to address the radiation damage, the mean intensity $\langle I \rangle$, and the mean of the ratio of the intensity over its experimental uncertainty, $\langle I/\sigma_I \rangle$, in the resolution shell 1.9 to 1.8 Å are calculated. We used unscaled raw reflection intensities derived from the integration of the Laue spots.

3.3.2 Average absorbed dose

For the PYP1 crystal, the absorbed dose by the X-ray illuminated voxel (d_{vox}) is 0.244×10^4 Gy (Schmidt *et al.*, 2012). The dose deposited to the total irradiated crystal volume is 0.0414×10^4 Gy (Eq. 2.28). Average X-ray dose per time series is 3.3×10^5 Gy. The total absorbed dose (D_{nc}) in all 12 time series is ~ 4 MGy. In Fig. 3.3A, the $\langle I \rangle$ and $\langle I/\sigma_I \rangle$ values (solid and open squares, respectively) from all the datasets collected at time delay 32 ms are plotted as a function of uncorrected absorbed dose. The $\langle I \rangle$ and $\langle I/\sigma_I \rangle$ are fitted by a single exponential and, the half value for uncorrected dose ($D_{1/2, \text{nc}}$) is measured (Fig. 3.3A). $D_{1/2, \text{nc}}$ is more than 18.4×10^5 Gy when the $\langle I \rangle$ values are used and is $\sim 20 \times 10^5$ Gy when the $\langle I/\sigma_I \rangle$ values are used (Fig. 3.3A & Tab. 3.6).

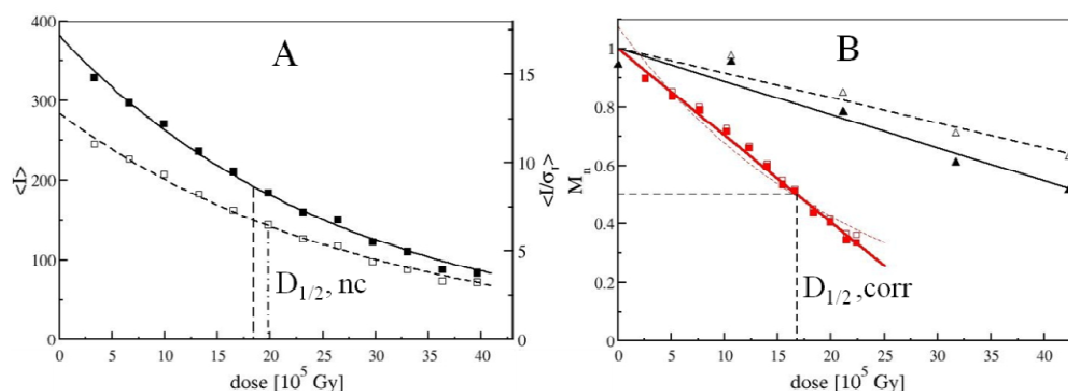


Figure 3.3 **A.** Raw mean intensities (solid squares) and (open squares) as a function of absorbed dose. Data fitted by exponential functions (solid black curve and dashed black curve, respectively for). Vertical dashed and vertical dashed-dotted lines denote the corresponding half value of uncorrected absorbed dose $D_{1/2, nc}$. **B.** Variation of the normalized mean intensities and as a function of virtual dose observed in the control experiment (black solid triangles and black open triangles, respectively). The data are fitted correspondingly by black solid and black dashed lines. Normalized intensities (red solid squares) and (red open squares), free from laser damage, are plotted as a function of adjusted dose. Fitting of the data with a straight line (red solid line) and with an exponential function (thin dashed line) is shown. The vertical dashed line represents the value which is same for and . Figure from Schmidt et al., 2012.

Table 3.5 Data statistics for 1st, 6th and 12th time-series after analysis with Precongnition/Epinorm. Table from Schmidt et al., 2012.

Short time-series	1 st			6 th			12 th		
time-delay	dark	2ms	32ms	dark	2ms	32ms	dark	2ms	32ms
Completeness (%) ^a	80.05	73.58	79.34	76.38	73.8	75.72	68.57	67.84	67.86
Completeness (%) ^b	66.88	55.97	66.39	59.81	54.62	58.18	44.96	43.40	43.93
R _{merge} on F ² (%)	5.74	6.01	5.75	6.02	6.83	6.30	7.93	7.83	8.14
	24.83	24.05	25.21	22.9	20.92	22.32	18.59	18.74	17.52
^b	13.81	13.21	15.91	14.32	11.97	15.92	6.00	13.60	13.87
R _{scale} 1.6-1.64		11.7	11.1		13.2	12.7		15.3	14.9
		-7.4	-4.9		-6.9	-4.4		-4.8	-4.3
		6.7	4.6		5.7	4.6		5.3	4.9

^a Resolution range: 1.00~1.6Å, ^b resolution range: 1.87~1.6Å,

3.3.3 Correction to the absorbed dose ()

For the actual data, the total shared volume $\langle V_c \rangle$ owing to subsequent crystal settings is 77% (Tab. 3.6) and therefore 23% of fresh volume on an average is exposed in different crystal settings (Sec. 2.2.6, Fig. 2.31B) (Schmidt *et al.*, 2012). For the first 5 time series, vertical displacements $\langle y' \rangle$ are negligible (Tab. 3.6). Large values of $\langle y' \rangle$ are observed from 5th to 12th time series and a total 25 % of the X-ray probed volume is freshly exposed. The corrected X-ray doses D_{corr} are obtained (Fig. 3.3B & Tab. 3.6).

3.3.4 Correction for laser damage using the control experiment

The thickness of the crystal used for laser experiment is 150 μ m. The common shared volume $\langle V_c \rangle$ is 80% which is slightly larger than that obtained for real time series (77%). No correction is needed due to vertical displacements $\langle y' \rangle$ of the X-ray beam because crystal positions remain fairly stable in all dark X-ray exposures (data not shown). The corrected virtual doses D_L are obtained (Fig. 3.3B). The $\langle I \rangle^L$ (solid black triangles) values are plotted as a function of D_L and fitted by a straight line with the slope $S_L = - 0.0113 \times 10^{-5} \langle I \rangle / \text{Gy}$ (Fig. 3.3B). The virtual half dose value $D_{1/2}^L$ (not shown), at which the normalized intensity reaches half of its maximum value, is about 4.5 MGy. The intensity free from the laser damage, $\langle I \rangle_{\text{free}}$, is calculated (Eq. 2.30) and plotted as a function of corrected absorbed dose D_{corr} (Fig. 3.3B). The $\langle I \rangle_{\text{free}}$ values (red solid squares) as are fitted by a straight line as well as by a single exponential. The crystallographic dose limit is given by $D_{1/2}^{corr} = 16.8 \times 10^5 \text{ Gy}$, which is same whether $\langle I \rangle_{\text{free}}$ or $\langle I / \sigma_I \rangle_{\text{free}}$ are used (Fig. 3.3B & Tab. 3.7).

Table 3.6 Absorbed doses (in 10^5 Gy) for 12 consecutive time-series, before and after corrections. N is the number of reflections in the resolution shell 1.9-1.8 Å. $\langle I \rangle_{32ms}$ and $\langle I/\sigma_I \rangle_{32ms}$ are determined from the 32 ms time point in the resolution shell 1.9-1.8 Å. $\langle I \rangle_{free}$ and $\langle I/\sigma_I \rangle_{free}$ are determined from dose data after applying laser corrections; Table from Schmidt et al., 2012.

time-series	1	2	3	4	5	6	7	8	9	10	11	12
Average dose nc^a	3.3	6.6	9.9	13.2	16.5	19.8	23.1	26.4	29.7	33.0	36.3	39.6
D_{corr}^1 ($V_c=77\%$)	2.54	5.08	7.62	10.16	12.71	15.25	17.79	20.32	22.87	25.41	27.95	30.49
$\langle y' \rangle$ [μm]	0	0	0	0	2	5	8	11	12	13	14	16
D_{corr}^2 ($V_c + \langle y' \rangle$)	2.54	5.08	7.62	10.16	12.29	13.98	15.41	16.59	18.30	19.90	21.42	22.36
$N_{reflections}$	3852	3860	3861	3861	3861	3859	3853	3864	3889	3908	3888	3894
$\langle I \rangle_{32ms}$	330	297	271	237	211	185	160	151	123	110	88	84
$\langle I \rangle_{free}$	337	310	289	258	233	206	181	172	142	128	104	100
$\langle I/\sigma_I \rangle_{32ms}$	11.07	10.22	9.35	8.23	7.33	6.50	5.71	5.31	4.42	3.98	3.33	3.26
$\langle I/\sigma_I \rangle_{free}$	11.31	10.67	9.97	9.00	8.10	7.28	6.47	6.07	5.12	4.66	3.94	3.89
τ_{SVD} [ms]	22	20	26	30	24	21	29	35	27	25	18	24
τ_{post} [ms] ($1/k_2$)	23	23	27	30	48	65	95	89	168	136	113	nd
R^{AO}	6.04	7.27	5.72	6.12	3.91	3.04	2.49	2.45	2.07	1.8	1.57	1.53

^a not corrected, ¹ dose correction (D_{corr}) due to crystal settings ² correction due vertical displacements are added to the D_{corr} , nd not detected

3.3.5 First Right singular vectors (rSVs) from SVD

After the SVD analysis, only one significant right singular vector (rSV1) for all 12 time series is found. Here, the rSVs for the 1st and 10th time-series are shown (Fig. 3.4). The rSVs for the first time course (rSV1(1st), black solid spheres) is fitted by the sum of two exponentials, one for a rising phase and another for a decaying phase with a relaxation time $\tau(1)_{rSV1}$ (Fig. 3.4A). For comparison, rSV1(1st) is fitted with one exponential with the same characteristic time $\tau(1)_{rSV1}$. In the 10th time-series, a rising phase is barely observed in rSV1(10th) (Fig. 3.4B).

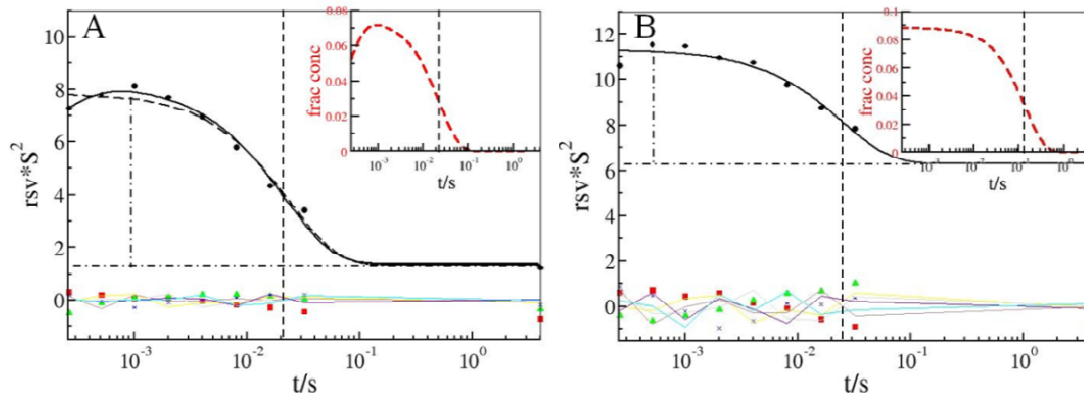


Figure 3.4 The right singular vectors (rSVs) for the two short time-series (1^{st} and 10^{th}). Black solid spheres: 1^{st} rSV, red solid squares: 2^{nd} rSV, green solid triangle: 3^{rd} rSV, blue stars: 4^{th} rSV and thin colored lines: 5^{th} to 8^{th} rSVs. Only 1^{st} rSV (rSV1) is significant. **A.** 1^{st} short time series that is exposed to the lowest absorbed dose. Black solid curve: fitting of rSV1(1) with two exponentials, with a source (not shown) and a decaying phase (Vertical dashed line); Black long dashed curve: fitting with only one exponential with the same relaxation time; vertical dashed-dotted line: amplitude of rSV1(1); horizontal dashed-dotted line: offset of rSV1(1). Insert: red dashed curve: concentration profile of pB1. Black dashed line: relaxation time from inverse of rate-coefficient k_2 . **B.** 10^{th} short time series that is exposed to the high absorbed dose. Vertical dashed line: relaxation time of the decaying phase from the fit of only one exponential. Vertical and horizontal dashed-dotted lines, red dashed curve and vertical dashed line of insert represent the same variables as described for panel A. Figure from Schmidt et al., 2012.

Consequently, only one exponential with $\tau(10)_{\text{rSV1}}$ is used for the fit. Both $\tau(1)_{\text{rSV1}}$ and $\tau(10)_{\text{rSV1}}$ are very similar, however the amplitudes and the offsets of rSV1(1) and rSV1(10) differ grossly (compare Fig. 3.4A & B).

3.3.6 The ratio of the amplitude to the offset

The level of noise in the difference electron density maps becomes higher with increasing radiation damage. As observed, the offset in rSV1(10^{th}) is larger than rSV1(1^{st}) (Fig. 3.4). This effect has also been noticed in spectroscopy (Henry & Hofrichter, 1992).

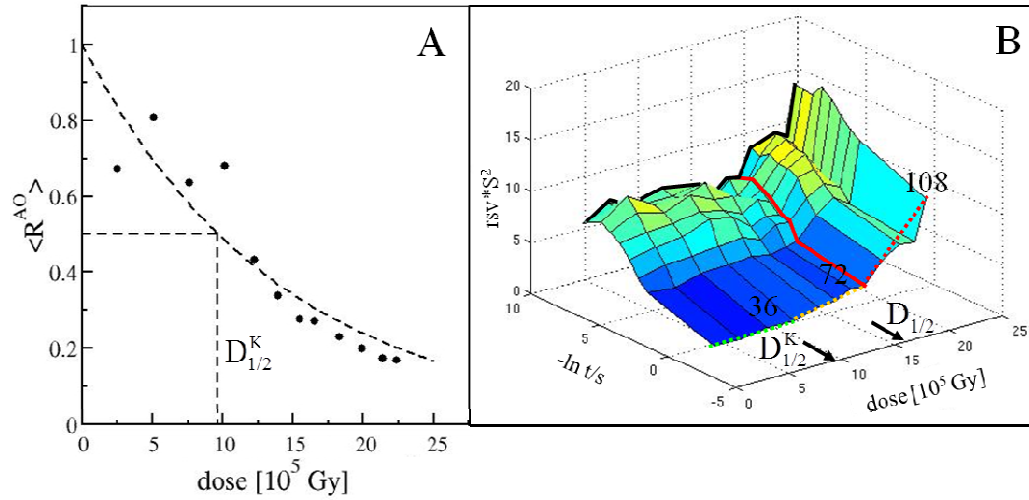


Figure 3.5 **A.** Normalized R^{AO} values (black spheres) for rSV1 of all 12 time series as a function of adjusted dose. Black dashed curve: data fitted by a single exponential; Horizontal and vertical dashed line: $\langle R^{AO} \rangle$ and corresponding kinetic dose limit $D_{1/2}^K$. **B.** Three dimensional plot of rSV1 for all short time-series as a function of corrected dose. The offsets in the rSV1s are indicated by the colored dotted lines. Green dotted line: small offsets; orange dotted line: offset increases slightly; red dotted line: offset increases strongly. The orange regime ends after 72 data sets. The red line indicates that posterior analysis of the data beyond this dose will not be possible. Figure from Schmidt et al., 2012.

From the first rSV (rSV1), we calculate the ratio of the amplitude to the offset ($\langle R^{AO} \rangle$, Tab. 3.6). This ratio is then computed for the rSV1s of all the 12 time-series. The calculated $\langle R^{AO} \rangle$ are plotted as a function of dose and fitted by a single exponential (black spheres (Fig. 3.5A). From the fit, $\langle R^{AO} \rangle$ is determined and the corresponding dose is the kinetic half-value, $D_{1/2}^K = 9.7 \times 10^5$ (Fig. 3.5A & Tab. 3.7). The rSV1s for all the time-courses are plotted in the three dimensions (Fig. 3.5B). The $\langle R^{AO} \rangle$ is reached after 4 short time series or 36 data sets (compare Fig. 3.5A & B)

3.3.7 Relaxation times

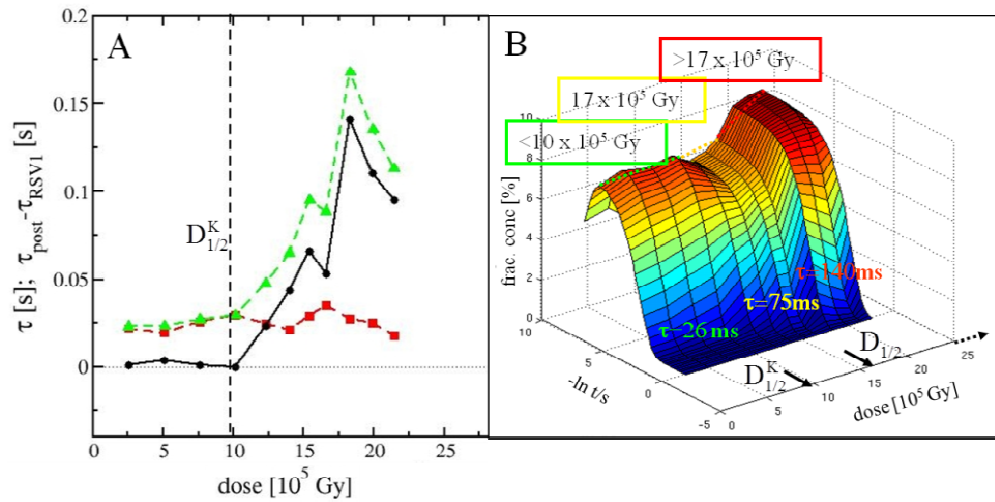


Figure 3.6 **A.** Relaxation times obtained from the SVD analysis (Red squares) and from the posterior analysis (Green triangles) as a function of adjusted dose. The red and green dashed lines are guide to the eye. Black spheres: difference between and . The vertical dashed line indicates the kinetic dose limit . **B.** Three-dimensional plot of all fitted time courses from the posterior analysis as a function of correct dose. The green, orange and red regimes and the approximate relaxation times in these regimes are marked. Figure from Schmidt et al., 2012.

Table 3.7 and derived from uncorrected and corrected dose data. Table from Schmidt et al., 2012.

	(Gy)	(Gy, Sec. 3.3.6)
$\langle I \rangle$; uncorrected dose	18.4×10^5	
$\langle I/\sigma_I \rangle$; uncorrected dose	19.7×10^5	
$\langle I \rangle_{\text{free}}$; corrected dose	16.8×10^5	
$\langle I/\sigma_I \rangle_{\text{free}}$; corrected dose	16.8×10^5	
R^{AO} ; uncorrected dose (not shown in Fig. 3.5A)		16.0×10^5
R^{AO} ; corrected dose		9.6×10^5

The relaxation times (red solid squares) extracted from the first rSVs and those calculated from the posterior analysis (green solid squares) are plotted (Fig. 3.6A). Up to the $= 9.7 \times 10^5$ Gy, the relaxation times agree with relaxation times . After , and start to diverge as shown in Fig. 3.6A & B. For higher absorbed dose such as $\sim 22 \times 10^5$ Gy, the time scale of the reaction from the SVD analysis

is still 26 ms, however the time scale from the posterior analysis reaches up to 140 ms (Fig. 3.6).

3.4 Time-resolved Laue crystallography: Effect of pH on PYP

3.4.1 Data processing

Data are processed up to 1.6 Å. The completeness of the data to this resolution is acceptable and excellent up to 1.8 Å. Difference maps are calculated to 1.8 Å. Data collection statistics at pH 4, 7 and 9 for some selected time points are shown (Tab. 3.8). R_{merge} on $|F|^2$ is around 4.5% for pH 7, < 6% for pH 4 and ~5 % for pH 9, showing the excellent data quality. R_{scale} is obtained when time-dependent data sets are scaled to the dark (reference) data at a resolution of 1.6 Å. For all three pH's R_{scale} are compared (Tab. 3.8).

Table 3.8 Data collection statistics for PYP at three different pH conditions. $\Delta\rho$ denote highest positive and lowest negative difference electron density features in the unit of σ value that is used for the difference maps. Table from Tripathi et al., 2012.

	pH 7			pH 4			pH 9		
time delay (t_i)	4 μ s	512 μ s	512ms	4 μ s	512 μ s	512ms	4 μ s	512 μ s	512ms
Completeness (%) ^a	70.5	70.4	71.5	70.5	70.4	71.5	74.4	74.2	75.4
Completeness (%) ^b	38.3	37.5	40.8	38.3	37.5	40.8	35.4	35.2	37.7
$\langle I/\sigma_I \rangle$	29.8	26.5	29.5	29.8	26.5	29.5	23.9	24.6	25.8
R_{merge} on $ F ^2$ (%)	4.6	5.1	4.6	4.6	5.1	4.6	5.8	5.6	5.4
R_{scale} (%) ^b	11.2	12.8	10.1	11.2	12.8	10.1	15.8	15.4	12.4
$\langle \Delta F \rangle$ (e ⁻)	9.1	9.9	6.7	9.1	9.9	6.7	12.5	11.9	10.1
$\langle \sigma_{\Delta F} \rangle$	4.2	4.8	4.1	4.2	4.8	4.1	5.4	5.4	5.2
$\Delta\rho_{\text{min}}/\sigma_{\Delta\rho}$	-11.2	-6.8	-4.7	-11.2	-6.8	-4.7	-8.8	-7.3	-5.4
$\Delta\rho_{\text{max}}/\sigma_{\Delta\rho}$	12.1	6.6	4.9	12.1	6.6	4.9	9.6	6.2	5.8

^aResolution range 100 – 1.6 Å ^b in the last resolution shell 1.6-1.64 Å

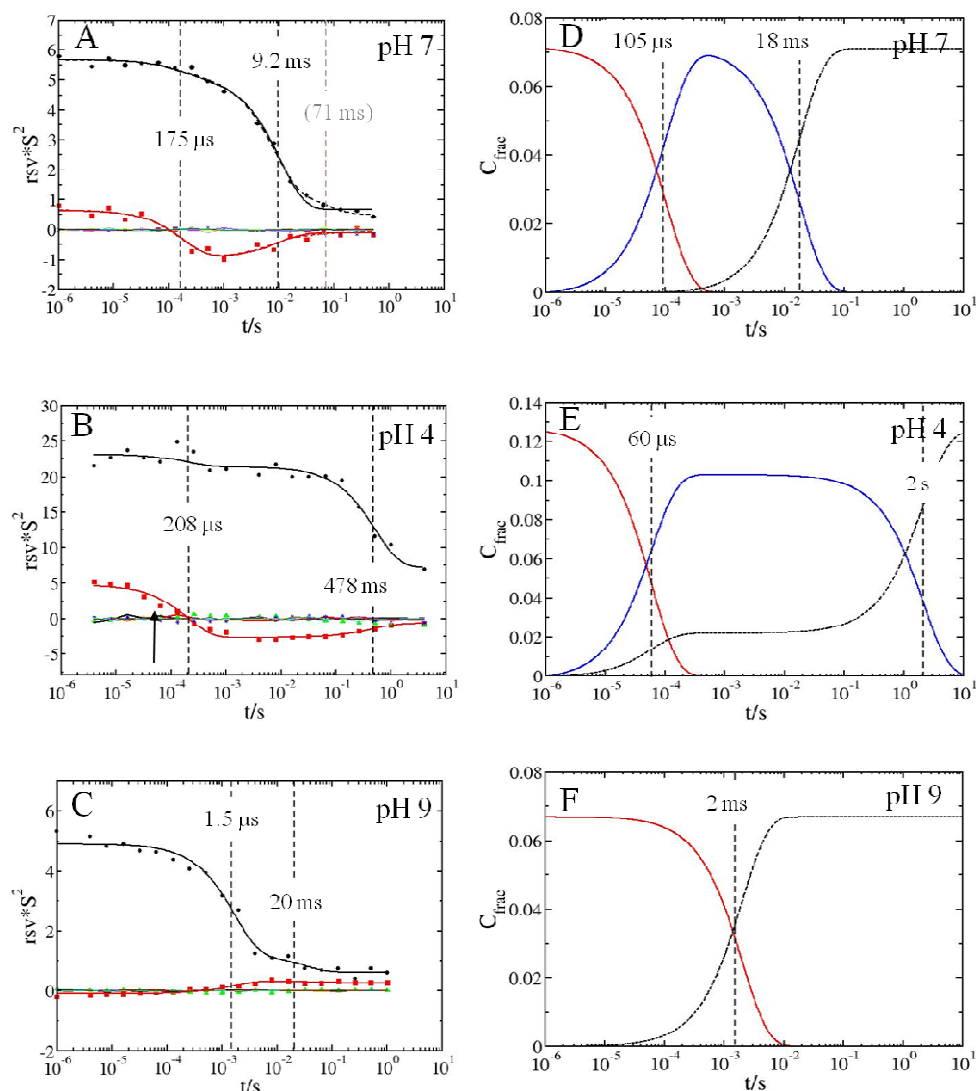


Figure 3.7 A-C. Right singular vectors obtained from the SVD analysis at three different pH's. 1st rSV: black spheres, 2nd rSV: red squares, 3rd rSV: green triangles. Two significant rSVs are present and each of them is fitted with sum of two exponentials. Fits for the 1st rSV (black solid curve) and the 2nd rSV (red solid curve) are shown. Relaxation times of the pR (τ_1) and pB (τ_2) determined from the fits are marked by vertical black dashed lines. **A.** at pH 7, 1st and 2nd rSVs are fitted by a sum of three exponentials. The third phase indicates a third intermediate with a relaxation time of 71 ms (gray dashed vertical line); **B.** at pH 4, **C.** at pH 9. **D-F.** Concentration profiles obtained from the posterior analysis using the proposed chemical kinetic mechanism (Fig. 2.17B). Relative concentration of intermediate pR (red), pB (blue), and pG (black) at **D.** pH 7.0 **E.** pH 4.0 and **F.** pH 9.0. Relaxation times τ_P (vertical dashed lines) calculated from microscopic rate coefficients k_i are shown. Figure from Tripathi et al., 2012.

The rSVs obtained from the SVD analysis of the difference maps are plotted as a function of time (Fig. 3.7). Two significant rSVs, rSV1 (black Solid spheres) and rSV2 (red solid squares), are present showing that two kinetic processes occur at each of three pH values (Fig. 3.7). Note, at pH 7, a small 3rd phase might be present (Fig. 3.7B), and at pH 9, the 2nd process is almost absent (Fig. 3.7C). The rSVs are fitted by sum of two exponentials except at pH 7 for which fitting is also tried with 3 exponentials. The relaxation times, τ_1 and τ_2 obtained from the fit correspond to pR and pB, respectively (Ihee *et al.*, 2005).

3.4.2 Averaged difference maps and extrapolated electron density maps of intermediates

For both pH 4 and 7, two kinetic processes corresponding to the pR and pB are present (Fig. 3.7A-B & 3.7D-E). The average difference maps for pR and pB are obtained and corresponding ΔF_{tind} are calculated as described in Sec. 2.2.14. N_c s are determined for both pH as well as for both intermediates (Sec. 2.2.14). For example, at pH 7 the values of N_c are about 15 and 25 for the pR and the pB states respectively. Using the N_c s, extrapolated maps are obtained (Fig. 3.8I.A & 3.8I.E). These maps are interpreted by atomic models which are subsequently refined and improved phases ϕ_{new} are obtained. Using ϕ_{new} and the measured difference structure factor amplitudes, new difference maps (Fig. 3.8D & 3.8H) as well as new extrapolated maps (Fig. 3.8I.C & I.G) are calculated. At pH 9 only one kinetic process corresponding to intermediate pR is clearly identified with τ_1 of 1.5 ms (Fig. 3.7C & 3.7F). An extrapolated map for the pR is calculated as described for the other pHs (Tripathi *et al.*, 2012). At this pH the 2nd process corresponding to pB is barely visible. The signal to noise ratio is too low in the difference map to obtain a meaningful extrapolated map. A very weak signal is found at the

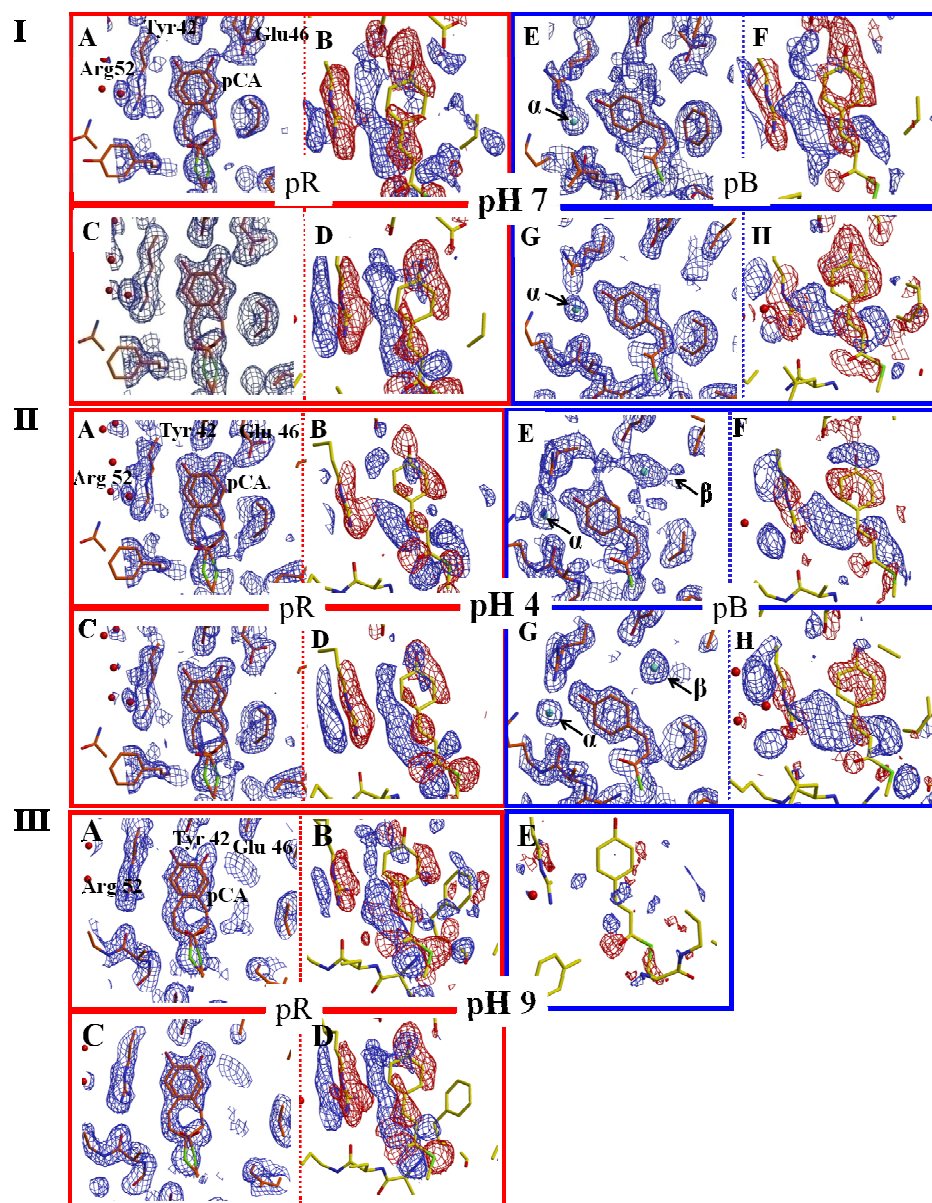


Figure 3.8 Extrapolated and difference electron density maps at different pHs. **I.** pH 7; **II.** pH 4 and **III.** pH 9. pR (left panels, A-D) and pB (right panels, E-H); Panel A, C, E & G denotes extrapolated electron density maps at 1σ level (blue contour lines). Atomic models of intermediate states (red lines) are shown. Panels B, D, F & G show difference electron density maps; positive (blue contour lines) and negative (red contour lines) difference electron density are contoured at $\pm 4\sigma$. The dark state (pG) model (in yellow) is shown. Extrapolated maps before (panel A & E) and after (panel C & G) phase improvement. Difference electron density maps before (panel B & F) and after (panel D & H) phase improvement. The (difference) electron density features α and β are indicated by the arrow in E and G. Figure from Tripathi et. al., 2012.

chromophore foot and also at Arg-52 that may suggest the presence of pB with very low

occupancy (Fig. 3.8 III.E).

3.4.3 Structural analysis of intermediates at pH 7, pH 4 and pH 9

Data collection and refinement statistics for intermediates, pR and pB are quite similar for all pH values (Tab. 3.8). In our case, the pR intermediate adopts two conformations (i) pR_{CW} and (ii) pR_{E46Q} as reported previously (Ihee *et al.*, 2005). For all three pH's, the relative occupancy of pR_{E46Q} is lower in compared to the pR_{CW}. In pR_{CW}, the hydrogen bonds (H-bonds) of the chromophore phenolic oxygen with Tyr-42 and Glu-46 are preserved. The bond length for Tyr-42 is 2.9 Å and for Glu-46 is 2.7 Å at pH 7 whereas these lengths are the same for both residues at pH 4 (2.8 Å) and pH 9 (2.9 Å). In pR_{E46Q}, the H-bond with Glu-46 is broken while that to Tyr-42 is preserved at a distance of 2.8 Å for all three pHs. In the case of pB, the H-bonds to Tyr-42 and Glu-46, both are broken. The chromophore head and Arg-52 are exposed to the protein solvent. In the extrapolated and difference density maps of the pB state, a feature (α) is detected close to chromophore phenolic oxygen, both at pH 7 and 4 (Fig. 3.8I.E & I.G; 3.8II.E & II.G). The feature α is interpreted as a water molecule which is H-bonded to the phenolate oxygen of the chromophore. The corresponding H-bond distance is 2.6 Å for pH 7 and 2.8 Å for pH 4. At pH 4, for state pB another large feature β appears in the chromophore pocket near Glu-46 and Tyr-42 (Fig. 3.8I.E & I.G; 3.8II.E & II.G). This feature has never been observed in any time-resolved crystallographic difference map on PYP. It is also interpreted as an additional water molecule which is H-bonded to Tyr-O_η with a distance of 2.7 Å and weakly bonded to Glu-46 O_{ε1} with 3.3 Å.

3.4.4 Kinetic Analysis

The relaxation times (τ_i) obtained from fitting of the rSVs are shown in Tab. 3.9. No significant differences are observed in τ_1 for the pR state at pH 4 and pH 7. However, $\tau_1=1.5$ ms is significantly slower at pH 9. The relaxation time (τ_2) for pB to dark state transition is more than 52 fold longer at pH 4 as compared to pH 7 (Tab. 3.9). The rate coefficients k_1 , k_2 and k_3 determined from the posterior analysis are shown in Tab 3.9. At pH 7, the rate coefficient k_3 is much smaller than k_1 . This suggests that the pathway from pR directly to pG is irrelevant at pH 7. At pH 4, k_3 is more than 20% of k_1 which indicates that a fraction of the molecules relaxes directly from pR to pG. At pH 9, the low occupation of pB did not allow the refinement of k_1 and k_2 . The value of $k_3 = 494 \text{ s}^{-1}$ implies that pR mainly decays directly to the pG, and pB is almost absent.

Table 3.9 Relaxation times from SVD analysis (τ_1 & τ_2). Rate coefficients (k_1 , k_2 & k_3) and their inverse, τ_p from the posterior analysis. Table from Tripathi et. al., 2012.

	pH=7	pH=4	pH=9*
τ_1	175 (+/- 8) μs	208 (+/- 12) μs	1.5 (+/-0.1) ms
τ_2	9.2 (+/-0.2) ms	478 (+/- 0.2) ms	20(+/-0.1) ms
k_1	9730(+/- 9.58) s^{-1}	13800 (+/- 3.12) s^{-1}	0.0
k_2	55.8 (+/- 1.02) s^{-1}	0.475 (+/- 0.002) s^{-1}	0.0
k_3	0.0	2940 (+/- 5.62) s^{-1}	494 (+/-51.5) s^{-1}
τ_p	$\tau_{p1} = 1/k_1 \approx 100\mu\text{s}$ $\tau_{p2} = 1/k_2 \approx 18\text{ms}$	$\tau_{p1} = 1/(k_1 + k_3) \approx 60\mu\text{s}$ $\tau_{p2} = 1/k_2 \approx 2\text{s}$	$\tau_{p1} = 1/k_3 \approx 2\text{ms}$

* At this level of pB occupation, refinement of k_1 and k_2 is not possible.

3.5 Effect of temperature on PYP photocycle

3.5.1 Time-resolved Laue crystallography

3.5.1.1 Kinetic analysis

Data collection statistics are shown for all 14 temperature settings in Tab. 2.1.

Table 3.10 Relaxation times obtained (τ_i) from the fit of rSVs for all temperature settings. The macroscopic coefficients (Λ_i) are the inverse of τ_i . The temperature dependence of Λ_i are fitted by the Van't Hoff-Arrhenius equation. From these fitting, energy of activations are calculated.

Temperature (°C)	τ_1	τ_2	τ_3	τ_4
-40	11 ns	1.9 μ s	5.5 ms	1.4 s
-30	2 ns	120 ns	7 ms	420 ms
-20	2 ns	100 ns	5 ms	411 ms
-15	n.o.	36 ns	2.6 ms	537 ms
-10	n.o.	40 ns	3 ms	129 ms
0	n.o.	58ns	697 μ s	73 ms
10	n.o.	31 ns	300 μ s	28 ms
20	n.o.	24 ns	198 μ s	9 ms
25	n.o.	15 ns	198 μ s	12 ms
30	n.o.	10 ns	99 μ s	6 ms
40	n.o.	7 ns	41 μ s	4.4 ms
50	n.o.	n.o.	40 μ s	1.3 ms
Macroscopic rate coefficients	Λ_1	Λ_2	Λ_3	Λ_4
Pre-factor ν [1/s]	n.a.	1.6×10^{14}	1.9×10^{13}	7.7×10^{10}
Energy of activation E_a [kJ/mol]	na	35.9	53.4	49.6

n.o. not observed, n.a. not applicable

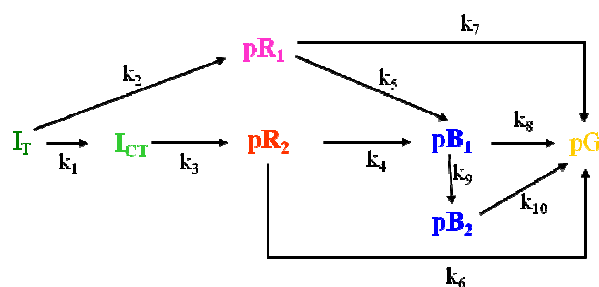


Figure 3.9 Chemical kinetic mechanism proposed for the PYP photocycle. Intermediates, I_T , I_{CT} , pR_1 , pR_2 , pB_1 and pB_2 are shown in different colors. Associated rate coefficients k_j are also shown. Figure from Schmidt et al., 2013.

The rSVs extracted from the SVD analysis for all temperatures are plotted as a function of employed time delays (Appendix E). The nomenclature for the PYP photocycle intermediates such as I_T , I_{CT} , pR_1 , pR_2 , pB_1 and pB_2 (Fig. 3.9) is same as described in

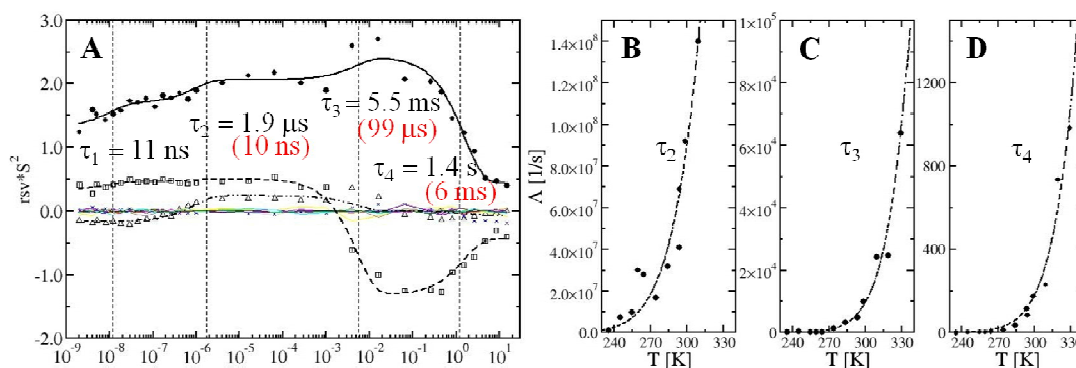


Figure 3.10 **A.** Right singular vectors (rSVs) at -40 °C. Four kinetic processes with $\tau_1 \dots \tau_4$ (dashed vertical lines) are globally observed. Solid spheres, open triangles, open squares denote first, second and third significant rSVs, respectively. Colored thin curves around zero line: less significant rSVs. Solid black curve, dashed curve, dashed double dotted curve are global fit of the significant rSVs by four exponential functions, respectively, with the same set of relaxation times but with different amplitudes. Relaxation times obtained at room temperature (25 °C, red) are shown for comparison in brackets. **B-D.** Macroscopic rates Λ (inverse of relaxation times) for processes τ_2 to τ_4 are plotted as function of temperature. Dashed curves: fits by the Van't Hoff-Arrhenius equation. Figure from Schmidt *et al.*, 2013.

previous works (Genick *et al.*, 1997a, Ihee *et al.*, 2005, Kim *et al.*, 2012, Jung *et al.*, 2013, Yeremenko *et al.*, 2006). At -40 °C, three significant rSVs are found which are globally fitted with 4 exponentials as shown in Fig. 3.10A. Correspondingly, four kinetic processes with relaxation times $\tau_1 = 11$ ns, $\tau_2 = 1.9$ μ s, $\tau_3 = 5.5$ ms and $\tau_4 = 1.4$ s are observed. The process with $\tau_1 = 11$ ns results from the non-zero laser pulse width and the decay of I_T to both I_{CT} and pR_1 that can be identified in the earliest difference maps. $\tau_2 = 1.9$ μ s results from the relaxation of state I_{CT} to pR_2 , $\tau_3 = 5.5$ ms from the joint relaxations of pR_1 and pR_2 to pB and pG and $\tau_4 = 1.4$ s from pB to pG (Fig. 3.10A). These processes accelerate at higher temperatures. For comparison, relaxation times at -40 °C (black colored numbers) and at 25 °C (red colored numbers in bracket) are shown in Fig. 3.10A.

The relaxation rates $\Lambda_i = 1/\tau_i$ are plotted as a function of different temperature settings employed in the experiment (Fig. 3.10B-D). The rates are fitted by the Van't Hoff-Arrhenius equation (Eq. 1.4). From the fitting, the pre-factors and the energies of activation are determined (Tab. 3.10).

3.5.2 Time-resolved spectroscopy

3.5.2.1 Dark absorption spectra of PYP in solution and on crystalline slurry

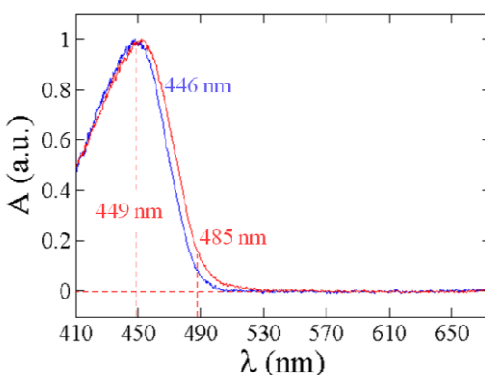


Figure 3.11 Dark absorption spectra for PYP in solution (blue) and on a crushed single crystal (red) measured by micro-spectrophotometer. Spectra are recorded from 25 accumulations of 25 μ s exposures. The absorption maxima are at 446 nm and 449 nm in solution and crystal, respectively. For a crystalline sample, absorption at a laser wavelength of 485 nm is approximately ten times smaller than at 449 nm.

A typical absorption spectrum obtained from PYP in solution (2 mg/mL) and on a crushed crystal is displayed in Fig. 3.11. Compared to solution, the absorption maximum for a crushed crystal is shifted by 3 nm.

3.5.2.2 Time-resolved spectra on PYP solution

Fig. 3.12 shows results from a time-series of absorption spectra collected from PYP solution at 10 time delays from 30 μ s to 2 s after reaction initiation. The dark spectra obtained before and after the time-series are shown in the inset of Fig. 3.12A, and it is

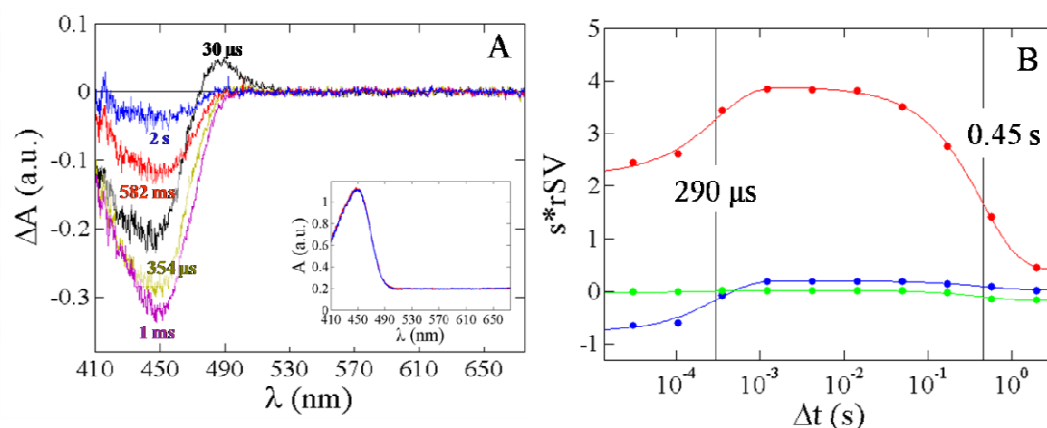


Figure 3.12 A. Time-resolved difference absorption spectra from 30 μ s – 2 s for PYP in solution at 295 K. Black spectrum: earliest time point; Blue spectrum: last time point. The inset shows the dark spectra collected before (red) and after (blue) the full time-series. No permanent bleaching has occurred. **B.** Two significant rSVs obtained from the SVD analysis of the spectral changes from 400 nm to 510 nm: 1st rSV (red circles); 2nd rSV (blue circles); 3rd rSV (green circles). Global fitting of the 1st, 2nd and 3rd rSV are represented by red, blue, and green curves, respectively, and relaxation times are shown as vertical lines.

apparent that no permanent bleaching has occurred. For the early time points around 100 μ s (colored black) a peak evolves at 485 nm and a sharp decrease is observed at 446 nm. As time progresses, the peak corresponding to 485 nm disappears and the 446 nm peak begins to recover. From the SVD analysis, two significant right singular vectors (rSVs) representing two kinetic processes are obtained as displayed in Fig. 3.12B. After global fitting of the rSVs by the sum of two exponentials, two relaxation times $\tau_1 = 290 \mu$ s and $\tau_2 = 0.38$ s are determined. The first process corresponds to the pR to pB transition with a lifetime of 290 μ s. The second process represents the recovery from the pB state to the ground state, pG.

3.5.2.3 Time-resolved spectra on PYP crushed single crystal

Difference spectra obtained from crushed single crystal at 0 $^{\circ}$ C (Fig. 3.13A) and 30 $^{\circ}$ C (Fig. 3.13B) are plotted as a function of wavelength from 400-600 nm. The dark spectra

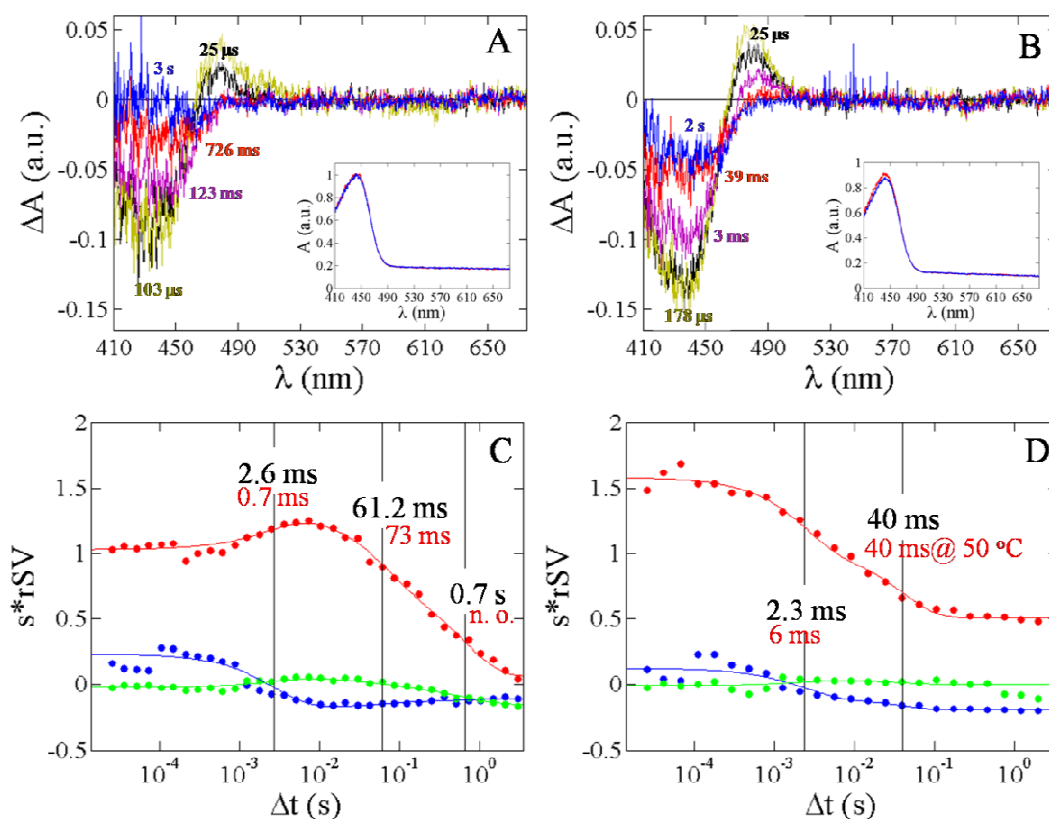


Figure 3.13 Time-resolved difference absorption spectra on crystalline slurry at different temperatures. The black horizontal line represents the difference spectrum corresponding to the dark (reference) spectrum. Black colored spectrum: 1st time point; blue colored spectrum: last time point **A.** $T = 0^\circ\text{C}$ **B.** $T = 30^\circ\text{C}$. **C-D.** Significant rSVs from the SVD analysis of the difference spectra obtained for PYP crystalline slurry at different temperatures. 1st, 2nd and 3rd significant rSVs are represented by red, blue and green spheres, respectively. Solid curves denote the global data fitting by the sum of exponentials. Respective relaxation times are represented as vertical lines. Relaxation times (red) are obtained from crystallography (n.o. means not observed). **C.** At 0°C three processes are identified and labeled with their respective relaxation times (, &) **D.** At 30°C two processes with their respective relaxation times (&) are labeled.

obtained before and after the time-series are shown in the insets of Fig. 3.13A & B. It is apparent that permanent bleaching is either absent or very small. rSVs obtained from the SVD analysis at both temperature settings are shown in Fig 3.14 C-D. At 0°C three significant rSVs equivalent to three kinetic processes are present (Fig. 3.13C). Process (1)

corresponds to the pR to pB transition with relaxation time $\tau_1 = 2.1$ ms. The pB to pG transition is biphasic and characterized by both processes 2 and 3. The values of τ_2 and τ_3 are 67 ms and 800 ms, respectively. Only 2 significant rSVs are observed at 30 °C. These two rSVs are equivalent to two processes (Fig. 3.13D). The relaxation time corresponding to the 1st process is 2.2 ms. A minor contribution from the 2nd process with $\tau_2 = 32$ ms is observed.

Table 3.11 Relaxation times (τ_i) and corresponding macroscopic rate coefficients (Λ_i) for PYP in solution and for a crushed single crystal.

	Solution		Crushed single crystal				
Temperature	295 K		273 K			303 K	
Relaxation times τ_i (ms)	0.29	380	2.1	67	800	2.2	32
Macroscopic rate coefficients Λ_i (s ⁻¹)	3.4x 10 ³	2.6	4.76x 10 ²	4.9	1.25	4.54x 10 ²	31

References

- Copeland, D. M., West, A. H. & Richter-Addo, G. B. (2003). *Prot. Struct. Func. Gen.* **53**, 182-192.
- Fita, I. & Rossmann, M. G. (1985). *Proc. Natl. Acad. Sci. USA* **82**, 1604-1608.
- Genick, U. K., Borgstahl, G. E., Ng, K., Ren, Z., Pradervand, C., Burke, P. M., Srajer, V., Teng, T. Y., Schildkamp, W., McRee, D. E., Moffat, K. & Getzoff, E. D. (1997a). *Science* **275**, 1471-1475.
- Henry, E. R. & Hofrichter, J. (1992). *Method Enzymol* **210**, 129-192.
- Ihee, H., Rajagopal, S., Srajer, V., Pahl, R., Anderson, S., Schmidt, M., Schotte, F., Anfinrud, P. A., Wulff, M. & Moffat, K. (2005). *Proceedings of the National Academy of Sciences of the United States of America* **102**, 7145-7150.
- Jung, Y. O., Lee, J. H., Kim, J., Schmidt, M., Moffat, K., Srajer, V. & Ihee, H. (2013). *Nature chemistry* **5**, 212-220.
- Kim, T. W., Lee, J. H., Choi, J., Kim, K. H., van Wilderen, L. J., Guerin, L., Kim, Y., Jung, Y. O., Yang, C., Kim, J., Wulff, M., van Thor, J. J. & Ihee, H. (2012). *J Am Chem Soc* **134**, 3145-3153.
- Kirkman, H. N. & Gaetani, G. F. (1984). *Proc. Natl. Acad. Sci. USA* **81**, 4343-4347.
- Maes, E. M., Roberts, S. A., Weichsel, A. & Montfort, W. R. (2005). *Biochemistry* **44**, 12690-12699.

- McRee, D. E. (1999). *J. Struct. Biol.* **125**, 156-165.
- Nienhaus, K., Ostermann, A., Nienhaus, G. U., Parak, F. G. & Schmidt, M. (2005). *Biochemistry* **44**, 5095-5105.
- Ohta, K., Muramoto, K., Shinzawa-Itoh, K., Yamashita, E., Yoshikawa, S. & Tsukihara, T. (2010). *Acta Cryst. F* **66**, 251.
- Putnam, C. D., Arvai, A. S., Bourne, Y. & Tainer, J. A. (2000). *J. Mol. Biol.* **296**, 295-309.
- Roberts, S. A., Weichsel, A., Qiu, Y., Shelnutt, J. A., Walker, F. A. & Montfort, W. R. (2001). *Biochemistry* **40**, 11327-11337.
- Schmidt, M., Srajer, V., **Purwar, N.** & Tripathi, S. (2012). *J Synchrotron Radiat* **19**, 264-273.
- Tripathi, S., Srajer, V., **Purwar, N.**, Henning, R. & Schmidt, M. (2012). *Biophysical journal* **102**, 325-332.
- Vojtechovský, J., Chu, K., Berendzen, J., Sweet, R. M. & Schlichting, I. (1999). *Biophys. J.* **77**, 2153-2174.
- Weichsel, A., Andersen, J. F., Roberts, S. A. & Montfort, W. R. (2000). *Nat. Struct. Biol.* **7**, 551-554.
- Weichsel, A., Maes, E. M., Andersen, J. F., Valenzuela, J. G., Shokhireva, T., Walker, F. A. & Montfort, W. R. (2005). *Proc. Natl. Acad. Sci. USA* **102**, 594-599.
- Yeremenko, S., van Stokkum, I. H. M., Moffat, K. & Hellingwerf, K. J. (2006). *Biophysical journal* **90**, 4224-4235.

4 Discussion

4.1 Catalase: structure and function

Our nitrosylated catalase (Fig. 3.1C) is of significant importance because it appears to be a good model system to mimic compound 1 ($\text{Fe-H}_2\text{O}_2$) (Eq. 1.2) that cannot either be recognized. The position of NO relative to the heme plane in our nitrosylated complex indicates the location of H_2O_2 bound in the actual catalytic reaction.

DEANO (Fig. 2.29 A) is a universal NO generator that can be used for all kinds of iron containing proteins. With the use of DEANO (Fig. 2.29A) and our simple glass apparatus (Fig. 2.29B), we can successfully produce 100 ~ 200 mmol/L of NO. The solubility of NO in water is ~2 mmol / L (Wilhelm *et al.*, 1977). With this solubility, a 100 mmol/L of NO corresponds to a partial pressure of ~ 50 bars. It is crucial to start with such high concentrations of NO because the dissociation rate of NO from the Cat-NO is very high (Tab. 4.1). As soon as the crystals are removed from the NO containing solution, they quickly begin to lose their bound NO by diffusion. In addition, catalase crystals have to be immersed in a cryo buffer before freezing them in the cryostream (Sec. 2.5.2). This process requires at least a few seconds, in which the NO may further diffuse out of the crystals. By immersing our catalase crystals in the tightly closed cavity (Fig. 2.29B), we could literally pressurized the crystal with NO. Pressurization of these crystals with such high NO concentration at pressures much higher than 1 bar, enables us to detect a substantial occupation of NO in the crystal.

Another advantage of our method is that with the 100 mmol/L DEANO, the concentration of NO is 2 orders of magnitude higher than that of oxygen. Even if all the

oxygen in solution is consumed in reaction with NO, plenty of nitric oxide is still available to form Cat-NO complex. Handling of NO as well as performing crystallographic experiments under complicated anaerobic conditions is not needed.

Table 4.1 On and off rates as well as binding constants (K) for several protein-NO (or CO) complexes. Table from Purwar *et al.*, 2011.

	k_{on} ($\text{M}^{-1} \text{s}^{-1}$)	k_{off} (s^{-1})	$K_{\text{CatNO}} = (k_{\text{on}}/k_{\text{off}})$ (M^{-1})
Mb(Fe^{2+})CO ^a	5.1×10^5	1.9×10^{-2}	2.7×10^7
Mb(Fe^{2+})NO ^a	1.7×10^7	1.2×10^{-4}	1.4×10^{11}
Mb(Fe^{3+})NO ^b	4.8×10^4	42	1.14×10^3
Lb(Fe^{2+})NO ^a	1.2×10^8	2.0×10^{-5}	5.9×10^{12}
NP1(Fe^{3+})NO ^c	1.5×10^6 (pH 5)	0.18 (pH 5)	8.3×10^6 (pH 5)
	1.5×10^6 (pH 8)	1.25 (pH 8)	1.2×10^6 (pH 8)
NP4(Fe^{3+})NO ^c	2.1×10^6 (pH 5)	0.11 (pH 5)	2.0×10^7 (pH 5)
	2.3×10^6 (pH 8)	1.24 (pH 8)	1.9×10^6 (pH 8)
Cat(Fe^{3+})NO ^d	1.3×10^7	1.5	8.7×10^6

^a Ref. (Rohlf *et al.*, 1988) ; Lb=LegHemoglobin; ^b Ref. (Laverman *et al.*, 2001); ^c Ref. (Andersen *et al.*, 2000); The nitrophorins adopt a closed and open conformation at pH 5 and pH 8, respectively; ^d This work (Purwar *et al.*, 2011)

NO binding has been observed for both ferrous and ferric iron-containing heme proteins (Tab. 4.1). It binds extremely tightly to ferrous compounds such as Mb (Fe^{2+}) or Lb (Fe^{2+}) with small dissociation rate coefficients k_{off} (Tab. 4.1). This leads to a larger binding constant ($K = k_{\text{on}}/k_{\text{off}}$) on the order of 10^6 or higher (Tab. 4.1). A kinetic analysis (Purwar *et al.*, 2011) of the dissociation of NO from Cat-NO shows that the binding constant $K_{\text{Cat-NO}}$ for our catalase (Fe^{3+}) is $8.7 \times 10^6 \text{ M}^{-1}$ (Tab. 4.1). Surprisingly, $K_{\text{Cat-NO}}$ is higher than those typically obtained for ferric-iron proteins such as Mb (Fe^{3+}) whose $K_{\text{metMb-NO}}$ is $1.14 \times 10^3 \text{ M}^{-1}$ (Tab. 4.1). The reasons for these differences can be explained on the basis of our structural results (Fig. 3.1). In case of metMb, a water molecule is bound at the 6th coordination site of the heme (Laverman *et al.*, 2001), whereas our

crystallographic results for the Cat-5 complex show that this site is free (Fig. 3.1B). For the NO binding to metMb, this water molecule has to be displaced before a molecule of NO can enter to that site. In catalase, NO can easily occupy the free coordination site (Fig. 3.1B). This most likely accounts for the higher k_{on} in catalase as compared to that of metMb (Tab. 4.1).

Our geometric calculations show that the NO is slightly bent away from the heme normal with an angle of $\sim 20^\circ$ (Tab. 3.1 & 3.3). This could be another reason for large K_{Cat-NO} . It is proposed that the relatively large bending of NO may be due to the spatial overlap of NO orbitals with the molecular orbitals of the iron/porphyrin system. This has been reported also for some other model systems (Richter-Addo *et al.*, 2001). Depending on the amount of electron density provided to the iron, iron gains some ferrous character (Richter-Addo *et al.*, 2001). Ferrous iron tends to bind NO more tightly. A higher degree of overlap can provide additional stability to the nitrosylated catalase. This may account for the smaller dissociation rate coefficient of our Cat-NO adduct as compared to the metMb-NO (Tab. 4.1).

It can be suspected that the relatively large bending angle in the Cat-NO complex is coming from the reduction of iron due to photoelectrons generated by X-rays. From our micro-spectrophotometric results, the photoreduction of iron for all 3 crystal forms are evident (Fig. 3.2A-F). Reduction of iron due to photoelectrons is also observed for Nitrophorin (Ding *et al.*, 1999). Changes in the metal oxidation state may trigger major structural changes to the catalase, for example, the large bending geometry of NO. Since our experiments are performed at cryogenic temperatures (Sec. 2.5.2), only minute atomic rearrangements can take place (Kurinov & Harrison, 1995). From that, it can be

assumed that that our catalase structures are in their original ferric form, even if iron is reduced from Fe(III) to Fe(II).

The previously proposed mechanisms (Fita & Rossmann, 1985, Alfonso-Prieto *et al.*, 2007) for catalase show that the porphyrin-Fe (III) complex (Eq. 1.2-1.3) must have a tendency to easily donate electrons to facilitate the formation of compound 1. Our nitrosylated complex gains a partial ferrous character due to the spatial overlap as described above. The complex has an excess electron density and can easily give away electrons. We speculate that the ferrous characterization is enhanced, if the iron accepts some electron density from the negatively charged hydroxyl oxygen of the distal residue Tyr-357 (Tab. 3.1).

The structural changes in all three crystal forms of the catalase are minute (Tab. 3.1 & 3.4) and the iron out of plane distances are almost zero upon binding of NH_3 and NO (Tab. 3.1). The changes in the positions of active site residues are also negligible (Tab. 3.1). Similar results were reported for bacterial catalase upon ligand binding (Gouet *et al.*, 1996). Catalase's rigidity throughout the catalytic cycle is responsible for its role as an effective electron transfer protein. The structural changes remain as small as possible to optimize the speed of the reaction. These results differ for other heme proteins such as myoglobin (Schmidt *et al.*, 2005b, Nienhaus *et al.*, 2005). Once the ligand is removed heme itself becomes dome-shaped and the iron moves out of the heme plane by $\sim 0.3 \text{ \AA}$ (Schmidt *et al.*, 2005a, Ihse *et al.*, 2005). This triggers the large structural changes observed in this protein.

In our catalase structures, more than 1000 water molecules are identified (Sec. 3.1.3 & Tab. 3.2). These water molecules are located in many cavities (Tab. 3.2). The presence of

such large number of cavities provide a network to the heme and may facilitate the diffusion of H_2O_2 . A similar environment containing many cavities was observed for cytochrome c oxidase (Tab. 3.2) whose function is also based on substrate diffusion and electron transfer.

4.1.1 Significance for other heme proteins involved in electron transfer

Our results can also be applied to other heme proteins such as cytochrome-c nitrite reductase (ccNIR, Sec. 4.2.1) (Darwin *et al.*, 1993). This enzyme has some features that are similar to the catalase (Fig. 1.2). For example, it also has hemes in its active site (Einsle *et al.*, 1999, Youngblut *et al.*, 2011) and its catalytic reaction is based on the transfer of electrons (Cole, 1996). The number of electrons involved is 6 whereas 4 electrons are transferred in catalase (Sec. 1.4 & Eq. 1.2). When ccNIR catalyzes the reduction of nitrite to ammonia (Berks *et al.*, 1995), several intermediates form and decay (Cole, 1996, Einsle *et al.*, 2002, Kostera *et al.*, 2008, Youngblut *et al.*, 2011). The Cat-NO complex may mimic some of these crucial intermediates. This may provide an insight into the function of this important enzyme.

4.1.2 Summary

The three dimensional structure of Cat-NO adduct can be successfully obtained. This provides not only a detailed and deeper understanding of the reaction mechanism of the catalase but also an insight into other electron transferring proteins. These results also pave the way for easy crystallographic experiments with the NO in general and for investigations on other proteins which weakly bind NO.

4.2 *Time-resolved study on PYP*

The structures of our catalase adducts are static. They already provide information about how this protein works as a bio-catalyst. The aim is to push time-resolved experiments to perform functional studies on the catalase where we observed binding and dissociation of the substrate and product, respectively, in real time. The catalase reaction is irreversible, very fast and cannot be initiated conveniently by ultra-short light pulses. Therefore, it is tedious to follow this reaction using time-resolved crystallography on an appropriate time-scale. However, enzymatic reactions depend on temperature and in many cases also on pH. To explore the influence of these parameters on the kinetics, we employed a model system (PYP) where reaction can be repeatedly initiated in a convenient way. Results from these experiments are discussed in the following sections. Since repeated exposure to X-rays produce radiation damage, its effect on the photocycle is also explored and is discussed first. At the end, an outlook to new experiments which can be performed at the next generation of X-rays sources is presented.

4.2.1 **Effect of radiation dose**

Our results from dose experiments exhibit how the damaging effects of X-rays and laser pulses on PYP can be quantified. The uniqueness of our results is the determination of a kinetic dose limit in addition to the conventional dose limit, which is typically used to estimate the dose sensitivity of a crystal (Southworth-Davies *et al.*, 2007, Rajendran *et al.*, 2011, Kmetko *et al.*, 2011).

The relaxation times from SVD and posterior analyses are in agreement up to the kinetic dose limit, $D_{1/2}^K$ (Fig. 3.6A & B). After $D_{1/2}^K$, relaxation times from the posterior analysis

start to deviate. This shows that SVD can extract correct relaxation times even at higher X-ray doses because it is able to accurately deal with very small occupancies such as 3-5 % (Schmidt *et al.*, 2003). On the other hand, sensitivity of the posterior analysis to noisy data causes the aforementioned deviations (Schmidt *et al.*, 2012).

Up to $D_{1/2}^K$, 36 complete Laue data-sets can be collected from a PYP crystal of moderate size ($170 \times 170 \times 700 \mu\text{m}^3$) without disturbing the kinetic and structural analysis (Fig. 3.5). For a successful SVD analysis, 3 data sets per order of magnitude in time should be collected (Schmidt *et al.*, 2003). Accordingly, a complete data set covering 12 orders of magnitude in time can be collected using only one single crystal. This means, with proper experimental settings, a comprehensive time-series from picoseconds to seconds can reliably be obtained (Schmidt *et al.*, 2010).

As shown in previous studies, the dose limit $D_{1/2}$ at room temperature not only depends on the number of X-ray exposures (Tab. 4.2) used for the data collection but also on the employed dose rate (Kmetko *et al.*, 2011, Rajendran *et al.*, 2011, Southworth-Davies *et al.*, 2007). The $D_{1/2}$ decreases when the dose rate is increased (Meents *et al.*, 2010, Rajendran *et al.*, 2011). The possible reason is that at a higher dose rate, the crystal heats up. Hydrogen may be produced and continues to accumulate in the crystal. In our case, the instantaneous dose rate ($\sim 2.3 \times 10^{13} \text{ Gy s}^{-1}$) is immense; however, the damaging effects are not significant. This is because we waited for 4s between two X-ray pulses so that the crystal can cool down (Moffat *et al.*, 1992). This significantly reduces the average dose rate, which greatly affects the dose limit (Tab. 4.2). In our case, the dose limit is large even without using any radical scavengers. The addition of these

scavengers, such as ascorbate, to the crystals may increase this dose limit $D_{1/2}$ (Barker *et al.*, 2009).

Our $D_{1/2}$ is one of the largest dose limits reported so far at room temperature (Kmetko *et al.*, 2011, Rajendran *et al.*, 2011, Southworth-Davies *et al.*, 2007). However, it is more than an order of magnitude smaller than the Henderson-limit (200×10^5 Gy) and the Owen-limit (430×10^5 Gy). Both of these limits are obtained at cryogenic temperatures. The $D_{1/2}$ values at cryogenic temperatures are relatively large, because the secondary damaging effects such as diffusion of radicals are strongly inhibited at lower temperatures (Owen *et al.*, 2006).

Table 4.2 Calculated value of dose limits and employed dose rates for different type of proteins.

Protein	Dose limit ($D_{1/2}$) (Gy)	Dose rate (Gy s ⁻¹)	References
Lysozyme	16.3×10^5	10	(Southworth-Davies <i>et al.</i> , 2007)
Insulin	2.20×10^5	1430	(Rajendran <i>et al.</i> , 2011)
PYP	16.7×10^5	600	(This work) (Schmidt <i>et al.</i> , 2012).

No site-specific damage is found at any of the amino acid residues of PYP (including Asp, Glu and those containing sulphur) from the inspection of the dark difference maps ($D_{i+1} - D_1$) (Schmidt *et al.*, 2012). Interestingly, others (Kmetko *et al.*, 2011) reported specific damage even at room temperature. The only effect observed in our difference map is that the noise level increases with the increasing number of time-series (Schmidt *et al.*, 2012). The possible reason for the absence of these localized damages is that the damaged molecules quickly lose their structural integrity at the room temperature, whereas at cryogenic temperature molecules are more stable. As a result, at room temperature, even if some specific radiation damage occurs, its signature disappears as if

the entire molecule is removed (Schmidt *et al.*, 2012). This generates some strain in a crystal which causes an increase in the mosaicity at higher X-ray doses as observed in our case.

Another interesting observation is that our corrected scattering intensities decay linearly (Fig. 3.3B). For the interpretation of dose data others proposed a first order model (Southworth-Davies *et al.*, 2007) that would result in an exponential decay rather than the linear one. The reasons for these discrepancies are not known. Therefore, more experiments are necessary to propose a model that can be widely used to interpret the dose data from time-resolved crystallography.

4.2.1.1 Significance to other proteins

For PYP, the $D_{1/2}^K$ is almost half of the $D_{1/2}$ (Fig. 3.5B, Tab. 3.7). This relationship may hold for other proteins such as myoglobin (Schmidt *et al.*, 2005b) and clam hemoglobin (Knapp *et al.*, 2006), which were also investigated using long time-series from time-resolved crystallography. Results from these experiments allow us to setup a proper Laue experiment for dose-sensitive specimens such as the ccNIR (Youngblut *et al.*, 2011) as mentioned already in Sec. 4.1.1. This sensitive protein has been investigated in collaboration with the Pacheco group. Several efforts were made to determine its structure using monochromatic X-rays but remained unsuccessful. Crystals of ccNIR obstinately resist freezing. In addition, these crystals quickly deteriorate in a monochromatic X-ray beam at ambient temperatures. Structure determination became feasible only when short polychromatic X-ray pulses were used. This suggests that short-

pulsed Laue experiments may be a preferred technique for proteins, which are highly sensitive to higher doses of X-ray radiation.

4.2.1.2 Summary

With the kinetic dose limit $D_{1/2}^K$, the number of kinetically meaningful data sets can be determined from a moderately sized single crystal of PYP. The crystal size used for our experiment is very well suited for time-resolved crystallographic experiments. This information can be used as a prerequisite to setup time-resolved crystallographic experiments for other proteins.

4.2.2 Effect of pH

In addition to the kinetic dose limit, we also explored how pH affects the structures and kinetics of PYP. The effect of pH has been observed spectroscopically, but a structural analysis has never been performed before.

At pH 4.0, the relaxation time for the pB \rightarrow pG transition is increased by two orders of magnitude than that at neutral pH (Fig. 3.7B & 3.7E; Tab. 3.9). This is consistent with the previous studies which show that the pB relaxation slows down with acidification (Borucki *et al.*, 2006, Genick *et al.*, 1997a, Hoff *et al.*, 1997). The reasons for this significant deceleration of the dark state recovery from the pB state at low pH were not known before. The presence of a water molecule corresponding to our feature β (Fig. 3.8II.E & 3.8II.G) in the pB state allows us to explain this slower recovery. For the chromophore to relax from its pB state to the ground state, this water molecule has to be removed. The water molecule acts as a transient inhibitor. As soon as the pB state forms, the water enters in the chromophore pocket after 200 μ s of the state formation. Since the

two events, formation of pB and the appearance of water are closely related, the water binding must be faster than pB formation. Therefore, water appears at the instant pB is formed as observed from the structure of the pB intermediate (Fig. 3.8II.E & 3.8II.G). The water molecule stays in the pocket and exits after ~ 1 s.

The water molecule identified in the chromophore pocket may be a hydronium ion (H_3O^+) that neutralizes the negative charge on the Glu-46. Consequently, Glu-46 becomes protonated. The neutral electrostatic environment in the chromophore pocket may be one of the reasons why a large fraction of molecules relaxes directly from pR to pG (Fig. 3.7B & 3.7E).

The water molecule denoted by β feature (Fig. 3.8II.E & 3.8II.G) forms hydrogen bonds with both Tyr-42 and Glu-46 (Sec. 3.4.3). This observation enables us to explain the results obtained from the previous Fourier Transform Infrared (FTIR) spectroscopy (Brudler *et al.*, 2001, Shimizu *et al.*, 2006). This study shows that the peak belonging to

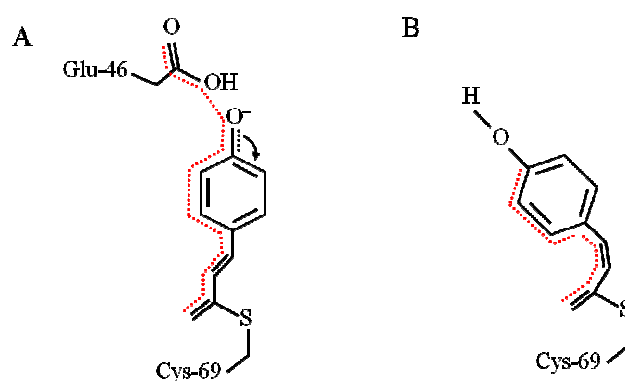


Figure 4.1 Structural differences of the PYP chromophore in the pG and blue shifted intermediate state pB. **A.** In pG, the chromophore is trans form and Glu-46 is protonated. An extended length of the conjugated system (red dashed lines) is possible. **B.** In the pB state, the proton has moved from the Glu-46 to the chromophore. Consequently, the chromophore becomes protonated. The effective length of the conjugated system is shortened and responsible for the blue shift of this intermediate.

the Glu-46 carboxyl group shifts from 1759 cm^{-1} to 1747 cm^{-1} when the pH of its surrounding environment is lowered. The presence of the water molecule (β feature; Fig. 3.8II.E & 3.8II.G) can potentially increase the hydrophilic environment near Glu-46 at low pH and may be responsible for the change in the Glu-46 IR-peak. Others (Meyer *et al.*, 2003) also speculated that the hydrogen bond between a solvent molecule and Glu-46 is responsible for the spectral form of the PYP intermediate.

In addition to the feature β , our pB state shows the presence of another feature α outside the chromophore pocket at pH 7 and pH 4 (Fig. 3.8I.E & 3.8I.G, 3.8II.E & 3.8II.G). This feature was also observed by others (Ihee *et al.*, 2005, Schmidt *et al.*, 2004) and was defined as a double conformation of Arg-52. Our improved data quality enables us to modify this interpretation. We attribute the feature α as a water molecule that forms a hydrogen bond to the phenolate oxygen of the chromophore (Sec. 3.4.3). With this, one can explain the blue shift of the pB state (Xie *et al.*, 1996). The presence of this hydrogen bond can affect the electron transition of the chromophore. The bond nature between phenolate oxygen and Glu-46 start to resemble a single bond (Fig. 4.1B). The effective length of the chromophore becomes shorter (compare Fig. 4.1A & B). This may be responsible for the blue shift. A similar observation has also been shown for a green fluorescent protein (GFP) chromophore, whose absorption maximum is blue-shifted in its protonated state (Kirchhofer *et al.*, 2009). A previous study of the pCA chromophore analog suggests that hydrogen bonds are responsible for the additional $\sim 60\text{ nm}$ shift when the protein environment is changed from aprotic to protic (Espagne *et al.*, 2006). A decrease in wavelength of $\sim 15\text{ nm}$ is observed for the pB state when protein is denatured

from its native form (Lee *et al.*, 2010, Xie *et al.*, 2001). In this form, more hydrogen bonds may form with additional water molecules leading to the extra blue shift of ~15nm. At pH 7.0, relaxation times from the SVD analysis are in agreement with previous studies (Ihee *et al.*, 2005, Schmidt *et al.*, 2005a). Ihee and coworkers reported the presence of two pB phases at neutral pH. The second phase pB₂ is much less occupied as compared to the first phase pB (Ihee *et al.*, 2005). Similarly, a faint kinetic phase corresponding to pB₂ at 71 ms is observed in our case (Fig. 3.7A). The reason for this weak phase is that the pB₁ and pB₂ are structurally very similar. Only one rSV is obtained which shows the presence of one phase coming from pB in general.

A comparison between relaxation times at pH 7.0 and 4.0 shows that the pR relaxes faster at low pH (Tab. 3.9). This causes an acceleration of the pR to pB transition. Similar behavior has also been observed before (Genick *et al.*, 1997b). The relaxation time for the pB → pG transition at pH 4 is larger by two orders of magnitude than that at pH 7 (Tab. 3.9). This is consistent with previous studies which also show that the pB relaxation slows down with acidification (Borucki *et al.*, 2006, Hoff *et al.*, 1997, Genick *et al.*, 1997b).

At basic pH (pH = 9), PYP stops cycling through the signaling state pB. From the pB state it reverts directly to ground state. The corresponding relaxation time obtained either from the SVD analysis (τ_1) or from the posterior analysis (τ_{P1}), is on the order of ~2 ms (Fig. 3.7C & F; Tab. 3.9). This time scale of τ_1 or τ_{P1} is approximately one order of magnitude larger than that at pH 4 and 7. The higher pH prevents the detachment of the chromophore head from the hydrogen-bonding network. As a result, the pR state cannot relax into another state and the chromophore reisomerizes on a time scale of milliseconds

(Tab. 3.9) as also reported by others (Genick *et al.*, 1997b). The cis-configuration after the isomerization can be further stabilized for an extended period of time only if another state is occupied. This happens at pH 7 and 4, where the pB state is largely occupied. At these pH's, the pB state stabilizes the cis configuration of the chromophore for an extended period of time.

4.2.2.1 Summary

The variation of pH has a significant effect on the kinetics of the intermediate states in general and on the signaling state in particular. The pB state is absent at pH 9.0 whereas its life time extends at lower pH's. We speculate that PYP may act as a pH sensing device in the host bacteria. The structural analysis of the reaction intermediates reveals the features that account for the blue or red shift observed spectroscopically.

4.2.3 Effect of temperature

From the dose and pH experiments, it is shown that our results are kinetically meaningful. We use this knowledge in exploring the effect of temperature on the kinetics of PYP. Results from our temperature dependent study shows that the functionality of PYP or proteins in general can be controlled by tuning the temperature. Not only structures of intermediates and chemical kinetics can be obtained but also thermodynamic properties can be extracted using the transition state equation (TSE, Eq. 4.1). The temperature dependent time-resolved study pushed crystallography to a new frontier. Results from both crystallographic and spectroscopic techniques are complementary to each other and can be tied together for a better understanding of PYP. Spectroscopic results also corroborate the findings from crystallography.

A comparison of relaxation times from time-resolved crystallography at -40 °C and 25 °C is shown in Fig. 3.10A. At higher temperature, the number of kinetic phases is reduced from 4 to 3. This is because at elevated temperatures (Appendix E), the photocycle of PYP speeds up. The fastest kinetic phase is shorter than our time-resolution and therefore cannot be detected. A decrease in the number of kinetic phases at temperatures higher than 50 °C is not due to a further acceleration of the photocycle (Schmidt *et al.*, 2013). Protein starts to unfold and potentially more pB states are formed that superpose to a longer pB kinetic phase.

Table 4.3 Rate of recovery from the signaling state pB to the dark state pG for PYP photocycle determined using time-resolved spectroscopy. The observed rates are compared with those reported by others.

Transition state	Solution	Crystal	References
Photostationary state →pG	(283 K) 666 ms ^a	NA	(Meyer <i>et al.</i> , 1989)
Photostationary state →pG	(283 K) 350 ms ^b (283 K) 363 ms ^c	(283 K) 454 ms ^d (283 K) [191 ms & 714 ms] ^e	(Ng <i>et al.</i> , 1995)
pB2→pG	(293K) 360 ms	(293K) ~20ms	(Yeremenko <i>et al.</i> , 2006)
pB1 or pB2→pG ^f	(295K) 380 ms	(273K) Biphasic [67 ms & 800 ms] (303K) Biphasic [2.2 ms & 32 ms]	This work

^a 5 mmol/L sodium phosphate pH 7.0; ^b 10 mmol/L sodium phosphate pH 7.0; ^c 50 % saturated ammonium sulfate, 283K; ^d data fitting with one exponential; ^e data fitting with two exponentials; ^f from the global fitting of rSVs by a sum of exponentials, NA not applicable

Our spectroscopic relaxation times for PYP in solution are compared with those reported by others (Tab. 4.3). The final decay (380 ms) obtained in our case is in very good agreement with the relaxation time (360 ms) observed by Yeremenko *et al.*, (Tab. 4.3). This validates the design of our micro-spectrophotometer. In addition, our relaxation time for pB→pG transition also matches with that for photostationary to pG transition (Ng *et*

al., 1995); however, these results cannot be directly compared. This is because these relaxation times are obtained at different temperatures.

A comparison of spectroscopic relaxation times on a crystalline sample is not straightforward. Our results show that at low temperature, such as 273 K, the pB→pG transition is biphasic. Between the two kinetic phases, the 2nd one (800 ms) agrees with that (714 ms) reported previously (Tab. 4.3). The pB→pG transition at 303K is also biphasic where the 2nd phase (32ms) is consistent with a single kinetic phase obtained at 293K (Tab 4.3). In addition to that, a comparison of spectroscopic relaxation times between PYP in solution and on crystals provides an insight how the crystalline phase may affect the protein kinetics.

For the crystalline samples, two pB phases are observed spectroscopically at 0 °C whereas a single pB phase is detected from crystallography (compare Fig. 3.13 & Appendix E). This is because spectra are sensitive to electronic transitions whereas diffraction patterns are more sensitive to the structural changes. Consequently, even small electronic changes in the chromophore region can be detected from spectroscopy.

From the Arrhenius plot of macroscopic rate coefficients Λ_i obtained from time-resolved crystallographic data (Fig. 3.10B-D), we determined the activation energies for the processes characterized by Λ_2 to Λ_4 . The Λ_i are linear combinations of the microscopic rate coefficients of the underlying chemical kinetic mechanism. For a precise calculation of thermodynamic variables, microscopic rate coefficients (k_i) must be determined. For this, a plausible kinetic mechanism that can properly interpret the data must be selected. Posterior analysis is applied for the selected mechanism. The mechanism used for the posterior analysis to our temperature dependent crystallographic data is shown in Fig.

3.9. The procedure to extract k_i using this analysis is outside the scope of this thesis. This has been described in detail by a recent publication (Schmidt *et al.*, 2013). Once k_i are known for a proposed kinetic mechanism, their temperature dependence can be described using the transition state equation which is given by

$$k = \frac{RT}{N_A h} e^{\frac{\Delta S^\ddagger}{R}} e^{-\frac{\Delta H^\ddagger}{RT}}, \quad (4.1)$$

where R is the gas constant, N_A is the Avogadro's number, T is temperature, h is the Planck's constant and ΔS^\ddagger and ΔH^\ddagger are the entropy and the enthalpy differences from an initial state to the transition state, respectively. From the plot of k_i against temperature, thermodynamic variables such as enthalpy, entropy and Gibbs free energy differences to the transition state can be extracted (Schmidt *et al.*, 2013). This is successfully applied to our time-resolved crystallographic data. Similarly, thermodynamic parameters can be extracted from time-resolved spectroscopy. However, more spectroscopic experiments performed at several temperature settings are necessary.

4.3 *Future applications*

As shown from our time-resolved crystallographic and spectroscopic experiments the time-resolved approaches are suitable for investigating cyclic reactions such as PYP, light sensitive complexes of heme proteins (Bourgeois *et al.*, 2007, Schmidt *et al.*, 2005b, Knapp *et al.*, 2006, Srajer *et al.*, 1996, Key *et al.*, 2007) and photosynthetic reaction centers (Neutze & Moffat, 2012). Application of these techniques to enzymatic reactions is difficult because the reaction initiation on an ultra-short time scale is not straightforward. For that, a substrate has to be provided in an ultrafast manner. Once the reaction is over, the end products must be removed. Also, the new substrate has to be

loaded so that it can be freshly exposed to the enzyme. Another challenge for investigating the enzymatic reaction is that the reaction in an enzyme can be initiated only once due to the irreversibility of these reactions. To overcome these problems, either flow cells (Kurisu *et al.*, 1997) can be used or a new crystal charged with substrate can be mounted each time. Both of these approaches are tedious and prevent rapid experiments.

Experiments on relatively faster time scales can be performed using caged substrates. In this method, an inactive caged substrate is soaked into the crystal so that the substrate can bind to the active site of the enzyme (Stoddard *et al.*, 1998, Duke *et al.*, 1994, Schlichting *et al.*, 1990, Stoddard *et al.*, 1991, Duke *et al.*, 1992, Scheidig *et al.*, 1992). A short and intense laser pulse is used to activate the caged substrate. The activation rate varies from nanoseconds to milliseconds (Adams & Tsien, 1993, Goeldner & Givens, 2005). The quantum yield of the activation may be low. A single laser shot may not activate a large fraction of the caged substrate. Chemical expertise is required to design and develop new caged substrates for various types of enzymes. These problems prevent the use of time-resolved crystallography as a routine tool to investigate these non-cyclic reactions.

Both challenges, fast reaction initiation and the requirement of multiple exposures during data collection, can be circumvented with the experiments performed at a modern facility using advanced techniques. New generation X-ray sources such as the XFEL (Fig. 4.2) deliver on the order of 10^{12} photons in a femtosecond X-ray pulse (Boutet *et al.*, 2012). Having this flux, even a single pulse provides a diffraction pattern on a tiny crystal with sufficient signal to noise ratio. Such high flux enables us to perform time-resolved experiments on small crystals. In addition, the radiation damage is absent on fast femtosecond time scale (Chapman *et al.*, 2011). For rapid reaction initiation, the easiest

way is to mix the enzyme with an active substrate and let the substrate diffuse into the crystal. To achieve the best time-resolution, the diffusion time (τ_D) into the crystal must be as fast as possible. τ_D depends on the square of the crystal size (Schmidt, 2013). For example, τ_D is on the order of seconds for a crystal of size $\sim 300 \times 400 \times 500 \mu\text{m}^3$ and decreases to $1.5 \mu\text{s}$ for $0.1 \times 0.2 \times 0.3 \mu\text{m}^3$ sized crystals. Another requirement is fast mixing of the enzyme with the substrate. With newer mixing devices, time resolution can be as good as $150 \mu\text{s}$ (Cherepanov & de Vries, 2004). Injector technology is progressing rapidly to deliver enzyme-substrate mixture into the XFEL beam (DePonte *et al.*, 2009, Park *et al.*, 2006, DePonte *et al.*, 2011, Gañán-Calvo *et al.*, 2010, Sierra *et al.*, 2012). Two events, mixing and injecting, must be carefully synchronized with X-ray pulses to probe changes in an enzymatic reaction.

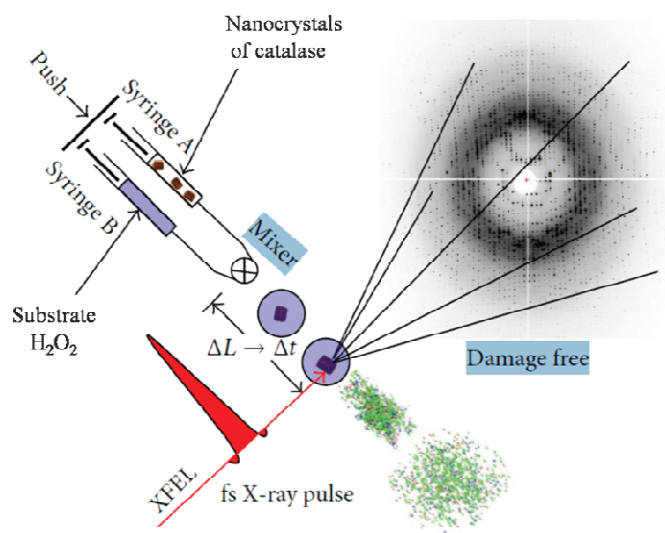


Figure 4.2 A schematic setup for a mix and inject time-resolved femtosecond (fs) serial crystallographic experiment at the XFEL. Nano- and micro-crystals of catalase are in syringe A and substrate H_2O_2 in syringe B. After mixing, the crystal/substrate droplet is injected into the XFEL beam. The crystal might disintegrate after the fs X-ray pulse, but diffraction occurs earlier. The diffraction pattern is damage free. Figure from Schmidt *et al.*, 2013 is modified.

This approach enables us to study enzymatic reactions that occur on faster time scales. One of the examples is catalase whose turnover time at ambient temperature is on the order of $\sim\mu\text{s}$ (Reid *et al.*, 1981). In addition, this method can be applied to a wide range of the enzymes because catalytic rates for most of the enzymes are favorably in the range of few ms (Cornish-Bowden, 2012). The mix and inject technique paves a way to conveniently and routinely investigate enzymatic reactions on the faster ($\sim\mu\text{s}$) time scales.

References

Adams, S. R. & Tsien, R. Y. (1993). *Annual Review of Physiology* **55**, 755-784.

- Alfonso-Prieto, M., Borovik, A., Carpena, X., Murshudov, G., Melik-Adamyan, W., Fita, I., Rovira, C. & Loewen, P. C. (2007). *J. Am. Chem. Soc.* **129**, 4193-4205.
- Andersen, J. F., Ding, X. D., Balfour, C., Shokhireva, T. K., Champagne, D. E., Walker, F. A. & Montfort, W. R. (2000). *Biochemistry* **39**, 10118-10131.
- Barker, A. I., Southworth-Davies, R. J., Paithankar, K. S., Carmichael, I. & Garman, E. F. (2009). *J Synchrotron Radiat* **16**, 205-216.
- Berks, B. C., Ferguson, S. J., Moir, J. W. & Richardson, D. J. (1995). *Biochimica et Biophysica Acta (BBA)-Bioenergetics* **1232**.
- Borucki, B., Joshi, C. P., Otto, H., Cusanovich, M. A. & Heyn, M. P. (2006). *Biophysical journal* **91**, 2991-3001.
- Bourgeois, D., de Rosay, E. & Katona, G. (2007). *Biofutur*, 48-51.
- Boutet, S., Lomb, L., Williams, G. J., Barends, T. R., Aquila, A., Doak, R. B., Weierstall, U., DePonte, D. P., Steinbrener, J., Shoeman, R. L., Messerschmidt, M., Barty, A., White, T. A., Kassemeyer, S., Kirian, R. A., Seibert, M. M., Montanez, P. A., Kenney, C., Herbst, R., Hart, P., Pines, J., Haller, G., Gruner, S. M., Philipp, H. T., Tate, M. W., Hromalik, M., Koerner, L. J., van Bakel, N., Morse, J., Ghonsalves, W., Arnlund, D., Bogan, M. J., Caleman, C., Fromme, R., Hampton, C. Y., Hunter, M. S., Johansson, L. C., Katona, G., Kupitz, C., Liang, M., Martin, A. V., Nass, K., Redecke, L., Stellato, F., Timneanu, N., Wang, D., Zatsepin, N. A., Schafer, D., Defever, J., Neutze, R., Fromme, P., Spence, J. C., Chapman, H. N. & Schlichting, I. (2012). *Science* **337**, 362-364.
- Brudler, R., Rammelsberg, R., Woo, T. T., Getzoff, E. D. & Gerwert, K. (2001). *Nature structural biology* **8**, 265-270.
- Chapman, H. N., Fromme, P., Barty, A., White, T. A., Kirian, R. A., Aquila, A., Hunter, M. S., Schulz, J., DePonte, D. P., Weierstall, U., Doak, R. B., Maia, F. R. N. C., Martin, A. V., Schlichting, I., Lomb, L., Coppola, N., Shoeman, R. L., Epp, S. W., Hartmann, R., Rolles, D., Rudenko, A., Foucar, L., Kimmel, N., Weidenspointner, G., Holl, P., Liang, M. N., Barthelmess, M., Caleman, C., Boutet, S., Bogan, M. J., Krzywinski, J., Bostedt, C., Bajt, S., Gumprecht, L., Rudek, B., Erk, B., Schmidt, C., Homke, A., Reich, C., Pietschner, D., Struder, L., Hauser, G., Gorke, H., Ullrich, J., Herrmann, S., Schaller, G., Schopper, F., Soltan, H., Kuhnel, K. U., Messerschmidt, M., Bozek, J. D., Hau-Riege, S. P., Frank, M., Hampton, C. Y., Sierra, R. G., Starodub, D., Williams, G. J., Hajdu, J., Timneanu, N., Seibert, M. M., Andreasson, J., Rocker, A., Jonsson, O., Svenda, M., Stern, S., Nass, K., Andritschke, R., Schroter, C. D., Krasniqi, F., Bott, M., Schmidt, K. E., Wang, X. Y., Grotjohann, I., Holton, J. M., Barends, T. R. M., Neutze, R., Marchesini, S., Fromme, R., Schorb, S., Rupp, D., Adolph, M., Gorkhover, T., Andersson, I., Hirsemann, H., Potdevin, G., Graafsma, H., Nilsson, B. & Spence, J. C. H. (2011). *Nature* **470**, 73-U81.
- Cherepanov, A. V. & de Vries, S. (2004). *Bba-Bioenergetics* **1656**, 1-31.
- Cole, J. (1996). *FEMS microbiology letters* **136**, 1-11.
- Cornish-Bowden, A. (2012). *Fundamentals of Enzyme Kinetics*, 4 edition ed. Wiley-VCH.
- Darwin, A., Hussain, H., Griffiths, L., Grove, J., Sambongi, Y., Busby, S. & Cole, J. (1993). *Molecular microbiology* **9**, 1255-1265.
- Deponte, D., McKeown, J., Weierstall, U., Doak, R. & Spence, J. (2011). *Ultramicroscopy* **111**, 824-827.
- DePonte, D. P., Doak, R. B., Hunter, M., Liu, Z., Weierstall, U. & Spence, J. C. H. (2009). *Micron* **40**, 507-509.
- Ding, X. D., Weichsel, A., Andersen, J. F., Shokhireva, T. K., Balfour, C., Pierik, A. J., Averill, B. A., Montfort, W. R. & Walker, F. A. (1999). *Journal of the American Chemical Society* **121**, 128-138.

- Duke, E., Hadfield, A., Walters, S., Wakatsuki, S., Bryan, R. & Johnson, L. (1992). *Philosophical Transactions of the Royal Society of London. Series A: Physical and Engineering Sciences* **340**, 245-261.
- Duke, E., Wakatsuki, S., Hadfield, A. & Johnson, L. (1994). *Protein Sci* **3**, 1178-1196.
- Einsle, O., Messerschmidt, A., Huber, R., Kroneck, P. M. H. & Neese, F. (2002). *Journal of the American Chemical Society* **124**, 11737-11745.
- Einsle, O., Messerschmidt, A., Stach, P., Bourenkov, G. P., Bartunik, H. D., Huber, R. & Kroneck, P. M. (1999). *Nature* **400**, 476-480.
- Espagne, A., Changuenet-Barret, P., Plaza, P. & Martin, M. M. (2006). *The journal of physical chemistry. A* **110**, 3393-3404.
- Fita, I. & Rossmann, M. G. (1985). *Proc. Natl. Acad. Sci. USA* **82**, 1604-1608.
- Gañán-Calvo, A. M., DePonte, D. P., Herrada, M. A., Spence, J. C., Weierstall, U. & Doak, R. B. (2010). *Small* **6**, 822-824.
- Genick, U. K., Borgstahl, G. E., Ng, K., Ren, Z., Pradervand, C., Burke, P. M., Srajer, V., Teng, T. Y., Schildkamp, W., McRee, D. E., Moffat, K. & Getzoff, E. D. (1997a). *Science* **275**, 1471-1475.
- Genick, U. K., Devanathan, S., Meyer, T. E., Canestrelli, I. L., Williams, E., Cusanovich, M. A., Tollin, G. & Getzoff, E. D. (1997b). *Biochemistry* **36**, 8-14.
- Goeldner, M. & Givens, R. (2005). *Dynamic studies in biology*. Wiley Online Library.
- Gouet, P., Jouve, H.-M., Williams, P. A., Andersson, I., Andreoletti, P., Nussaume, L. & Hajdu, J. (1996). *Nat. Struct. Biol.* **3**, 951-956.
- Hoff, W. D., Van Stokkum, I. H. M., Gural, J. & Hellingwerf, K. J. (1997). *Bba-Bioenergetics* **1322**, 151-162.
- Ihee, H., Rajagopal, S., Srajer, V., Pahl, R., Anderson, S., Schmidt, M., Schotte, F., Anfinrud, P. A., Wulff, M. & Moffat, K. (2005). *Proceedings of the National Academy of Sciences of the United States of America* **102**, 7145-7150.
- Key, J., Srajer, V., Pahl, R. & Moffat, K. (2007). *Biochemistry* **46**, 4706-4715.
- Kirchhofer, A., Helma, J., Schmidthals, K., Frauer, C., Cui, S., Karcher, A. & Rothbauer, U. (2009). *Nature structural & molecular biology*, **17**, 5.
- Kmetko, J., Warkentin, M., Englich, U. & Thorne, R. E. (2011). *Acta Crystallogr D* **67**, 881-893.
- Knapp, J. E., Pahl, R., Srajer, V. & Royer, W. E., Jr. (2006). *Proceedings of the National Academy of Sciences of the United States of America* **103**, 7649-7654.
- Kostera, J., Youngblut, M. D., Slosarczyk, J. M. & Pacheco, A. A. (2008). *JBIC Journal of Biological Inorganic Chemistry* **13**, 10.
- Kurinov, I. V. & Harrison, R. W. (1995). *Acta crystallographica. Section D, Biological crystallography* **51**, 98-109.
- Kurusu, G., Sugimoto, A., Kai, Y. & Harada, S. (1997). *J Appl Crystallogr* **30**, 1.
- Laverman, L. E., Wanat, A., Osajca, J., Stochel, G., Ford, P. C. & van Eldik, R. (2001). *J. Am. Chem. Soc.* **123**, 285-293.
- Lee, B. C., Kumauchi, M. & Hoff, W. D. (2010). *The Journal of biological chemistry* **285**, 12579-12586.
- Meents, A., Gutmann, S., Wagner, A. & Schulze-Briesse, C. (2010). *Proceedings of the National Academy of Sciences of the United States of America* **107**, 1094-1099.
- Meyer, T. E., Devanathan, S., Woo, T., Getzoff, E. D., Tollin, G. & Cusanovich, M. A. (2003). *Biochemistry* **42**, 3319-3325.
- Meyer, T. E., Tollin, G., Hazzard, J. H. & Cusanovich, M. A. (1989). *Biophysical journal* **56**, 559-564.
- Moffat, K., Chen, Y., Ng, K. M., Mcree, D. & Getzoff, E. D. (1992). *Philos T R Soc A* **340**, 175-189.

- Neutze, R. & Moffat, K. (2012). *Curr Opin Struc Biol* **22**, 651-659.
- Ng, K., Getzoff, E. D. & Moffat, K. (1995). *Biochemistry* **34**, 879-890.
- Nienhaus, K., Ostermann, A., Nienhaus, G. U., Parak, F. G. & Schmidt, M. (2005). *Biochemistry* **44**, 5095-5105.
- Owen, R. L., Rudino-Pinera, E. & Garman, E. F. (2006). *Proceedings of the National Academy of Sciences of the United States of America* **103**, 4912-4917.
- Park, H. Y., Qiu, X. Y., Rhoades, E., Korlach, J., Kwok, L. W., Zipfel, W. R., Webb, W. W. & Pollack, L. (2006). *Anal Chem* **78**, 4465-4473.
- Purwar, N.**, McGarry, J. M., Kostera, J., Pacheco, A. A. & Schmidt, M. (2011). *Biochemistry* **50**, 4491-4503.
- Rajendran, C., Dworkowski, F. S., Wang, M. & Schulze-Briese, C. (2011). *J Synchrotron Radiat* **18**, 318-328.
- Reid, T. J., Murthy, M. R. N., Sicignano, A., Tanaka, N., Musick, W. D. L. & Rossmann, M. G. (1981). *Proc. Natl. Acad. Sci. USA* **78**, 4767-4771.
- Richter-Addo, G. B., Wheeler, R. A., Hixson, C. A., Chen, L., Khan, M. A., Ellison, M. K., Schulz, C. E. & Scheidt, W. R. (2001). *J. Am. Chem. Soc.* **123**, 6314-6326.
- Rohlf, R. J., Gibson, J. S. & Gibson, O. H. (1988). *J. Biol. Chem.* **263**, 1803-1813.
- Scheidig, A. J., Pai, E. F., Schlichting, I., Corrie, J., Reid, G. P., Wittinghofer, A., Goody, R. S., Liljas, A. & Moffat, K. (1992). *Philosophical Transactions of the Royal Society of London. Series A: Physical and Engineering Sciences* **340**, 263-272.
- Schlichting, I., Almo, S. C., Rapp, G., Wilson, K., Petratos, K., Lentfer, A., Wittinghofer, A., Kabsch, W., Pai, E. F. & Petsko, G. A. (1990).
- Schmidt, M. (2013). *Advances on Condensed Matter Physics*, 1-10.
- Schmidt, M., Graber, T., Henning, R. & Srajer, V. (2010). *Acta crystallographica. Section A, Foundations of crystallography* **66**, 198-206.
- Schmidt, M., Ihee, H., Pahl, R. & Srajer, V. (2005a). *Methods Mol Biol* **305**, 115-154.
- Schmidt, M., Nienhaus, K., Pahl, R., Krasselt, A., Anderson, S., Parak, F., Nienhaus, G. U. & Srajer, V. (2005b). *Proceedings of the National Academy of Sciences of the United States of America* **102**, 11704-11709.
- Schmidt, M., Pahl, R., Srajer, V., Anderson, S., Ren, Z., Ihee, H., Rajagopal, S. & Moffat, K. (2004). *Proceedings of the National Academy of Sciences of the United States of America* **101**, 4799-4804.
- Schmidt, M., Rajagopal, S., Ren, Z. & Moffat, K. (2003). *Biophysical journal* **84**, 2112-2129.
- Schmidt, M., Srajer, V., Henning, R., Ihee, H., **Purwar, N.**, Tenboer, J. & Tripathi, S. (2013). *J Am Chem Soc*, submitted.
- Schmidt, M., Srajer, V., **Purwar, N.** & Tripathi, S. (2012). *J Synchrotron Radiat* **19**, 264-273.
- Shimizu, N., Imamoto, Y., Harigai, M., Kamikubo, H., Yamazaki, Y. & Kataoka, M. (2006). *The Journal of biological chemistry* **281**, 4318-4325.
- Sierra, R. G., Laksmono, H., Kern, J., Tran, R., Hattne, J., Alonso-Mori, R., Lassalle-Kaiser, B., Glockner, C., Hellmich, J. & Schafer, D. W. (2012). *Acta Crystallographica Section D: Biological Crystallography* **68**, 1584-1587.
- Southworth-Davies, R. J., Medina, M. A., Carmichael, I. & Garman, E. F. (2007). *Structure* **15**, 1531-1541.
- Srajer, V., Teng, T. Y., Ursby, T., Pradervand, C., Ren, Z., Adachi, S., Schildkamp, W., Bourgeois, D., Wulff, M. & Moffat, K. (1996). *Science* **274**, 1726-1729.
- Stoddard, B. L., Cohen, B. E., Brubaker, M., Mesecar, A. D. & Koshland, D. E. (1998). *Nature structural & molecular biology* **5**, 891-897.
- Stoddard, B. L., Koenigs, P., Porter, N., Petratos, K., Petsko, G. A. & Ringe, D. (1991). *Proceedings of the National Academy of Sciences* **88**, 5503-5507.

- Wilhelm, E., Battino, R. & Wilcock, R. J. (1977). *Chem. Rev.* **77**, 219-262.
- Xie, A., Hoff, W. D., Kroon, A. R. & Hellingwerf, K. J. (1996). *Biochemistry* **35**, 14671-14678.
- Xie, A., Kelemen, L., Hendriks, J., White, B. J., Hellingwerf, K. J. & Hoff, W. D. (2001). *Biochemistry* **40**, 1510-1517.
- Yeremenko, S., van Stokkum, I. H. M., Moffat, K. & Hellingwerf, K. J. (2006). *Biophysical journal* **90**, 4224-4235.
- Youngblut, M., Srajer, V., Pacheco, A. & Schmidt, M. (2011). (*submitted*).

5 Appendices

In this section, we provide the source code for the Andor basic program (Appendix A). This program was employed for the data acquisition as well as for initializing the iStar camera. During the data collection, timing is synchronized using two digital delay generators: DG545 and DG645. Only DG645 needed to be controlled by a program, therefore a Matlab graphical user interface (GUI) was created for this delay generator (Appendix B). In addition, Matlab programs were used to analyze the time-resolved spectroscopic data. The source codes for both of these programs are given in Appendices C & D. Finally, a figure from Schmidt *et al.*, 2013 shows the relaxation times obtained from the time-resolved crystallography at different temperatures (Appendix E).

5.1 Appendix A: Program 1 for time-resolved spectroscopic data collection

This program is written in the Andor basic, a proprietary programming language. It is used to collect all the time-resolved absorption spectra at different time delays with minimal user input. All the desired time-delays are manually fed in this program using another Matlab script (not shown). Since this program can be initiated with an external trigger pulse, data acquisition can easily be synchronized with the Q-switch laser pulse.

```

1 RelaxationTime = 5 // Waiting time between two laser pulses
2 t = 1000; dim exp&[t]
3 gosub .createexposuretime //create the number of exposures from 2ms-3sec
4 exp&[1] = 0.002 ; i = 1
5 while(exp&[i] < 0.01) //exposure time from 2ms-9ms
6   exp&[i+1] = exp&[i]+0.001; i = i+1
7 wend
8 while (exp&[i] >= 0.01) && (exp&[i] < 0.1) // 10ms-90ms
9   exp&[i+1] = exp&[i]+0.01; i = i+1
10 wend
11 while (exp&[i] >= 0.1) && (exp&[i] < 1.0) // 100ms-1sec
12   exp&[i+1] = exp&[i]+0.1; i = i+1
13 wend
14 while (exp&[i] < 5.0) // 1sec-4sec
15   exp&[i+1] = exp&[i]+0.005; i = i+1
16 wend
17 num = i-1; print("Total number of exposure time: "; num)
18
19 d = 10; dim delay&[d] // 8 time delays in the range from 50  $\mu$ s-1s
20 delay&[1]=0.00*10^000:delay&[2]=5.00*10^007:delay&[3]=2.06*10^008:delay&[4]=8.47*10^008:
21 delay&[5]=3.49*10^009:delay&[6]=1.43*10^010:delay&[7]=5.90*10^010:delay&[8]=2.43*10^011:
22 delay&[9]=1.00*10^012:delay&[10]=0.00*10^000
23 dim rel_exp&[d] // Relevant exposure times(exposure times >= (gate pulse width + pulse delay))
24 //Gate pulse width, a deciding factor for time-resolution
25 dim pw&[5]
26 pw&[1] = 20*10^6 : pw&[2] = 40*10^6 : pw&[3] = 60*10^6 : pw&[4] = 100*10^6 : pw&[5] =
27 170*10^6
28 // Select accumulation number based on gate pulse width
29 dim acmn&[5] ; acmn&[1] = 45 : acmn&[2] = 30 : acmn&[3] = 20 : acmn&[4] = 15 : acmn&[5] = 10
30 SaGain = 50; dim gain&[5] // Select the MCP gain, either same for each time delay or different
31 gain&[1] = SaGain : gain&[2] = SaGain : gain&[3] = SaGain : gain&[4] = SaGain : gain&[5] = SaGain
32 trigger = 2 //External triggering
33 setdatatype(6) //datatype is absorbance units; setacquisitionmode(2) //read in FVB mode
34
35 window = 100; i = 1; j = 1
36 for j = 1 to d
37   print(" next in loop j = ";j)
38   gosub .pulsewidthaccumulationifelseloop //Assign pulse width
39   while ( ((delay&[j] + pulsewidth)>= exp&[i]*10^12)&&(j<(d+1)))
40     i = i+1

```

```

41 wend
42 print(" i = ";i;" j = ";j)
43 if ((delay&j] + pulsewidth) <= exp&[i]*10^12) then
44     rel_exp&j] = exp&[i]
45     if (j = d) then /** For the dark after **
46         rel_exp&j] = exp&[1]; pulsewidth = pw&[1]
47         accumulationnumber = acmn&[1] ; MCPgain = gain&[1]
48     endif
49     print(" For delay time (";j;" ";delay&j]; ": exposure    time(";i;" ");exp&[i]*10^12;":
50     relevent exposure time(";j;" ");rel_exp&j]*10^12)
51     print(" pulsewidth = "; pulsewidth;" and accumulation  number ";accumulationnumber)
52 endif
53 next
54
55 TotalAccu = 0 // Initialization
56 gosub .takebackground
57 key(" TAKE REFERENCE NOW ") //wait for user input; gosub .takereference //take reference data
58 print("Total accumulation needed for Signal: ";TotalAccu);
59 MinutesSig=(TotalAccu*RelaxationTime)/60
60 print("Time required for Signal: ";MinutesSig;" mins = ";MinutesSig/60;" hours")
61 key(" TAKE SIGNAL NOW ") // wait for user input; gosub .takesignal //take signal data
62 print ("Successfully DONE"); print(TotalAccumulation); saveoutput("output.txt")
63
64 // ***** Function.1 called in the main program
65 .pulsewidthaccumulationifelseloop
66 if (delay&j] >= 0) then
67     if (delay&j] < 80*10^6) then
68         pulsewidth = pw&[1]; accumulationnumber = acmn&[1] ; MCPgain = gain&[1]
69         print(" Time point ";j;": delay less than 80us,  pulsewidth = ";pulsewidth)
70     endif
71     if ((delay&j] >= 80*10^6)&&(delay&j] < 200*10^6))then
72         pulsewidth = pw&[2]; accumulationnumber = acmn&[2]; MCPgain = gain&[2]
73         print(" Time point ";j;": delay b/w 80us and 200us,  pulsewidth = ";pulsewidth)
74     endif
75     if ((delay&j] >= 200*10^6)&&(delay&j] < 1*10^9))then
76         pulsewidth = pw&[3]; accumulationnumber = acmn&[3]; MCPgain = gain&[3]
77         print(" Time point ";j;": delay b/w 200us and 1ms,  pulsewidth = ";pulsewidth)
78     endif
79     if ((delay&j] >= 1*10^9) && (delay&j] < 500*10^9))then
80         pulsewidth = pw&[4]; accumulationnumber = acmn&[4]; MCPgain = gain&[4]
81         print(" Time point ";j;": delay b/w 1ms and 500ms,  pulsewidth = ";pulsewidth)
82     endif
83     if (delay&j] >= 5*10^11)then
84         pulsewidth = pw&[5]; accumulationnumber = acmn&[5]; MCPgain = gain&[5]
85         print(" Time point ";j;": delay greater than 500ms, pulsewidth = ";pulsewidth)
86     endif
87 endif
88 return
89
90 // ***** Function.2 called in the main program
91 .takebackground ; print("Ready to take background")
92 for j = 1 to d
93     gosub .pulsewidthaccumulationifelseloop

```

```

94     print(" For delay time ";delay&j];" (" ; j;") " ; ": relevant exposure time ";rel_exp&j]*10^12)
95     print(" pulsewidth = "; pulsewidth;" accumulation number = "; accumulationnumber; " MCPgain
96     = ";MCPgain)
97     setDDG(trigger, 0, delay&j], pulsewidth, 0); setaccumulatenumber(accumulationnumber)
98     setGain(MCPgain); setexposuretime(rel_exp&j]); setacquisitiontype(1); run()
99     #(window+j)_bg = #0_bg
100     next
101     return
102
103 // ***** Function.3 called in the main program
104 .takereference; print("Ready to take reference")
105 for j = 1 to d
106     gosub .pulsewidthaccumulationifelseloop
107     print(" For delay time ";delay&j];" (" ; j;") " ; ": relevant exposure time ";rel_exp&j]*10^12)
108     print(" pulsewidth = "; pulsewidth;" accumulation number = ";accumulationnumber; " MCP gain
109     = "; MCPgain)
110     setDDG(trigger, 0,delay&j], pulsewidth, 0); setexposuretime(rel_exp&j])
111     setGain(MCPgain); setacquisitiontype(2)
112     #0_bg = #(window+j)_bg; setaccumulatenumber(accumulationnumber); run()
113     #(window+j)_ref = #0_ref; TotalAccu = TotalAccu + accumulationnumber + 2
114 next
115 return
116
117 // ***** Function.4 called in the main program
118 .takesignal; print(" Now ready to take signal")
119 create(#1000,1024,1,d)
120 for j = 1 to d
121     gosub .pulsewidthaccumulationifelseloop
122     print(" For delay time ";delay&j];" (" ; j;") " ; ": relevant exposure time ";rel_exp&j]*10^12)
123     print(" pulsewidth = "; pulsewidth;" accumulation number = ";accumulationnumber; " MCP
124     gain = "; MCPgain)
125     SetDDG(trigger, 0,delay&j], pulsewidth, 0)
126     setGain(MCPgain); setexposuretime(rel_exp&j]); setacquisitiontype(0)
127     #0_bg = #(window+j)_bg; #0_ref = #(window+j)_ref
128     if (j == 2)then
129         print(" Turn on the LASER for time series ") ; key(" Turn on the LASER for time series ")
130     endif
131     if (j == (d-1))then
132         print(" Turn off the LASER and take dark "); key(" Turn off the LASER and take dark ")
133     endif
134     setaccumulatenumber(1); run()
135     #(window+j)_sig = #0_sig; setaccumulatenumber(accumulationnumber); run()
136     #(window+j)_sig = #0_sig; print("Scan ";j;" is completed")
137
138     filename$ = "pyp_" + str$(window+j) + ".sif"; save(#(window+j),filename$)
139     filename2$ = "pyp_" + str$(window+j) + ".asc"; saveasciixy(#(window+j),filename2$,2)
140     #1000_sig{j} = #(window+j)_sig
141     TotalAccu = TotalAccu - accumulationnumber-2 // Calculate remaining time for data acquisition
142     TimeRem =TotalAccu*Relaxation Time/60; print("Remaining time: ";TimeRem; "minutes")
143 next
144     save(#1000, "PYP_KS.sif"); copyxcal(#0,#1000)
145     saveasciixy(#1000,"test117.laser446.150uj.Wait4s.T285K.cov20.asc",2); closewindow(#1000)
146     return

```

5.2 Appendix B: Graphical user interface for the timing synchronization

The graphical user interface is created in Matlab for the DG645 as mentioned. It is used to control the delay between flash lamp and Q-switch pulses. With this, one can also select the desired waiting time between two subsequent laser pulses.

COM Port

COM1
COM2
COM3
COM4
COM5

Baud Rate: 9600

Disconnect Now

Set Trigger Source

Internal
External rising edges
External falling edges
Single shot external rising edges
Single shot external falling edges
Single shot
Line

Display Trigger Source

Set Ext Trigger Threshold

Enter value from -3.5 to 3.5

Disp Trigger Threshold

Delay = 2,+0.000100000000 for channel B relative to A

Set Delay

Step.1 Select Channel 1
Step.2 Select Channel 2
Step.3 Enter delay (sec)

Channel 1
To: A, B, C, D, E, F, G

Channel 2
To: A, B, C, D, E, F, G

Enter Delay (sec): 3

Display Delay Channel To:
Display Delay Channel A
Display Delay Channel B
Display Delay Channel C
Display Delay Channel D
Display Delay Channel E
Display Delay Channel F
Display Delay Channel G

Set Amplitude

Step.1 Select Output
Step.2 Enter Amplitude(V)

Output
To: AB, CD, EF, GH

Enter Amplitude (Volts)

Display Amplitude Channel To:
Display Amplitude Channel AB
Display Amplitude Channel CD
Display Amplitude Channel EF
Display Amplitude Channel GH

Set Offset

Step.1 Select Output
Step.2 Enter Offsets (Units)

Output
To: AB, CD, EF, GH

Enter Offset (Units)

Display Offset Channel To:
Display Offset Channel AB
Display Offset Channel CD
Display Offset Channel EF
Display Offset Channel GH

Set Polarity

Step.1 Select Output
Step.2 Enter Amplitude(V)

Output
To: AB, CD, EF, GH

Enter Polarity (pos or neg)

Display Polarity Channel To:
Display Polarity Channel AB
Display Polarity Channel CD
Display Polarity Channel EF
Display Polarity Channel GH

Quick Delay

Delay C wrt To: 0

Delay H wrt G

Set Advanced Triggering Mode (ADVT)

Enable
Disp ADVT mode

Advanced Setting

Type Text: DISP 11,3

Send text
Receive text

Query Disp Err
Clear Disp Err
Fix Com port Err
Self Test
Reset

5.3 Appendix C: Program 2 for time-resolved spectroscopic data analysis

The code performs the analysis of the time-resolved spectroscopic data. It requires an input file consisting of absorption spectra at different time-delays. Such file has already been produced from *program.1*. From these absorption spectra, difference spectra are first calculated and then brought to the same offsets. Spectral changes in a specified region are selected for the SVD analysis. Obtained right and left singular vectors are plotted against the time and wavelength axis, respectively.

```

1 Clear all; clc;
2 The given time range from 30us to 2s is distributed in 10 time points such that all of them are
3 equally distributed on the logarithmic scale
4 tps=12; n1=log10(30)-6; n2=log10(2);%(1st & last timepoint:30us & 2 sec)
5 time=(logspace(n1,n2,tps-2)); (% Distribute in 10 time points)
6 tp(1)=0;tp(tps)=0; tp(2:tps-1)=time; t=tp';clear n1 n2 tp;
7
8 Provide the ASCII file in which the first column is wavelength and remaining ones are the
9 absorption spectra at certain time delays
10 Kinetic_Series_Xe='test161_Sol27.asc'
11 Detailedname='t161.RT.W5s.10tps25us~2s.Sol27.L446nm150uj'
12 dark_figure=sprintf('Dark_%.tif',Detailedname)
13 absorbance_figure=sprintf('Abs_%.tif',Detailedname)
14 Difference_abs_figure=sprintf('DiffAbs_%.tif',Detailedname)
15 LeftSingularValue=sprintf('Two_LSVs_%.tif',Detailedname)
16 SingularValue=sprintf('SVs_%.tif',Detailedname)
17 RightSingularValue=sprintf('Three_wrSVs_%.tif',Detailedname)
18 delay=sprintf('Delay.tps_%.mat',Detailedname);save(delay, 'time');
19 wrSV=sprintf('wRSV_%.mat',Detailedname)
20 diffSpec=sprintf('DiffSpectra_%.asc',Detailedname)
21 FirRSVgrace=sprintf('firstrSVforGrace_%.asc',Detailedname)
22
23 Read the file & assigning variables
24 f=fopen(Kinetic_Series_Xe,'r') % read file
25 data=(fscanf(f,'%f',[tps+1 1024])); %Total Cols are 13 (1 lambda + 10 tps + 2 dark)
26 fclose(f);
27 PREwavelength=data(:,1); PREabsorbance=data(:,2:tps+1);
28 darkbefore=PREabsorbance(:,1); darkafter=PREabsorbance(:,tps);
29
30 Plot dark absorption spectra to examine the bleaching affects
31 figure(1);plot(PREwavelength,darkbefore,PREwavelength,darkafter)
32 title({'\bfDark spectra\rm'; sprintf(' %.s',Detailedname)},'fontsize',22,'fontname','Times New
33 Roman')
34 xlabel('\bfWavelength(\lambda)\rm','fontsize',22,'fontname','Times New Roman')
35 ylabel('\bfAbsorbance unit(A)\rm','fontsize',22,'fontname','Times New Roman')
36 h=legend('dark before','dark after'); set(h,'fontsize',15,'fontname','Times New Roman')
37 set(gca,'fontsize',12,'fontname','Times New Roman')

```

```

38 xlabel('\lambda (nm)','fontsize',28,'fontname','Times New Roman')
39 ylabel('A (a.u.)','fontsize',28,'fontname','Times New Roman')
40 set(gca,'fontsize',20,'fontname','Times New Roman','ticklength',[.020 .025])
41 saveas(ffigure(1),dark_figure)
42
43 Plot all the absorption spectra Vs wavelength
44 figure(2);plot(PREwavelength,PREabsorbance)
45 title({'\bfAbsorption spectra\rm'; sprintf(' %s ',Detailedname)},'fontsize',22,'fontname','Times New
46 Roman')
47 xlabel('\bfWavelength (\lambda)\rm','fontsize',22,'fontname','Times New Roman')
48 ylabel('\bfAbsorbance unit (A)\rm','fontsize',22,'fontname','Times New Roman')
49 h=legend(int2str(t*10^6));set(h,'fontsize',9,'fontname','Times New Roman');
50 set(gca,'fontsize',12,'fontname','Times New Roman')
51 saveas(ffigure(2),absorbance_figure)
52
53 Calculate the difference absorption spectra and their offsets for each time delay
54 for i=1:tps
55     diff(:,i)=PREabsorbance(:,i)-darkbefore;
56 end
57 diff_FlatRegion(:,:)=diff(360:1024,:); %flat region (520-700nm) of spectra
58 offset=mean(diff_FlatRegion); %calculate the average offset for each spectra
59 for i=1:tps
60     if offset(i)<0
61         diff(:,i)=diff(:,i)+ abs(offset(i)); % adjust offset
62     end
63     if offset(i)>0
64         diff(:,i)=diff(:,i)- abs(offset(i)); % adjust offset
65     end
66 end
67
68 figure(3);plot(PREwavelength,diff)
69 title({'\bfDifference spectra\rm'; sprintf(' %s ',Detailedname)},'fontsize',22,'fontname','Times New
70 Roman')
71 xlabel('\lambda (nm)','fontsize',22,'fontname','Times New Roman')
72 ylabel('\Delta A (a.u.)','fontsize',22,'fontname','Times New Roman')
73 h=legend(int2str(t*10^6));set(h,'fontsize',9);
74 set(gca,'fontsize',16,'fontname','Times New Roman','ticklength',[.020 .025])
75 saveas(ffigure(3),Difference_abs_figure)
76
77 Obtain the absorption and difference spectra in the wavelength range from 400-500nm,
78 where large spectral changes occur
79 RangeSelection=360 % The number 360 corresponds to 550 nm
80 wavelength=PREwavelength(1:RangeSelection); % (400-550nm)
81 absorbance=PREabsorbance(1:RangeSelection,:);
82 darkbefore=absorbance(:,1); darkafter=absorbance(:,tps);
83 Diff=diff(1:RangeSelection,2:tps-1); % remove the dark before and after
84 figure(CCP4);plot(wavelength,Diff)
85 title({'\bfDifference Spectra\rm'; sprintf(' %s ',Detailedname)},'fontsize',22,'fontname','Times New
86 Roman')
87 xlabel('\bfWavelength \lambda\rm','fontsize',22,'fontname','Times New Roman')
88 ylabel('\bfAbsorbance unit\rm','fontsize',22,'fontname','Times New Roman')
89 h=legend(int2str(time*10^6)); set(h,'fontsize',9)
90

```



```

91 Plot a time-trace of difference absorption spectra at a single wavelength such as 485 nm
92 DiffA_485nm = (diff(275,:)); % The number 275 corresponds to 485 nm
93 Solution_22C = [time DiffA_485nm(2:tps-1)];
94 xlabel('\Deltat (s)','fontsize',22,'fontname','Times New Roman');
95 ylabel('\DeltaA (a.u.)','fontsize',22,'fontname','Times New Roman');
96 set(gca,'fontsize',16,'fontname','Times New Roman')
97 set(gca,'XLim',[10^-5 10],'XTick',logspace(-5,1,7))
98
99 save('DiffA_485nm_Solu_22C.asc','Solution_22C','-ASCII')
100 save('DiffA_485nm_Solu_22C.mat','Solution_22C')
101
102 SVD calculation
103 [U,S,V]=svd(Diff,0);
104 figure(CCP4);plot(wavelength,U(:,1),'r-',wavelength,U(:,2),'b-'); title({'\bfLeft singular vectors
105 (U)\rm';sprintf(' %s ',Detailedname)},'fontsize',22,'fontname','Times New Roman')
106 xlabel('\bfWavelength (\lambda)\rm','fontsize',22,'fontname','Times New Roman')
107 ylabel('\bfSV\rm','fontsize',22,'fontname','Times New Roman');
108 h=legend('1st ISV','2nd ISV'); set(h,'fontsize',15,'fontname','Times New Roman')
109 set(gca,'fontsize',12,'fontname','Times New Roman')
110 saveas(ffigure(4),LeftSingularValue)
111
112 figure(5);plot(diag(S),'r-*');
113 h=legend('SVs');set(h,'fontsize',15,'fontname','Times New Roman'); title({'\bfSingular values
114 (S)\rm';sprintf(' %s ',Detailedname)},'fontsize',22,'fontname','Times New Roman');
115 set(gca,'fontsize',12,'fontname','Times New Roman')
116 saveas(ffigure(5),SingularValue);
117
118 wrSV=V*S
119 figure(6);semilogx(time,wrSV(:,1),'r*',time,wrSV(:,2),'b*',time,wrSV(:,3),'g*');
120 title({'\bfWeighted right singular vectors (V)\rm';sprintf(' %s
121 ',Detailedname)},'fontsize',22,'fontname','Times New Roman');
122 xlabel('\bfdelay time (s)\rm','fontsize',22,'fontname','Times New Roman');
123 ylabel('\bfS^2*rSV\rm','fontsize',22,'fontname','Times New Roman');
124 h=legend('1st wrSV','2nd wrSV','3rd wrSV'); set(h,'fontsize',15,'fontname','Times New Roman');
125 set(gca,'fontsize',17,'fontname','Times New Roman');
126 set(gca,'XLim',[10^-5 10],'XTick',logspace(-5,1,7),'YLim',[-5 42])
127 saveas(ffigure(6),RightSingularValue)
128
129 Save weighted S*rSVs for fitting routine Program.2
130 Three_wrSV=V*S(:,1:3); wrSV=sprintf('S.RSV_%s.mat',Detailedname)
131 save(wrSV,'Three_wrSV');
132 first_wrSV=Three_wrSV(:,1); firstrSVforGrace=[time first_wrSV]
133 save('FirRSVgrace','firstrSVforGrace','-ASCII')

```

5.4 Appendix D: Program 3 for the fitting of right singular vectors using a sum of exponentials

This program globally fits the right singular vectors (rSVs) using a sum of exponentials. These rSVs were already calculated in the *program 2* and used here as an input. As an example code, it is shown how two significant rSVs can be fitted using a sum of two exponentials.

```

1 Clear all; clc;
2 Load Matlab files generated from the first program (line 206-209. They contain right singular
3 vectors (rSVs) and employed time points.
4 load Delay.tps_t222.T30C.W5s.24tps25us~2s.C35.L446nm460uj.mat;
5 load S.RSV_t222.T30C.W5s.24tps25us~2s.C35.L446nm460uj.mat;
6
7 Detailedname = 't.222 30C' % Formatted output
8 FittedData=sprintf('Fit_2RSV.2tau_%.s.tif',Detailedname);
9 observed=sprintf('Obs_3RSV_%.s.asc',Detailedname);
10 calculated=sprintf('Cal_2RSV.2tau_%.s.asc',Detailedname);
11
12 Assign the variables to the observed data
13 X=time; Y1=Three_wrSV(:,1); Y2=Three_wrSV(:,2); Y3=Three_wrSV(:,3);
14 figure(1);semilogx(X,Y1,'*r',X,Y2,'*b')
15 title(sprintf('Fitted Data %.s',Detailedname),'fontsize',25,'fontname','Times New Roman')
16 xlabel('\Delta t (s)','fontsize',22,'fontname','Times New Roman');
17 ylabel('s*rSV','fontsize',22,'fontname','Times New Roman');
18 set(gca,'fontsize',16,'fontname','Times New Roman')
19 set(gca,'XLim',[10^-5 10],'XTick',logspace(-5,1,7),'YLim',[-1.3 5])
20
21 The command calls a function fun_2RSV_2tau that starts at the point x0 and finds a minimum
22 of the sum of squares of the functions. Calculate the new coefficients using LSQNONLIN.
23 [ λ1 λ2 A0 A1 A2 B0 B1 B2]
24 X0 = [-.0021 -.041 .1 .1 .1 .1 .1 .1]; % Initialization
25 Options = optimset('MaxIter',800,'MaxFunEvals',3000,'TolFun',1e-10,'Algorithm','levenberg-
26 marquardt','TolX',1e-10);
27 [x,resnorm,residual,exitflag,output]=lsqnonlin(@fun_2RSV_2tau,X0,[],[],options,X,Y1,Y2);
28
29 v=axis;
30 line([abs(x(1)),abs(x(1))],[v(3),v(CCP4)],'LineWidth',1,'LineStyle','-','MarkerSize',7,'color','k')
31 line([abs(x(2)),abs(x(2))],[v(3),v(CCP4)],'LineWidth',1,'LineStyle','-','MarkerSize',7,'color','k')
32 RelaxationTimes=sprintf('tau_1 = %2.5f s = %2.1f ms \ntau_2 = %2.2f s \nresnorm =
33 %2.3f',abs(x(1)),10^3.*abs(x(1)),abs(x(2)),resnorm)
34 h=text(v(1).*2,v(CCP4)*(0.4),RelaxationTimes); set(h,'fontname','Times New Roman','fontsize',12);
35 sprintf('resnorm = %2.4f \nexitflag = %d \n',resnorm,exitflag)
36
37 Generate a large number of time points such as 200 within in the same time range in which 10
38 points are originally generated. With this, smooth plot can be generated.
39 n1=log10(13)-6; n2=log10(CCP4);

```

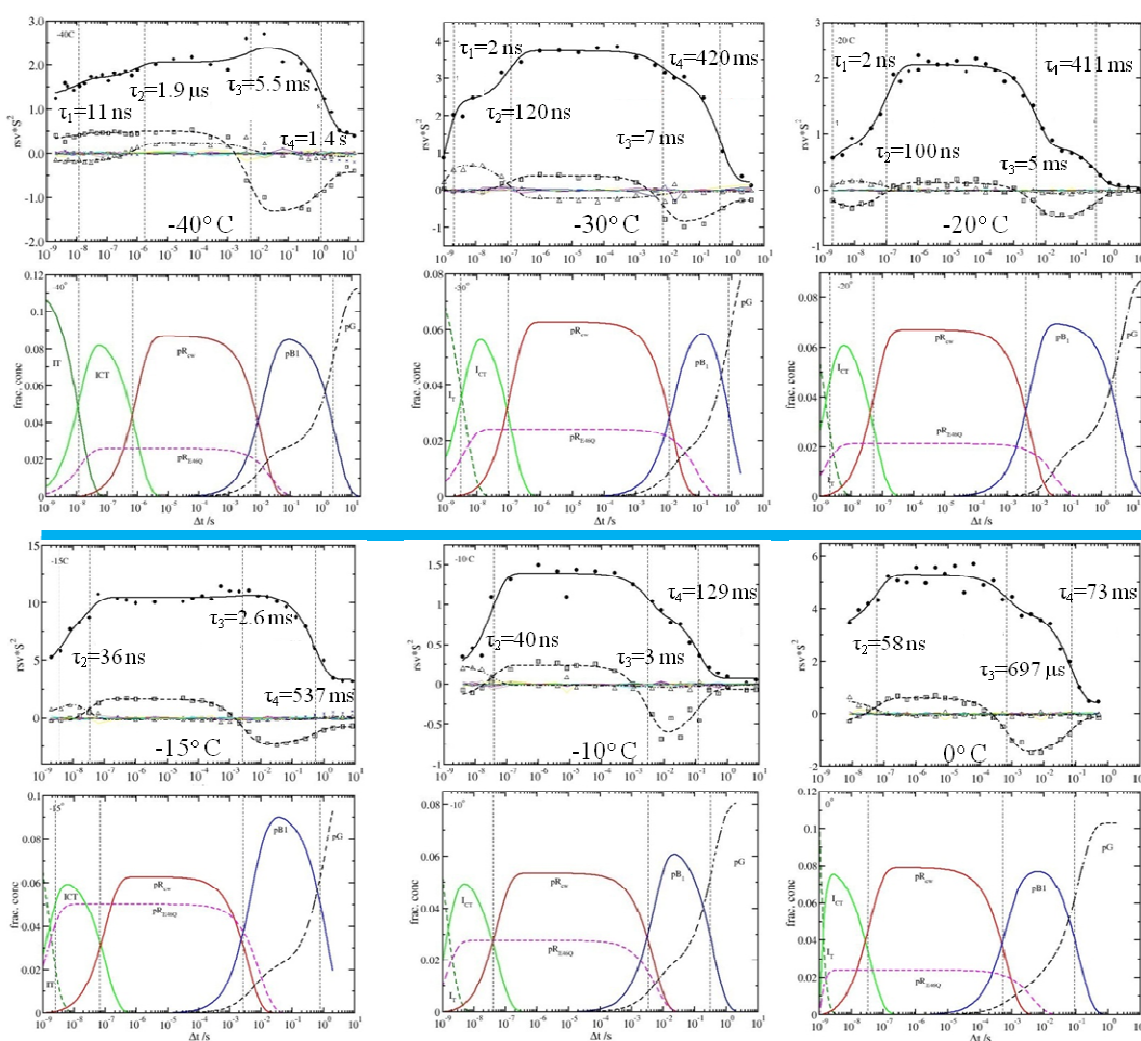
```

40 SmoothTime=logspace(n1,n2,200); X=SmoothTime'; tau1=x(1);tau2=x(2); i=3;
41 A0=x(i);A1=x(i+1);A2=x(i+2);B0=x(i+3);B1=x(i+4);B2=x(i+5);
42 Y1calc=A0 + A1.*exp(X./tau1) + A2.*exp(X./tau2);
43 Y2calc=B0 + B1.*exp(X./tau1) + B2.*exp(X./tau2);
44 Hold on; semilogx(X,Y1calc,'r',X,Y2calc,'b');
45 h=legend('1st wrSV','2nd wrSV');
46 set(h,'fontsize',12,'fontname','Times New Roman');
47 saveas(ffigure(1),FittedData); hold off
48
49 observed_ascii=[time Three_wrSV]; save (observed, 'observed_ascii', '-ASCII' )
50 Calculated_ascii=[X Y1calc Y2calc]; save (calculated, 'Calculated_ascii', '-ASCII' )
51
52 ***** THE FUNCTION fun_2RSV_2tau to be called *****
53 This function is called by lsqnonlin in the main body of the program.1 X, Y1 and Y2 are the input
54 variables that are passed to the lsqnonlin. x is the output vector.
55
56 function diff = fun_2RSV_2tau(x,X,Y1,Y2)
57 tau1=x(1);tau2=x(2); i=3; A0=x(i);A1=x(i+1);A2=x(i+2);B0=x(i+3);B1=x(i+4);B2=x(i+5);
58 diff = abs(A0 + A1.*exp(X./tau1) + A2.*exp(X./tau2) - Y1)+ abs(B0 + B1.*exp(X./tau1) +
59 B2.*exp(X./tau2) - Y2);

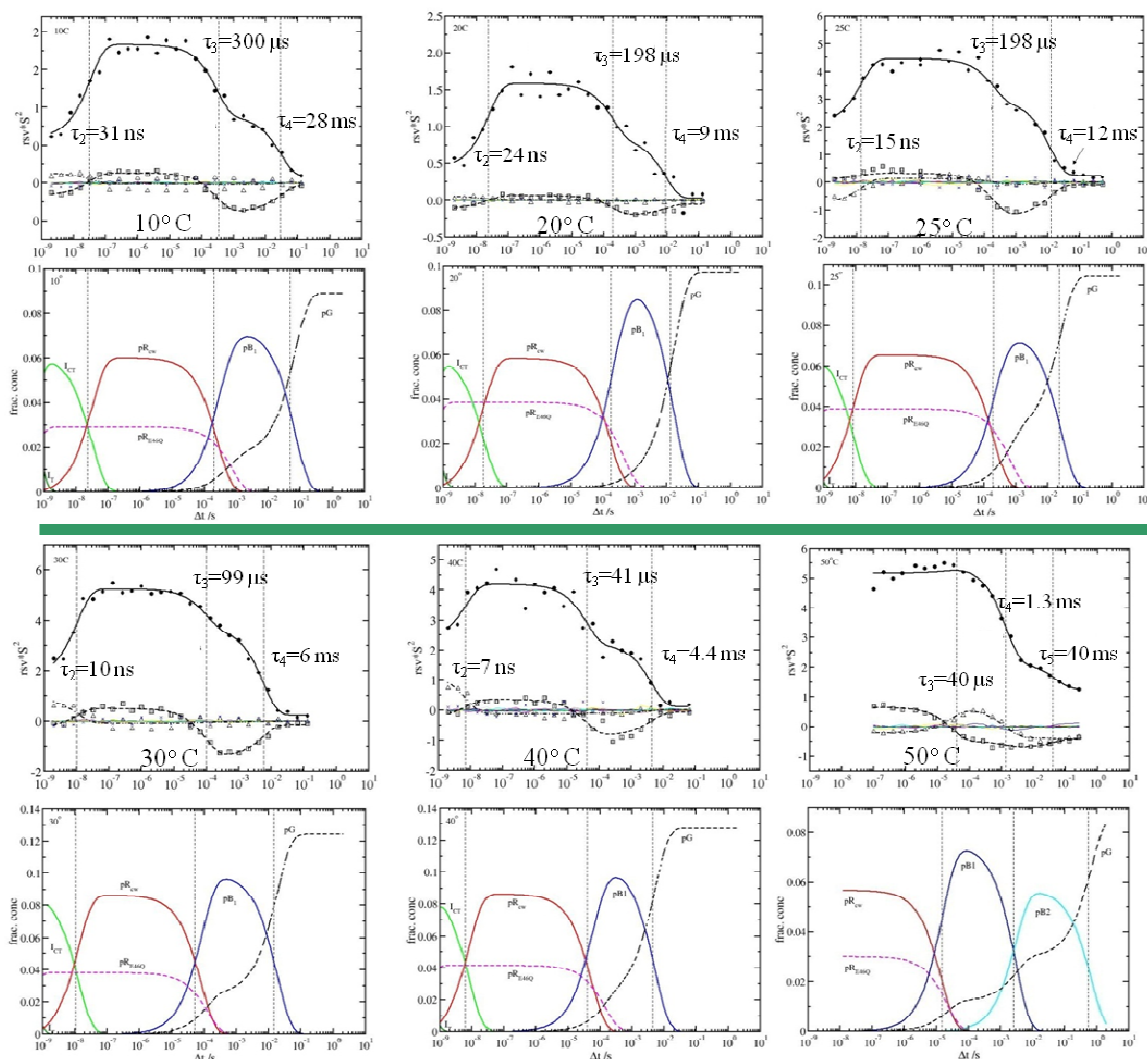
```

5.5 Appendix E: A figure showing the relaxation times obtained from time-resolved crystallography

The figure from Schmidt *et al.*, 2013 shows the relaxation times obtained for PYP using time-resolved crystallography at different temperatures. The temperature range is from -40 °C to 50 °C. Upper panels show the rSVs from SVD analysis. From the global fit of these rSVs, the associated relaxation times are calculated. Lower panels show the concentration profiles obtained by kinetic modeling.



Continued



CURRICULUM VITAE

Namrta Purwar

Place of birth: Orai, U.P., India

Education

2006-Present	Ph.D. (Biophysics), Department of Physics, UW-Milwaukee, USA
2002-2004	M.S. (Physics), Bundelkhand University, Jhansi, India

Dissertation Title

Structure and function of proteins investigated by crystallographic and spectroscopic time-resolved methods

Publications

-
1. Deepti Pachauri; Timothy A. Stiles; **Namrta Purwar**; Prasenjit Dey and S. K. Patch (2008) Transducer frequency response and impact on TPOAT signal. **International society for optics and photonics** 6856, 68561H.
 2. A. Ulijasz, **Namrta Purwar**; V. Srajer and M. Schmidt (2010) Biological, macromolecular switches and cyclers. **Romanian Journal of Biochemistry** 47(2), 155-164.
 3. **Namrta Purwar**; Jennifer M. McGarry and Joshua Kostera; A. Andrew Pacheco; Marius Schmidt (2011), Interaction of Nitric oxide with Catalase: Structural and kinetic analysis. **Biochemistry** 50(21), 4491-4503.
 4. Marius Schmidt; Vukica Srajer; **Namrta Purwar** and Shailesh Tripathi (2012), The kinetic dose limit in room-temperature time-resolved macromolecular crystallography. **Journal of Synchrotron Radiation** 19(2), 264-73.
 5. Shailesh Tripathi; Vukica Srajer; **Namrta Purwar**; Robert Henning and Marius Schmidt (2012) pH dependence of the photoactive yellow protein photocycle investigated by time-resolved crystallography. **Biophysical Journal** 102(2), 325-332.
 6. **Namrta Purwar**; Jason Tenboer; Shailesh Tripathi and Marius Schmidt (2013) Spectroscopic studies of model photo-receptors: Validation of a nanosecond time-resolved micro-spectrophotometer design using photoactive yellow protein and α – phycoerythrocyanin. **International Journal of Molecular Sciences** 14, 18881-18898.
 7. Marius Schmidt; Vukica Srajer; Robert Henning; Hyotcherl Ihee; **Namrta Purwar**; Jason Tenboer and Shailesh Tripathi (2013) Protein Energy Landscapes Determined by 5-Dimensional Crystallography. **Acta Crystallographica Section D (Accepted)**.

Workshops attended and posters/Presentations

2013 Time-resolved experiments, Biophysics seminar, UW Milwaukee, WI

2012 Time-resolved spectroscopic study on photoactive yellow protein with newly designed micro-spectrophotometer, Biophysics seminar, UW Milwaukee, WI

2011 Structural and kinetic analysis of nitrosylated beef liver catalase & five dimensional crystallographic studies of photoactive yellow protein, Biophysics seminar, UW Milwaukee, WI

2011 Dynamic X-ray Scattering in Structural Biology held at BioCARS Advanced Photon Source, Argonne National Laboratory, Chicago, IL

2010 An X-ray Crystallographic Investigation of Nitric Oxide Binding to Beef Liver Catalase; **Namrta Purwar**, Jennifer McGarry, A. Andrew Pacheco, Marius Schmidt, American Crystallographic Association, Chicago IL

2010 Interaction of Nitric Oxide with beef liver catalase: Structural and Kinetic analysis, Biophysics seminar, UW Milwaukee, WI

2009 Seeing protein molecules change in real time using time resolved X-ray crystallography; Jennifer McGarry, **Namrta Purwar**, Marius Schmidt, A. Andy Pacheco, Undergraduate research symposium, UW Milwaukee, WI

2008 Time-resolved Macromolecular Crystallography held at BioCARS Advanced Photon Source, Argonne National Laboratory Chicago IL

Academic Awards/Achievements

2013 CGSA physics, David Lichtman memorial scholarship & UWM scholarship 1

2012 CGSA physics & David Lichtman memorial scholarship

2010-11 CGSA physics & UWM scholarship 1

2009 CGSA physics, Chancellor's graduate student award & UWM scholarship 5ND

2008 CGSA physics

2006-07 Chancellor's graduate student award

- Topper in B.Sc. in P.C.M. (Physics, Chemistry, Mathematics) in the B. B. College & Bundelkhand University, Jhansi (India)
- Second rank in M.Sc. (Physics) at B.B. College, Bundelkhand University, Jhansi
- Gold medal for highest marks in the Bundelkhand university, Jhansi